TU Delft Delft University of Technology

Electrochemical degradation of GenX using boron-doped diamond anodes

Experimental insights into degradation influencing factors

Diwakar Suresh Babu

Materials Science & Engineering

Electrochemical degradation of GenX using boron-doped diamond anodes

Experimental insights into degradation influencing factors

by

Diwakar Suresh Babu

in partial fulfillment of the requirements for the degree of

Master of Science

in Materials Science and Engineering at the Delft University of Technology,

to be defended publicly on **10 February, 2021**.

Student number	4873467
Project duration	February 1, 2020 – February 10, 2021

Thesis Supervisor

Dr. Ivan Buijnsters,	Delft University of Technology

Thesis Committee

Dr. Ivan Buijnsters,	Delft University of Technology (Chair)
Prof.dr.ir. Arjan Mol,	Delft University of Technology
Dr. Peyman Taheri,	Delft University of Technology
Dr. Martin Pabst,	Delft University of Technology

TU Delft

Contents

ABSTRACT

The presence of harmful pollutants and toxic pathogens in water is a risk to both living beings and the environment. Water treatment plays a crucial role in the removal of these contaminants through different stages of filtration. Among the existing pollutants, a family of per- and polyfluoroalkyl substances (PFAS) escapes from all treatment methods and ends up in our food, water and, finally, in our blood. Current treatment methods are not effective due to their inability to break the strong C-F bonds in PFAS. Perfluorooctanoic acid (PFOA) and perfluorooctanesulfonate (PFOS) are the most widely studied PFAS due to their widespread contamination of various environmental and biological matrices. Due to the global ban of PFOA, a short-chain fluorinated compound named GenX (the ammonium salt of hexafluoropropylene oxide dimer acid) is currently used as an alternative. However, recent studies have shown that GenX has higher toxicity compared to PFOA and is more easily soluble in water, thus making it more difficult for removal. Hence, this research surveys the potential of using boron-doped diamond (BDD) anodes, which are known to have the largest potential window and high stability over time, for GenX degradation . During the electrochemical advanced oxidation process (EAOP), the highly reactive hydroxyl radicals ($OH^{\bullet}$) produced at the BDD surface break the C-F bonds to form fluoride (F^{-}) and CO_2 products. Till date, very limited research is reported on the GenX degradation and they present a contradiction on the effect of sulfate radicals ($SO_4^{\bullet -}$), considered for their high redox potential, in the GenX degradation.

In the present study, we investigate the degradation and defluorination efficiency of GenX using boron-doped diamond anodes in EAOP. This study aims to elucidate the first step in the degradation mechanism of GenX and to clarify the contradictions previously reported on the role of sulfate radicals. Experiments are performed separately with sodium sulfate and sodium perchlorate to assess the effect of $SO_4^{\bullet -}$. The results demonstrate that sulfate radicals are ineffective in GenX degradation due to the steric hindrance by the -CF_3 branch which blocks the trajectory of $SO_4^{\bullet -}$ for electron transfer reaction. The effects of electrolyte concentration, current density, and chloride radicals on the degradation and defluorination are investigated for the first time to provide in-depth understanding of the degradation mechanism. A possible degradation pathway is proposed by determination of the intermediate products using mass spectrometry. From the proposed pathway, it is inferred that GenX completely mineralizes to CO_2 and F^{-} via formation of three intermediates.

By comparing the electrochemical degradation of GenX with that of PFOA, it is observed that the presence of the -CF_3 branch increases the complexity of electron transfer in the GenX degradation even though the mineralization rate is faster for GenX than for PFOA due to lesser number of intermediates. Hence, the direct electron transfer from GenX to the BDD anode is observed to be the rate-determining step in the GenX degradation. Additionally, by comparing different BDD anodes based on their material properties and surface morphology, it is observed that the presence of sp^2 regions which act as active sites for effective electron transfer is necessary to initiate the GenX degradation mechanism. Electrochemical degradation of GenX using the BDD anodes has resulted in the complete mineralization to CO_2 and F^{-} which supports EAOP using BDD anodes as a promising approach towards effective PFAS degradation.

Keywords: boron-doped diamond (BDD); hexafluoropropylene oxide dimer acid (HFPO-DA); GenX; electrochemical oxidation; hydroxyl radicals ($OH^{\bullet}$); perfluorooctanoic acid (PFOA).

ACKNOWLEDGEMENTS

In view of the ongoing COVID-19 pandemic, this project could not have been feasible without the guidance and helping hands of several people. I would like to take this opportunity to express my sincere gratitude to all those who supported me in this journey, especially during the course of my master thesis. I'm extremely thankful to TU Delft for allowing students to carry out their research amidst the serious lockdown and to take extra measures to ensure safe working environment.

I am grateful to the Department of Materials Science and Engineering (MSE) for providing me the freedom to choose courses specializing in Nanotechnology from various departments and to carry out an interdepartmental master thesis. I would also like to thank the Department of Precision and Microsystem Engineering (PME) and the Department of Process and Energy (P&E) for providing me the facilities and materials required for my project. The advantage of working across different departments helped me to gain a lot of contacts who shared their ongoing research. Their technical insights broadened my knowledge base as I was able to understand the complexity of various projects that I was not familiar with.

Firstly, I would like to acknowledge the European Union for being transparent and reporting freely on the harmful effects of the per- and polyfluoroalkyl substances (PFAS) and providing a comparison of PFAS found in various sources across all EU countries. I would like to acknowledge the National Institute for Public Health and the Environment (RIVM, The Netherlands) for conducting a number of surveys to report the PFAS levels in air, water, soil and food and its strictness towards the industries to drastically reduce the quantity of PFAS discharged into the environment. In particular, The Netherlands leading the European PFAS ban owing to the harm it does to people and weighing the people's life over the country's profit is highly appreciated.

I want to extend my deepest sense of gratitude to my thesis supervisor, Dr. Ivan Buijnsters, for giving me the opportunity to frame my own thesis topic. His constant support and prompt replies to my mail have made me run the extra mile. Also, Ivan being my internship supervisor, he has always appreciated the different versions of my abilities and has made his fullest contribution to make me a better person. I would like to thank my thesis committee members, Prof. Arjan Mol and Dr. Peyman Taheri for their guidance during my thesis and to provide their suggestions on framing my research objectives. I would like to specially thank Dr. Martin Pabst from the Faculty of Applied Sciences for helping me with the Mass Spectrometry analysis that made my research complete and for teaching me how to interpret the MS spectra using Xcalibur software. I thank Christophe Provent from Neocoat, Switzerland for delivering the BDD electrodes on time and for the valuable discussions to clear my doubts.

It is my radiant sentiment to place on record my regards to Michel van den Brink (P&E) for training me to use their HPLC and IC facility needed for my analysis. Despite being extraordinarily busy with his lab duties, he always offered his hands to fix issues whenever the equipment was down and to answer my queries patiently. The consistent problem occuring with the HPLC and looking for solutions by playing with the LC parameters have made me an HPLC expert. I specially thank Jan Volkers from Instrument Solutions to provide me with instant support on replacing the defective UV/Vis and ensuring that I don't have any delay due to this downtime. I would like to acknowledge the technical interactions I had with Mariette de Groen and Louis Legrand from Coval Energy during the IC measurements. I would also like to thank Yasmina Bennani and Patricia van den Bos from Sanitary Engineering (CiTG) for providing me the C18 HPLC column without which this project

could have not moved forward. I would like to thank the PME technicians, Rob Luttjeboer and Spiridon van Veldhoven for ordering my materials on time and to provide support with the equipment. I would like to thank MSE corrosion lab technician, Agnieszka Koojman, for providing me training on contact angle measurement and helping me with the start of my experiments. Furthermore, I thank Kees Kwakernaak (MSE) for performing the EBSD measurements and providing me a detailed report on the analysis. I would like to thank Ursa Tiringer (MSE Postdoc) for the XPS analysis and for teaching me how to fit the XPS spectra. I thank Saskia van der Meer for taking care of my graduation procedure and to make sure I don't face any obstacles with the procedures.

I thank Mirsajjad Mousavi (MSE PhD) for helping me with the AFM measurements and for giving me a tutorial on using the Gwyddion software. I thank Maxine Ankora (MSE PhD) for helping me with the UV-Vis measurements. A special thanks to Daniel Fan (PME Postdoc) and Balakrishnan Munirathinam (MSE Postdoc) who have been more like a mentor in helping me with tips on writing a research paper and to get me started with the next phase of my career which is to pursue a PhD. I would like to thank Romme Koldenhof and Zhichao Liu for getting me started with the electrochemical experiments and I totally enjoyed the brainstorming discussions we had if any new observations were made. Futhermore, I thank the following PhDs, Saleh Aghajani (PME), Ahmed Sharaf (PME), Mirsajjad Mousavi (MSE), Simone Asperti (P&E), Chenghao Zhang (PME) and Shidong Zhang (PME) for their valuable advice on applying to a PhD, writing a paper, and for frequent lively discussions with a free coffee.

This acknowledgement would not be complete without thanking my colleagues, Brian, Damla, Bob, Halis, Innocent, Michiel, Sanne, and Pieter for all the fun and valuable discussions we had while working in the lab and during breaks. A special thanks to my senior Siddharth Gupta who has been more like a brother and helped me with a lot of advice and directions which made my life easier. I'm so grateful to my friends, Sahith, Kalyan, Vishnu, Deepak, Tanya, Lakshmi, Kaustub, Aleem, Alexandra, and Nawel who have been more like a family and been with me through thick and thin.

I would like to express my sincere gratitude to my parents and grandparents for always being there and supporting me through every decision I've taken in my life and for being a constant source of motivation. I thank my grandfather, Mr. Venugopal, who moulded me to what I'm today with his life lessons. His passing just months before my graduation really took a toll on me and it needed some serious motivation to get myself back to my work. I'm forever thankful to Gayathri Pichai for her constant encouragement to finish my thesis on time and for her unending support. Finally, I thank God for blessing me with the required mental fortitude and direction to complete this project.

While writing the acknowledgements, I felt so happy and blessed to see the number of people I have interacted within a short period of time. Each one has contributed to my success in some way and has given me memories to cherish for a lifetime.

Diwakar Suresh Babu
Delft, February 2021

Cover image: https://www.cmbg3.com/pfas-consumer-products-regulation-legislative-update

NOMENCLATURE

AFFF Aqueous Film-Forming Foam.

AFM Atomic Force Microscopy.

AOPs Advanced Oxidation Processes.

BDD Boron-Doped Diamond.

CTE Coefficient of Thermal Expansion.

CV Cyclic Voltammetry.

CVD Chemical Vapor Deposition.

DET Direct Electron Transfer.

EAOP Electrochemical Advanced Oxidation Process.

EBSD Electron Backscatter Diffraction.

ECHA European Chemical Agency.

EIS Electrochemical Impedance Spectroscopy.

GAC Granular Activated Carbon.

HFPO-DA Hexafluoropropylene Oxide Dimer Acid.

HPHT High-Pressure High-Temperature.

HPLC High Performance Liquid Chromatography.

IPF Inverse Pole Figure.

LC-MS Liquid Chromatography-Mass Spectrometry.

LSV Linear Sweep Voltammetry.

MCD Microcrystalline Diamond.

NOAEL No-Observed-Adverse-Effect-Level.

PFAS Per- and Polyfluoroalkyl Substances.

PFOA Perfluorooctanoic acid.

PFOS Perfluorooctanesulfonic acid.

ppm Parts Per Million.

ROS Reactive Oxygen Species.

SEM Scanning Electron Microscopy.

SFE Surface Free Energy.

SHE Standard Hydrogen Electrode.

SVHC Substances of Very High Concern.

TOC Total Organic Carbon.

UNCD Ultrananocrystalline Diamond.

UPLC Ultra Performance Liquid Chromatography.

XPS X-ray Photoelectron Spectroscopy.

List of Figures

List of Tables

1

INTRODUCTION

1.1 INTRODUCTION

Groundwater plays a permanent role in supporting the economy of a country. In The Netherlands, groundwater majorly contributes in providing drinking water to its residents as seen in Figure 1.1 [1]. The five components that are involved in water supply are (i) Groundwater or surface water abstraction, (ii) Treatment, (iii) Transport, (iv) Storage and (v) Distribution (Fig. 1.2). Out of the five components, water treatment contributes greatly in ensuring the quality of drinking water supplied to the residents [2].

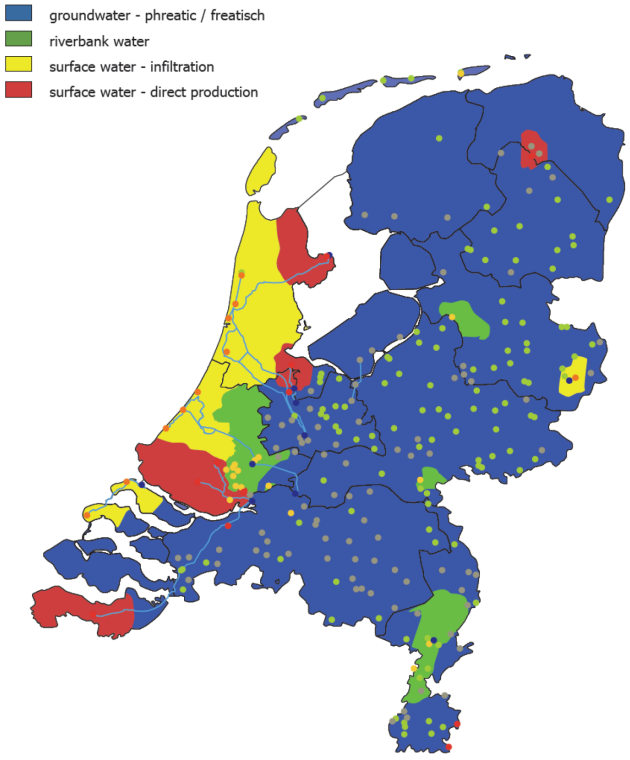

Figure 1.1: Source of drinking water in The Netherlands [1]

With growing industrialisation, the number of chemicals used in the manufacture of consumer goods has increased enormously. The effluents from respective industries are discharged into the river which end up in the groundwater. With new chemicals being used and discharged, innovations in water treatment are

necessary to meet the quality standards of drinking water. The common groundwater pollutants are pharmaceuticals, pesticides, heavy metals, pathogens, organic and inorganic compounds [3]. According to The Netherlands Environmental Assessment Agency, the cost incurred to produce drinking water and to treat the sewage water is estimated to be 10.2 billion euros per year (1.26% of GDP, 2018) [4].

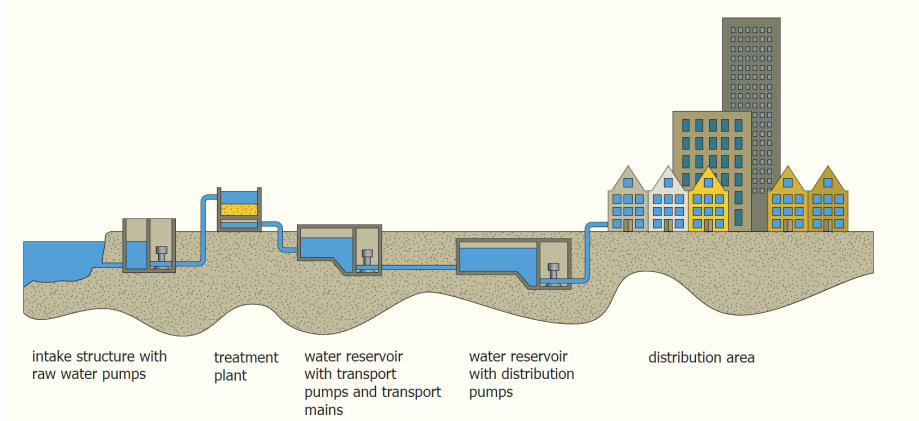

Figure 1.2: Schematic of drinking water supply in The Netherlands [2]

Current water treatment methods are effective enough to remove most of the river and groundwater pollutants. The most basic treatment involves aeration through spraying water over dry filters made of limestone to remove the dissolved gases like CO_2 and to reduce the water hardness. Advanced treatment involves the use of activated carbon, ultrafiltration, reverse osmosis and UV-disinfection as shown in Figure 1.3 for the treatment of groundwater and surface water, respectively.

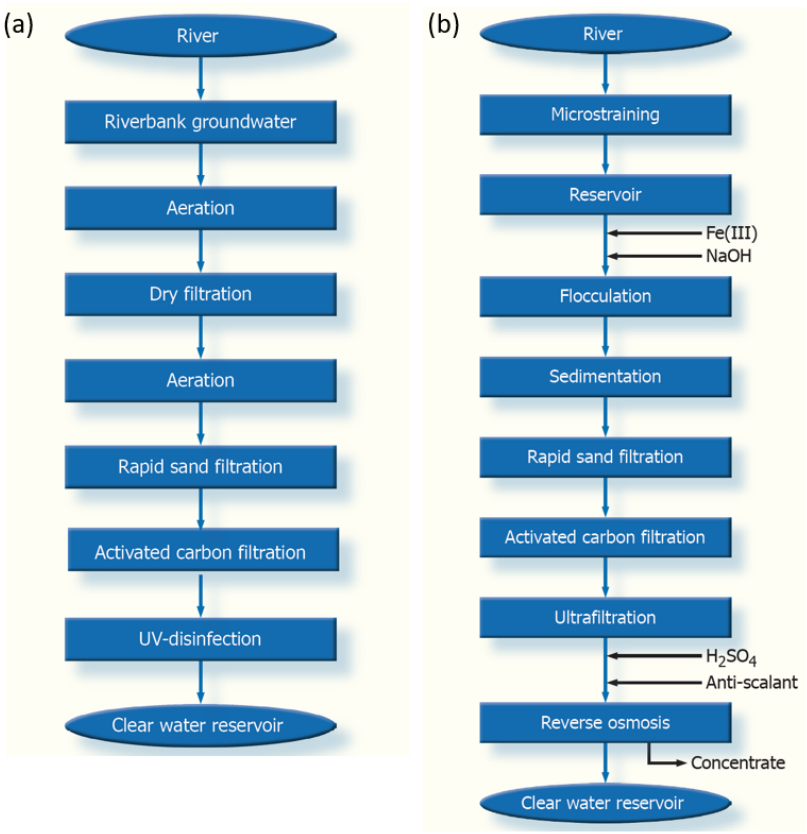

Figure 1.3: Flowchart of stages involved in the treatment of (a) groundwater and (b) surface water [2]

Amidst continuous innovations and the different stages involved in water treatment, there are a family of substances called per- and polyfluoroalkyl substances (PFAS) that manage to pass through all these different treatment methods and finally end up in the drinking water. Hence, this research serves to explore the potential of electrochemical advanced oxidation process (EAOP) as an advanced water treatment method to degrade the PFAS which is briefly explained in the upcoming chapters.

1.2 MOTIVATION

With an interest to work on advanced water treatment to remove one of the most complex recalcitrant pollutants, a literature survey was done to list down a few toxic pollutants. It came to light that PFAS is nicknamed "Forever Chemicals" due to their high chemical stability and resistance to conventional treatment methods which required an urgent solution. The forever chemicals have been extensively surveyed by RIVM (The National Institute for Public Health and the Environment, The Netherlands), as they are placed on the list of 'substances of very high concern' (SVHC) by the European Chemicals Agency (ECHA). Fixing on to the forever chemical due to its complexity to degrade, the current available methodologies to remove PFAS from water are reviewed and the electrochemical degradation of PFAS using BDD anode is demonstrated with an experimental insight into degradation influencing parameters.

1.3 OUTLINE OF THE REPORT

This report consists of 6 chapters. The report starts with the current chapter which outlines the introduction to water treatment, the motivation and the approach taken. Chapter 2 encapsulates an in-depth literature survey and theoretical background of current electrochemical advanced oxidation processes and the potential of using boron-doped diamond (BDD) as an anode in EAOP. This chapter also reports the available literature on electrochemical degradation of PFAS using BDD anodes. Chapter 3 deals with finding the knowledge gap and the research objectives on closing the gap. A brief description of the experimental setup, characterization techniques and analytical tools used is given in Chapter 4. Chapter 5 deals with the results and discussion of GenX degradation using BDD anodes and the effect of anodic oxidation on the surface morphology and material properties of boron-doped diamond. To avoid confusion to the reader, this chapter is split into 5 parts. Part 2 forms the core of this research from which a manuscript has been prepared for journal publication. Finally, in Chapter 6, the conclusions drawn from this research are provided along with recommendations for future work on this topic.

2

LITERATURE REVIEW

This chapter deals with the necessary theoretical background required to gain a comprehensive understanding of the contents of this research. This chapter is split into 4 sections. The first section deals with the history, properties and applications of PFAS, followed by a case study on PFAS detected in various sources in The Netherlands. The second section explains the current treatment methods employed to remove PFAS. The advantages of EAOP and the potential of using BDD anodes in EAOP are discussed in the third section. The final section provides a critical review of current literature available on PFAS degradation using BDD anodes and the various parameters involved in EAOP.

2.1 PFAS

2.1.1 HISTORY OF PFAS

PFAS are man-made substances containing at least 4730 different substances in its family [5]. The invention of PFAS finds its date back to the 1930s when a group of scientists involved in the Manhattan project to make nuclear bombs invented it by accident. PFAS were used mainly in non-stick coatings. Later in the 1960s, the fire emerged from the accidental launch of a rocket into US navy planes and fuel tanks led to a tragic incident of killing 130 people [6]. This incident led the scientists to develop aqueous film-forming foam (AFFF) which contained PFAS as the main ingredient and were used as a fire extinguisher medium. Since then, scientists worldwide were extensively involved in studying the properties of PFAS and industries like 3M and DuPont started to use these chemicals in a broad range of consumer products [7]. As seen in Figure 2.1, Perfluorooctanoic acid (PFOA) and Perfluorooctanesulfonic acid (PFOS) were the two extensively used chemicals in the industries at an early stage. The serious human health concerns associated with the PFAS resulted in the ban of PFOS and PFOA in most of the countries which led industries to use short-chained PFAS that seemed less harmful [8].

2.1.2 PROPERTIES OF PFAS

- PFAS are man-made synthetic organofluorine chemical compounds of the form (-C_nF_{2n}-) [9].

- They consist of a long chain made of C-F bonds which are the strongest bonds in organic chemistry. They are called 'Forever Chemicals' due to their inability to degrade naturally.

- PFAS are made with a hydrophilic head containing polar functional groups connected to this hydrophobic chain of C-F bonds as seen in Figure 2.2 [10].
- C-F bond has a bond dissociation energy of up to 544 kJ/mol, making PFAS repel almost everything (e.g. oil, water) that comes in contact with them [9].
- The chemical structure of PFAS effectively reduces the surface tension of water, hence finding their application as excellent surfactants and dispersants [11][12].
- The strength of C-F bonds gives these substances excellent chemical and thermal stability.

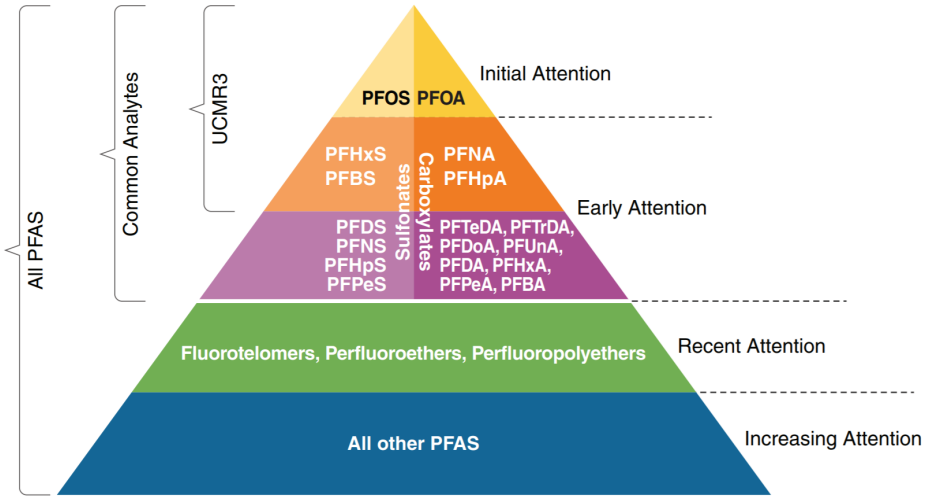

Figure 2.1: PFAS family and its hierarchy [8]

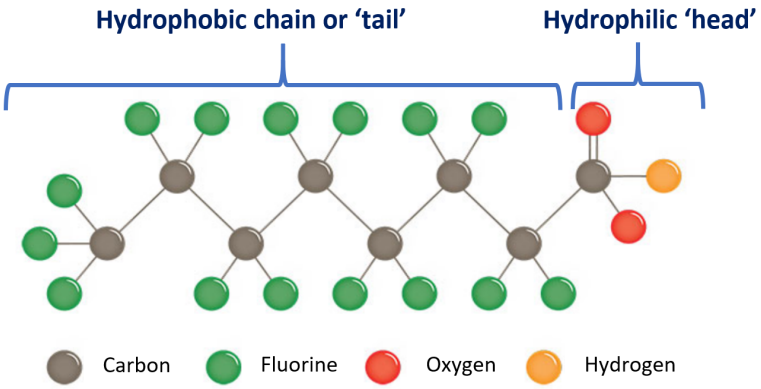

Figure 2.2: Molecular structure of PFOA with a carboxylic head group [12]

2.1.3 Applications of PFAS

Table 2.1 shows the applications of PFAS in consumer goods. From this, it can be understood that PFAS are omnipresent and in some way humans consume PFAS through contact materials on a daily basis. In the early period, fire-fighting foams were the most important cause for polluting the groundwater and have been a main reason for causing cancer in firefighters [13].

Table 2.1: Applications of PFAS in different industrial sectors

Sectors	Uses
Textiles & leathers	- Waterproof clothing - Umbrellas - Carpets - Upholstery
Cookware	- Teflon pans - Non-stick cutlery - Baking paper
Industrial surfactant & resins	- Fire-fighting foams - Fluoropolymer coatings - Composite resins
Food contact materials	- Pizza and doner boxes - Microwave popcorn bags - Fast-food wrappers - Beverage cups
Wire & tape manufacturing	- Wire insulation - Insulation tapes

2.1.4 PFAS CYCLE

Fluorochemical production plants discharge PFAS in allowed quantities directly into the water stream and the rest to water treatment plants. The sludge containing PFAS ends up in landfills which are then used in dredging and farmlands. The vegetables and crops grown in the PFAS contaminated soil are found to contain PFAS [14]. The water from river and ground are treated and supplied to residents but PFAS still exists in the drinking water. Humans consume PFAS through drinking water, food and indirectly through food contact products. This cycle is schematically illustrated in Figure 2.3 [15].

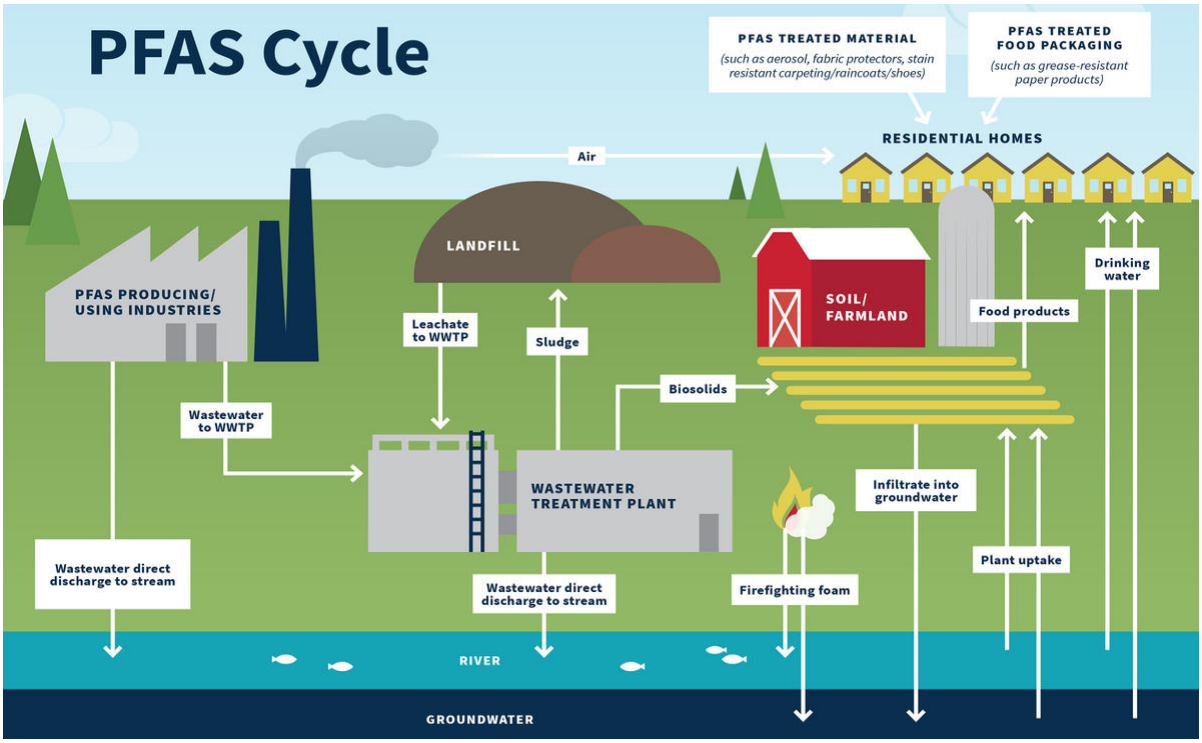

Figure 2.3: PFAS cycle [15]

2.1.5 Case Study: RIVM, The Netherlands

PFAS contamination has been spread throughout the world with extensive surveys carried out in the United States of America because of their large number of fluorochemical production plants. To give an idea on the level of PFAS contamination in various sources, a case study on PFAS contamination in The Netherlands is presented with the recent reports from RIVM, The National Institute for Public Health and the Environment, The Netherlands. Appendix A presents the recent data on PFAS found in drinking water, soil, breast milk and food contact materials. [16–27].

Chemours, a spin-off from DuPont is located in Dordrecht, The Netherlands and it has been in production since the 1970s. The plant majorly used PFOA for fluoropolymer production during its early phase and a number of surveys have been done in the subsequent years to measure the PFAS level in river and groundwater close to the Chemours plant to ensure safe-limit of exposure to humans. Figure 2.4(a) shows the water samples taken from the rivers at various locations near the Chemours plant. Figure 2.4(b) shows the peak levels of PFOA (230 ng/L) in Nieuwe Mass river recorded in the year 2002. PFOA has been banned for use due to high level of PFOA concentrations found in this river which resulted in high level of PFOA accumulated in blood serum of humans (Fig. 2.5). Since 2012, GenX ($C_6F_{11}O_3NH_4$), a short-chain organofluorine chemical, the ammonium salt of hexafluoropropylene oxide dimer acid (HFPO-DA, $C_6HF_{11}O_3$), has replaced PFOA and is being used till date. In 2017, the highest reporting of PFOA in surface water is 12 ng/L even after 5 years of ban [26]. The difference between PFOA and GenX is the presence of an ether linkage (R-O-R), making it a short-chain compound as seen in Figure 2.6.

Note: The ammonium salt of HFPO-DA is GenX. But both exist in the same anionic form ($C_6F_{11}O_3^-$) in water due to deprotonation (H^+) or dissociation (NH_4^+). Hence, GenX and HFPO-DA deliver the same dissolved species.

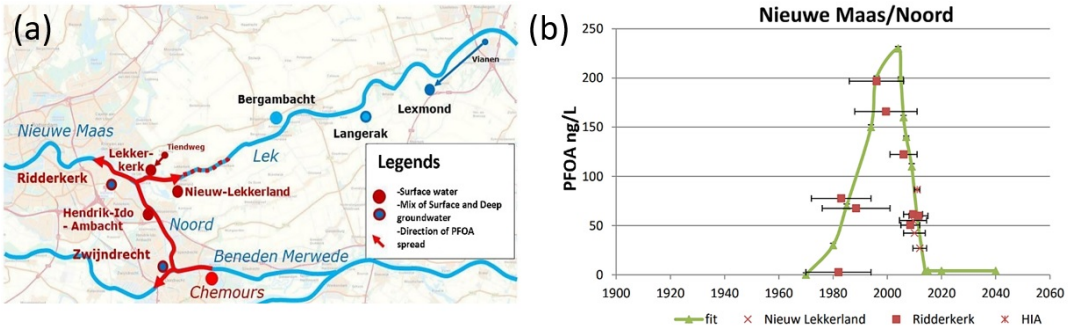

Figure 2.4: (a) Flow of PFOA discharged from Chemours into the river and (b) PFOA concentrations in Nieuwe Mass/Noord river [16]

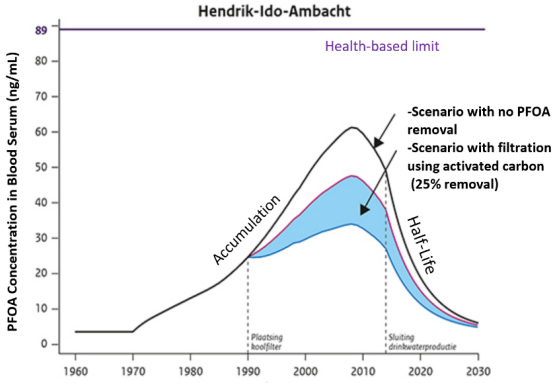

Figure 2.5: PFOA concentration in blood serum of people living near Hendrik-Ido-Ambacht with two scenarios [18]

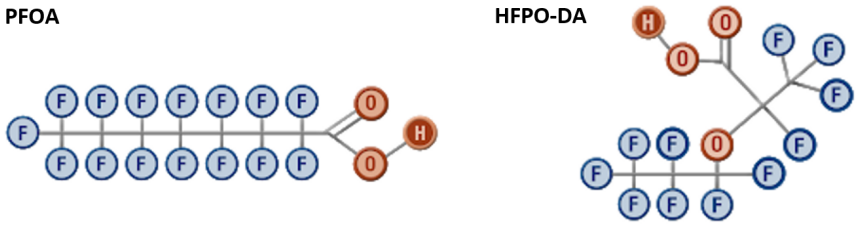

Figure 2.6: Chemical structures of PFOA and HFPO-DA [27]

The short-chains in HFPO-DA (GenX) were thought to be an advantage over PFOA and were considered less harmful to humans. However, current research on the GenX remediation proved that GenX has higher toxicity compared to PFOA and is more easily soluble in water, thus making it more difficult for removal [27].

Safe limits set by RIVM

RIVM has set the following safe limits of PFAS exposure from various sources as listed in Table 2.2 [16–26]. The no-observed-adverse-effect-level (NOAEL) has been derived from repeated oral dose toxicity studies conducted on rats and mice as their genetic and biological characteristics resemble close to those of humans [21].

Table 2.2: Safe PFAS limits in various sources set by RIVM [16–26]

Sources	PFOA	GenX
Air	0.1 mg/kg body weight/day	0.1 mg/kg body weight/day
Soil	0.8 µg/kg	0.8 µg/kg
Drinking Water	87.5 ng/L	150 ng/L
Surface Water	48 ng/L	118 ng/L
Swimming Water	240 ng/L	403 ng/L
Fish	1.5 µg/kg	2.6 µg/kg

2.1.6 HUMAN HEALTH CONCERNS

PFAS make our lives convenient with their anti-stick properties but their comfort comes with a price. The half-life of PFAS in human blood serum ranges from 4 to 7 years. Due to continuous exposure of PFAS from consumption of water, food etc., they keep accumulating in blood over time and this has serious detrimental effects on the human health. The major concerns are kidney, liver and thyroid related issues in general, pregnancy related issues in women and testicular cancer in men [20, 21, 26, 27] as depicted in Figure 2.7. A recent study showed that elevated plasma-PFAS concentration in human blood was associated with the severity of COVID-19 due to their accumulation in lungs [28].

2.2 CURRENT TREATMENT METHODS FOR PFAS REMOVAL

2.2.1 ACTIVATED CARBON TREATMENT

Use of granular activated carbon (GAC) has been extensively studied for PFAS removal due to its relatively low cost. Different types of carbon material, e.g. bituminous coal, coconut and GAC with different pore diameters are used [29]. These filters are commonly found in treatment plants and household water-filter systems and they adsorb natural and synthetic organic compounds. Activated carbon being a highly porous material,

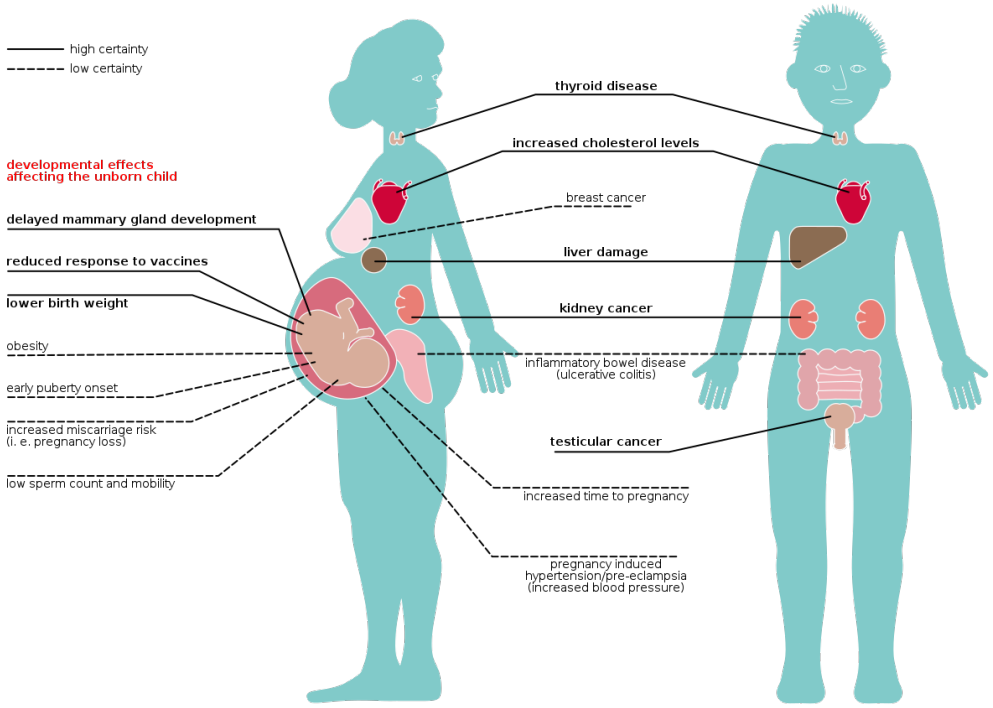

Figure 2.7: Potential effects of PFAS exposure on human health [27]

provides a high surface area for adsorption. Figure 2.8 shows the simulated efficiency of PFOA adsorption with respect to bed volume. Bed volume refers to the minimum solvent required to wet the entire filter. As can be seen, the efficiency greatly depends on the type of coal and the adsorbed PFOA curve flattens over time of treatment due to saturation of adsorbed organic compounds [30, 31].

Advantages: Least-expensive method, large volumes of water can be treated, easy replacement of filters.

Disadvantages: Other organic compounds also adsorb onto the pores thus reducing the efficiency of PFAS removal and short-chain molecules can escape without getting trapped. PFAS is only adsorbed and not degraded, thus requiring a secondary treatment method to treat the used carbon filters.

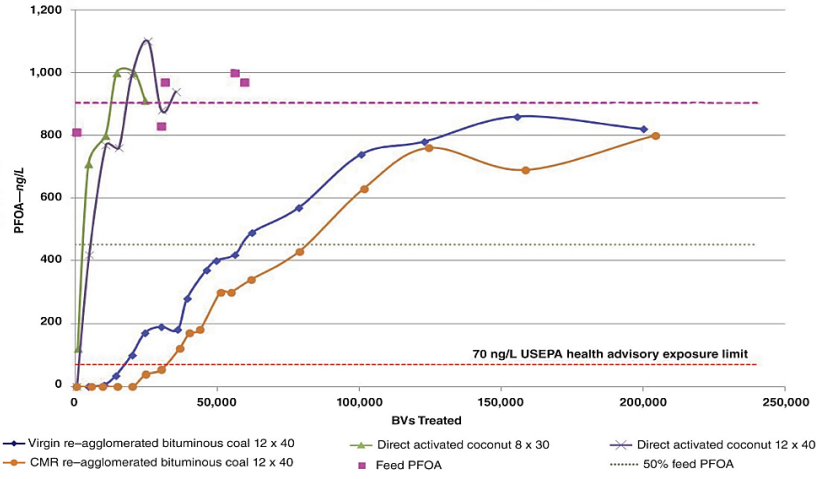

Figure 2.8: Simulated adsorption of PFOA using GAC [29]. The curves represent different types of carbon material used. BV- bed volume, CMR – custom municipal reactivated, USEPA – US Environmental Protection Agency

2.2.2 ION EXCHANGE RESIN

Ion exchange resin is a dual mechanism process of both adsorption and ion exchange happening at the same time to remove the PFAS from water. The hydrophobic non-ionic tail of PFAS adsorbs to the cross-linked polymer of the resin via Van der Waals forces and the anionic head bonds to the fixed ion exchange group (cation) of the resin as shown in Figure 2.9 [32]. Due to the dual mechanism, the size of the treatment system can be reduced to 67% compared to that of GAC system and the results show that the adsorption rate is faster and efficiency of removal is thirteen times more effective compared to GAC [33].

Advantages: Higher efficiency compared to GAC, reduction of the treatment system size.

Disadvantages: Similar to GAC, PFAS is only adsorbed and not degraded, thus requiring an additional process for safe disposal of PFAS. Regeneration of the used resin is expensive.

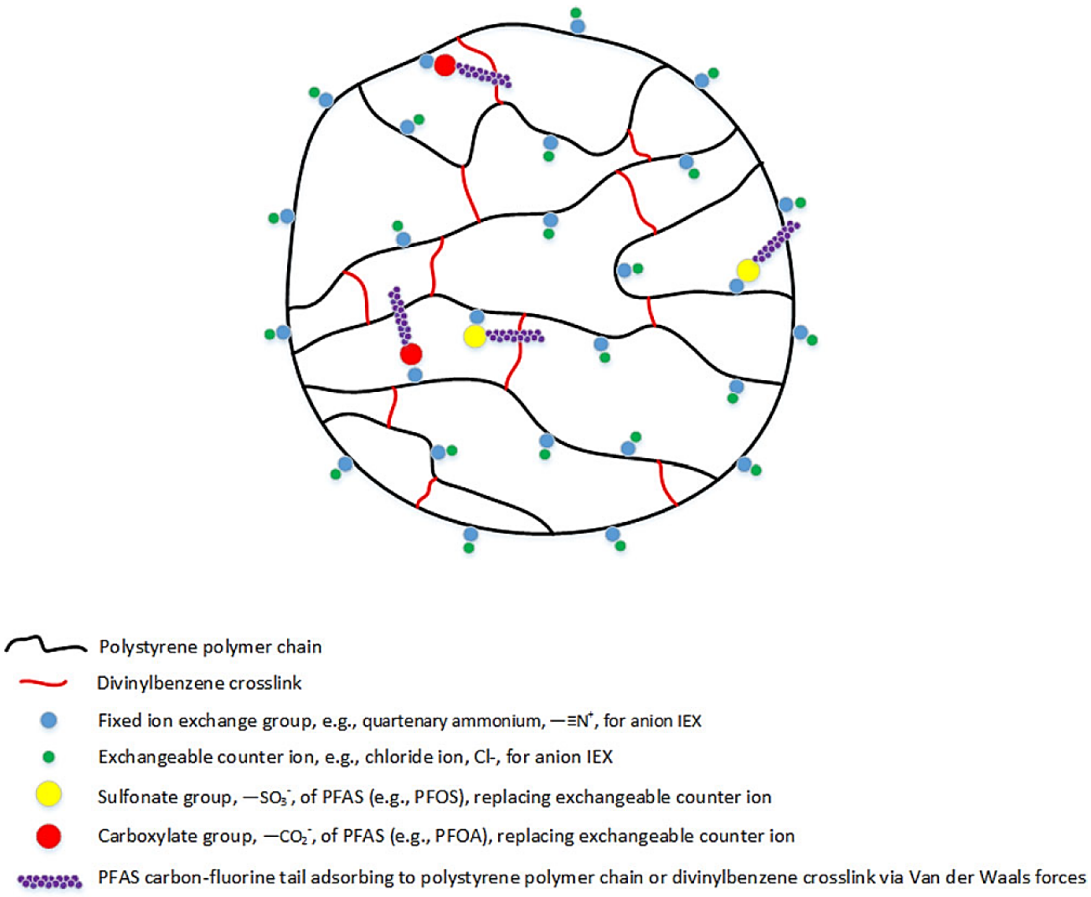

Figure 2.9: Representation of dual mechanism for PFAS removal using ion exchange resin [32]

2.2.3 HIGH PRESSURE MEMBRANES

Reverse osmosis or nanofiltration is extremely effective at removing PFAS. In both cases, pressurized water is forced through a semipermeable membrane that blocks the PFAS from passing through the membrane as seen in Figure 2.10. The size of the pores is much smaller in reverse osmosis membranes than in nanofiltration membranes. Both the methods have been proven to attain a removal efficiency of >90% (Figure 2.11), which is much higher than GAC or ion exchange resin methods [34–36].

Advantages: High removal efficiency, both short and long-chain PFAS molecules can be removed with high repeatability.

Disadvantages: Using high pressure membrane technology is energy intensive and only smaller volumes can be treated. 20% of the feed water is retained as concentrated waste which needs to be disposed again into the environment or needs to be incinerated at temperature >1100°C causing further environmental concerns [34].

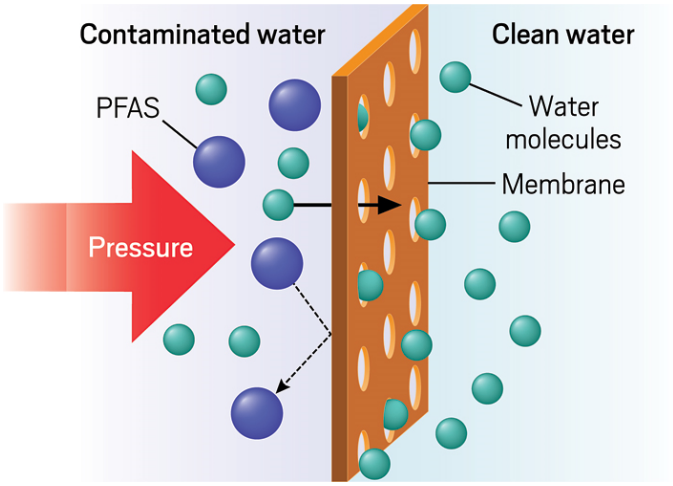

Figure 2.10: Reverse osmosis of PFAS through high pressure membranes [35]

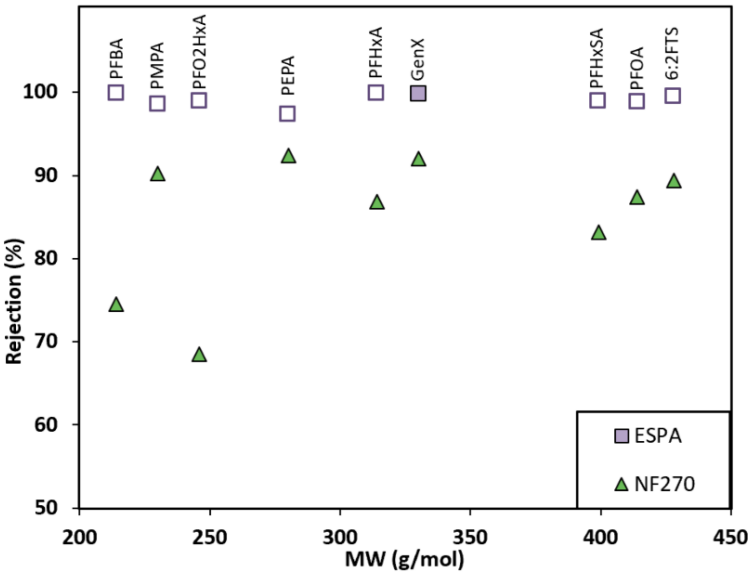

Figure 2.11: Rejection efficiency of PFAS using high pressure membranes (ESPA refers to membrane material used in reverse osmosis and NF270 refers to membrane used in nanofiltration). >97% rejection efficiency of GenX in reverse osmosis [36]

2.3 EAOP USING BDD ANODES

This section explains the role of advanced oxidation processes (AOPs) in water treatment. The types of AOPs and the reactions that take place during the oxidation of contaminants are briefly explained. Among the listed AOPs, the electrochemical advanced oxidation process (EAOP) is the main focus for this survey and a brief overview of the process is given. The role of anode material in EAOP and the potential of using boron-doped diamond over other anode materials are discussed.

2.3.1 ADVANCED OXIDATION PROCESSES

AOPs have received great attention over the last few decades due to their ability to oxidize non-biodegradable organic pollutants into stable biodegradable compounds along with the potential of pathogenic disinfection, deodorization and decolorization [37]. With growing number of complex toxic chemicals, water treatment requires a more powerful oxidizing process, hence the name advanced oxidation process. AOPs are based on the in-situ generation of hydroxyl radicals ($OH^{\bullet}$) that are able to attack and degrade almost any organic compound that comes in contact with them. The hydroxyl radicals are highly reactive, non-selective oxidants that react rapidly with the organic compounds, often close to diffusion-controlled rates through multi-step pathways [38]. The reaction ends up producing shorter organic by-products, or in some cases, the complete mineralization of organic compounds into carbon dioxide, water and inorganic salts as described in Equation 2.1 [39].

$$organic\ compounds + OH^{\bullet} \rightarrow CO_2 + H_2O + inorganic\ ions \tag{2.1}$$

Advantages[40]

1. $OH^{\bullet}$ are highly reactive species with oxidation potential of 2.80 V vs standard hydrogen electrode (SHE).
2. $OH^{\bullet}$ directly react with the organic contaminants by attacking their bond sites and cleaving the bonds to form smaller biodegradable compounds.
3. By-products produced are simpler and do not produce any new toxic compounds.
4. Complete mineralization of organic compounds into CO_2, H_2O and inorganic ions.
5. AOPs do not produce any concentrated sludge that would need secondary treatment as mentioned in the previous chapter in the case of reverse osmosis or ion exchange resin method.

Disadvantages [40]

1. Though $OH^{\bullet}$ are highly reactive, they are short-lived species (20 ns).
2. Presence of chloride and bromide in natural water leads to the formation of free chlorine, perchlorate and bromates that need to be treated using additional processes.

In AOPs, the main processes include (i) Fenton/Photo-Fenton Oxidation; (ii) Ozonation; (iii) Photocatalysis; (iv) Anodic oxidation. The principle behind each process and its disadvantages are as follows [37]:

FENTON/PHOTO-FENTON PROCESS

The Fenton process involves the use of hydrogen peroxide as an oxidant and iron in the form of ferrous ions as a catalyst. Iron (ll) sulfate is commonly used as iron catalyst [41]. The hydroxyl radicals are generated due to the oxidation of Fe^{2+} to Fe^{3+} as described in Equation 2.2. The oxidized Fe^{3+} is then reduced back to Fe^{2+} by another molecule of H_2O_2, forming a hydroperoxyl radical as described in Equation 2.3. Eq.2.2 and Eq.2.3 form a catalytic redox cycle reaction with the oxidation state of iron changing between +2 and +3. Hence the hydroxyl radical generation depends on the rate of redox reaction. The reaction of ferrous ions (Fe^{2+}) with H_2O_2 is several orders of magnitude faster than reaction of ferric ions (Fe^{3+}) with H_2O_2 which results in a slow reaction rate limited by Eq.2.3 [37, 38].

Photo-Fenton process makes use of UV-irradiation to increase the reaction rate due to photoreduction of Fe^{3+} to Fe^{2+}. This increases the overall efficiency of the process and results in additional generation of $OH^{\bullet}$.

$$Fe^{2+} + H_2O_2 \rightarrow Fe^{3+} + OH^{\bullet} + OH^{-} \tag{2.2}$$

$$Fe^{3+} + H_2O_2 \rightarrow Fe^{2+} + OOH^{\bullet} + H^{+} \tag{2.3}$$

Disadvantages [37, 42]

1. Due to insolubility of Fe^{3+} in neutral pH, the reaction proceeds rapidly only under acidic conditions with pH<4.

2. At higher pH, reduction of Fe^{3+} leads to the formation of $Fe(OH)_3$ instead of Fe^{2+} which affects the rate of reaction as illustrated in Figure 2.12.

3. Removal of iron using secondary treatment methods is eventually required.

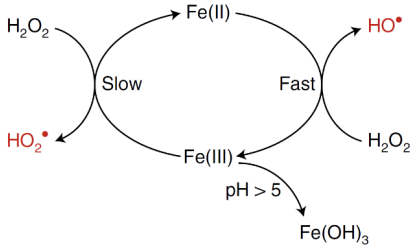

Figure 2.12: Redox cycle in Fenton reaction and the formation of $Fe(OH)_3$ at pH>5 [39]

OZONATION

Ozone (O_3) is a powerful oxidant (2.07 V/SHE) that can react with organic and inorganic compounds. For many years, ozone is used as a disinfectant and also as a pretreatment method for minimization of excess sludge production [38, 43]. Recently, ozonation has gained interest in water treatment as an advanced oxidation process. Ozone either reacts directly with organic compounds through a selective slow reaction (organic pollutants containing amines double bonds, sulfur and activated aromatic rings) or indirectly through rapid non-selective reaction by conversion of ozone into hydroxyl radicals [38].

In the acidic medium, ozone reacts with H^+ to form oxygen and water as described in Equation 2.4. This limits

the reaction of ozone with organic pollutants [44].

$$O_3 + 2H^+ + 2e^- \rightarrow O_2 + H_2O \tag{2.4}$$

In the basic medium, ozone directly attacks the OH^- to generate hydroxyl radicals as described in Eqs. 2.5, 2.6 & 2.7.

$$O_3 + OH^- \rightarrow O_3^{\bullet -} + OH^{\bullet} \tag{2.5}$$

$$O_3^{\bullet -} \rightarrow O^{\bullet -} + O_2 \tag{2.6}$$

$$O^{\bullet -} + H^+ \rightarrow OH^{\bullet} \tag{2.7}$$

The presence of UV increases the generation of hydroxyl radicals through photolysis of ozone as described in Equation 2.8. Photolysis involves the decomposition of water into protons and electrons by means of photons [44].

$$O_3 + H_2O + h\nu \rightarrow O_2 + 2OH^{\bullet} \tag{2.8}$$

Disadvantages [37, 44]

1. The main disadvantage is the poor solubility of ozone in water.
2. Ozonation leads to the formation of toxic by-products like bromate.
3. Since ozone rapidly decomposes to oxygen, the efficiency greatly depends on the gas-liquid transfer of ozone during the process.

PHOTOCATALYSIS

Photocatalysis is similar to photolysis other than a catalyst involved to enhance the production of electron-hole pair from irradiation using UV or visible light. The catalyst is made of a semiconductor material like TiO_2. Upon irradiation, the photon has sufficient energy to excite an electron from the valence band to the conduction band thus creating a hole in the valence band as described in Equation 2.9. The created hole is then recombined with an electron directly from the adsorbed contaminant or from solvent molecules, e.g. water, which are held responsible for the generation of hydroxyl radicals as described in Eqs. 2.10 and 2.11. A schematic representation of the whole process [37–39, 44] is shown in Figure 2.13.

$$TiO_2 + h\nu \rightarrow TiO_2(e^- + h^+) \tag{2.9}$$

$$TiO_2(h^+) + H_2O_{ad} \rightarrow TiO_2 + OH_{ad}^{\bullet} + H^+ \tag{2.10}$$

$$TiO_2(h^+) + OH_{ad}^- \rightarrow TiO_2 + OH_{ad}^{\bullet} \tag{2.11}$$

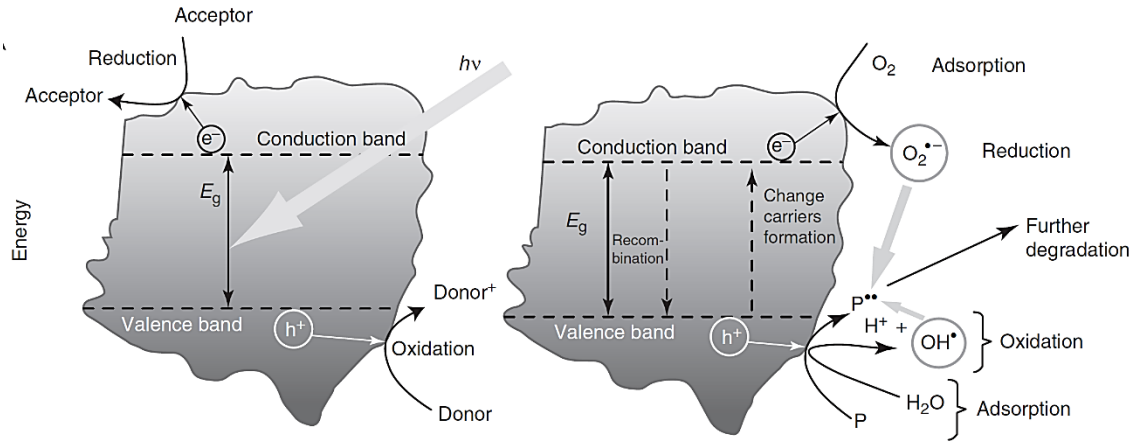

Figure 2.13: (Left schematic) Generation of electron-hole pair upon irradiation with a photon and (Right schematic) Schematic of direct oxidation of contaminant P by direct electron transfer and the hydroxyl radical generation by transfer of electron from adsorbed water molecule to fill the hole in valence band of the TiO_2 semiconductor. The generated hydroxyl radical further reacts with contaminant P and oxidizes it [38]

Disadvantages [37, 38]

1. Full-scale application of photocatalysis has not been demonstrated yet.
2. TiO_2/UV is observed to be very slow as compared to the other AOP processes.
3. Problems due to deactivation, leaching and chemical instability are yet to be studied.

ANODIC OXIDATION

The above mentioned AOPs have their own set of disadvantages like low solubility, requirement of additional UV irradiation, requirement of highly acidic medium, removal of catalysts etc. Hence a much simpler and more powerful oxidation process is required for large scale applications. Electrochemical advanced oxidation process (EAOP) also called as anodic oxidation has emerged as novel water treatment process owing to its simplicity of operation. Anodic oxidation is considered to be versatile due to its increased capability to degrade a wide range of contaminants at ambient temperature and pressure. It involves the generation of hydroxyl radicals due to oxidation of water at the surface of the anode as described in Equation 2.12 [45].

$$H_2O \rightarrow OH^{\bullet} + H^+ + e^- \tag{2.12}$$

Working Principle: The electrochemical setup consists of a cell comprising of two electrodes operating as anode and cathode and an electrolyte which in this case is the contaminated water consisting of some naturally present conducting ions like sulfate and chloride. When an electrical connection is made between the electrodes by supplying a voltage difference, hydroxyl radicals are generated at the anode which break down the organic compounds to CO_2, H_2O and inorganic salts [46].

To understand the principle behind the generation of hydroxyl radicals, the basics behind water electrolysis is explained first. Electrolysis of water, also called as water splitting, is the decomposition of water into hydrogen and oxygen due to the passage of electric current [47]. The anodic and cathodic reactions are described in Eqs. 2.13 and 2.14, respectively.

$$Anode\ (oxidation):\ \ 2H_2O \rightarrow O_2(g) + 4H^+ + 4e^- \quad E^o = +1.23V \tag{2.13}$$

$$Cathode\ (reduction):\ \ 2H^+ + 2e^- \rightarrow H_2(g) \quad E^o = 0.00V \tag{2.14}$$

From the above equations, the standard potential for water splitting can be determined as $E^o_{cell} = E^o_{cathode} - E^o_{anode} = -1.23$ V at 25°C. The value of 1.23 V is based on the thermodynamic value of Gibbs free energy change for the reaction $H_2O \leftrightarrow H_2 + 0.5\ O_2$. This value is at ideal conditions and in practice the water splitting does not occur until a voltage of 1.5 V. The increase in potential required for driving a reaction (e.g. water electrolysis reaction) is termed as overpotential [48]. In experimental conditions, the overpotential greatly depends on the type of material used as electrodes for the oxidation and reduction reactions. The overpotential for a particular material can be determined by measuring the voltage at which a desired current density is achieved.

Electrochemical Oxidation Mechanism:

The oxidation of organic compounds can occur in the following two ways:

(i) Direct electron transfer (DET):

Since the water is not oxidized until a potential of 2.0 V/SHE in EAOP, a wide potential window is available for the direct electron transfer (DET) from the organic compound to the anode as described in Equation 2.15 where R is the contaminant [45].

$$R \rightarrow (R^\bullet)^+ + e^- \tag{2.15}$$

The importance of DET pathway is often overlooked but considered to be the rate-determining step for the oxidation of organic compounds, especially in case of fluorinated organics. Direct electrolysis requires the adsorption of organic compounds onto the anode and the reaction can occur at relatively lower potentials. The direct electron transfer makes the contaminant highly unstable which results in the splitting of the compound to smaller by-products that are further mineralized to water and carbon dioxide in the presence of reactive radicals. The rate of direct electrolysis is limited by diffusion of compounds to the anode surface, slow reaction kinetics and decrease in catalytic activity of the anode due to fouling (chemisorption of contaminants onto anode) [45–49].

(ii) Oxidation by reactive radicals:

Reactive oxygen species (ROS) are unstable molecules containing oxygen that can react rapidly to mineralize organic compounds [50]. When voltage is applied, the intermediates of oxygen evolution like superoxide ($O_2^{\bullet -}$), hydroxyl radicals ($OH^\bullet$) and peroxides (H_2O_2) are formed at the anode surface. Peroxides are further reduced to highly reactive hydroxyl radicals as described in Equation 2.16 [50].

$$H_2O_2 + e^- \rightarrow OH^- + OH^\bullet \tag{2.16}$$

This study mainly focuses on the reaction of hydroxyl radicals with organic compounds. Due to the high oxygen overpotential in BDD-based EAOP, increased efficiency for hydroxyl radical generation is observed within the potential window of the anode material. The reactive radicals react with organic compounds in water through the following two ways:

Direct oxidation: Direct oxidation involves the reaction of physically adsorbed oxygen species (physisorbed $OH^\bullet$) or the chemisorbed active oxygen (oxygen within the lattice in case of metal oxide (MO) anode) with

the organic compounds. The generation of the physisorbed hydroxyl radical as an intermediate species during oxygen evolution reaction is described in Eq. 2.17 where M represents the anode material and M(OH$^\bullet$) represents the OH$^\bullet$ adsorbed onto the M surface. The physisorbed OH$^\bullet$ can further result in the evolution of oxygen as seen in Eq. 2.18 [51]. To improve the efficiency of OH$^\bullet$ formation, it is therefore necessary to use anodes with a wide potential window to favour the reaction in Eq. 2.17 and avoid unwanted side reactions (Eq. 2.18) that lead to oxygen evolution [45, 49, 51].

$$M + H_2O \rightarrow M(OH^\bullet) + H^+ + e^- \tag{2.17}$$

$$M(OH^\bullet) + H_2O \rightarrow M + O_2 + 3H^+ + 3e^- \tag{2.18}$$

In case of active anodes, the anode material reacts with the hydroxyl radical due to strong interaction to form metal oxide as seen in Equation 2.19. This metal oxide further oxidizes the organic compound through a redox couple reaction or leads to the formation of oxygen reaction as describes in Eqs. (2.20) and (2.21), respectively.

$$M(OH^\bullet) \rightarrow MO + H^+ + e^- \tag{2.19}$$

$$MO + R \rightarrow M + RO \tag{2.20}$$

$$MO \rightarrow M + 0.5\,O_2 \tag{2.21}$$

The generated hydroxyl radicals then react with the organic compounds (R) to form water, carbon dioxide and inorganic salts as described in Equation 2.22.

$$R + M(OH^\bullet) \rightarrow M + CO_2 + H_2O + inorganic\ ions \tag{2.22}$$

Non-active anodes are ideal anodes due to their high oxygen overpotential and they do not participate directly in the reaction due to limited interaction of the anode surface with the hydroxyl radicals. Consequently, the hydroxyl radicals are weakly adsorbed onto the anode surface which results in high reactivity compared to the chemisorbed OH$^\bullet$ [49, 52]. This physisorbed OH$^\bullet$ is directly responsible for the mineralization of organic compounds and hence anode material plays an important role in determining the efficiency of the process.

Indirect oxidation: As mentioned earlier, water naturally consists of dissolved salts like sulfate and chloride in parts per million (ppm). EAOP not only leads to the generation of hydroxyl radicals but also promotes the formation of other oxidant species. Indirect oxidation involves the formation of oxidants like sulfate radicals ($SO_4^{\bullet-}$), chloride radicals (Cl$^\bullet$), hypochlorite (ClO^-) and free chlorine (Cl_2) at the anode surface [52, 53]. These oxidants either react directly with the organic compounds or lead to the formation of OH$^\bullet$ to mineralize organic compounds to carbon dioxide and water. The oxidation half-reactions occurring at the anode are as follows (Eqs. 2.23, 2.24, 2.25 and 2.26) [53]:

$$2Cl^- \rightarrow Cl_2 + 2e^- \tag{2.23}$$

$$Cl_2 + H_2O \rightarrow HClO + Cl^- + H^+ \tag{2.24}$$

$$HClO \rightarrow ClO^- + H^+ \tag{2.25}$$

$$SO_4^{2-} \rightarrow SO_4^{\bullet-} + e^- \tag{2.26}$$

The advantages and disadvantages of EAOP over other AOPs can be summarized as follows [40, 52, 53]:

Advantages

- Direct oxidation of organic compounds by applied current between electrodes.
- No requirement of UV irradiation or addition of catalysts.
- EAOP can be incorporated into the water flow system with no additional space requirements.
- The reaction can occur at neutral pH and at ambient pressure and temperature.

Disadvantages

- Formation of by-products like free chlorine, perchlorate etc. which needs secondary treatment for removal.
- The efficiency of the process is highly dependent on the choice of anode material. Hence cost of the anodes can be considered to be a drawback.
- Fouling of anode over time due to formation of oxide layer.

2.3.2 BORON-DOPED DIAMOND ANODES FOR EAOP

The allotropes of carbon have received increased attention in various applications due to their distinct properties. They vary from the lightest material (graphene with sp^2 arrangement) to the hardest material (diamond with sp^3 arrangement). Diamond is known to have exceptional properties like high thermal conductivity, extreme chemical and thermal stability and low friction coefficient. But diamond has failed to receive attention in the electrochemical applications due to its insulating property with a bandgap of 5.47 eV and extremely high inherent electrical resistivity (10^{16} Ω cm) [51, 54].

Recently, a large number of studies has been made on diamond as an electrode material through doping of other elements to reduce its bandgap. Boron which has one electron less than carbon and a relatively small atomic size compared to that of carbon, is doped into diamond as a charge acceptor [54]. Boron is widely preferred as a dopant due to its small charge carrier activation energy (0.37 eV), thus effectively accommodating the carbon lattices [51]. The incorporation of boron introduces mid-gap states to enhance the electrical conductivity and electron-transfer rates which gives diamond p-type semiconducting property, hence commonly called as boron-doped diamond (BDD) [54].

BDD as an electrode material has gained interest recently due to its excellent electronic, chemical and mechanical properties as seen in Figure 2.14.

BDD ANODE PROPERTIES FOR EAOP

Extremely wide potential window: BDD has the widest potential window than any other electrode material as shown in Figure 2.15 [55]. This increases the efficiency of EAOP by favouring the intermediate oxygen evolution reaction through the generation of hydroxyl radicals. BDD has a wide potential window in both aqueous and non-aqueous electrolytes. The oxygen evolution occurs at +2.9 V/SHE and the hydrogen evolution occurs at -1.5 V/SHE [51]. This property gives BDD anode the ability to oxidize a wide range of organic compounds [51, 54–56].

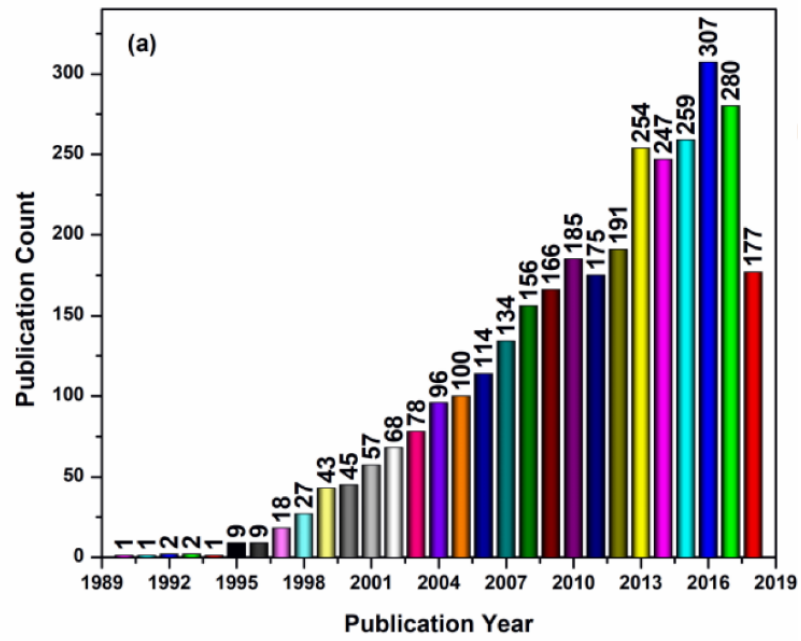

Figure 2.14: Publication output per year from the period 1990 to 2018 on BDD electrodes for electrochemical applications [51]

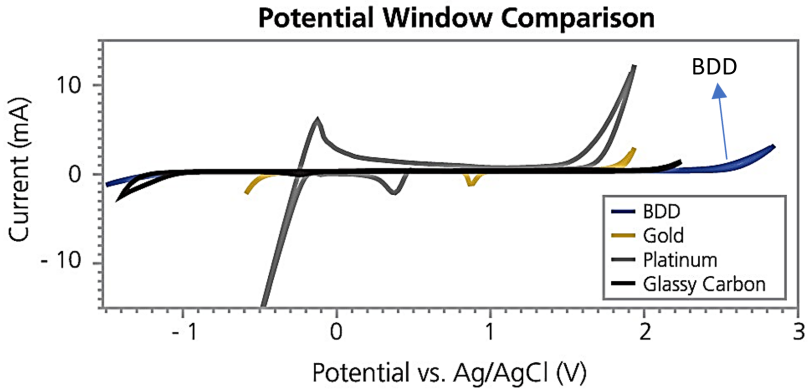

Figure 2.15: Potential window of BDD compared to other electrode materials with Ag/AgCl as reference electrode [55]

Ideal non-active electrode: BDD electrodes are characterized by very slow kinetics of inner sphere reaction like oxygen evolution. This requires very high overpotential for the evolution of oxygen. Due to weak adsorption properties of hydroxyl radicals onto the BDD surface, the physisorbed hydroxyl radicals react rapidly with the organic compounds.

Chemical inertness: Due to the high sp^3/sp^2 ratio of carbon state, BDD is extremely resistant to corrosion and can work under extreme acidic conditions. BDD electrodes are robust and are capable of operation under elevated temperature and pressure.

Resistance to fouling: Since the BDD electrode is non-active (i.e.) resistant to formation of oxide layer on reaction with water, they are able to operate for extended lifetime without delamination. Also, due to weak adsorption properties of BDD, the contaminants present in water do not directly react with the BDD hence fouling of electrodes is negligible.

SYNTHESIS OF BORON-DOPED DIAMOND

High-pressure high-temperature (HPHT) and chemical vapour deposition (CVD) growth techniques have been used for the synthesis of diamond for many decades. For the synthesis of boron-doped diamond, CVD is commercially used due to the advantage of synthesizing doped diamond at low pressure and temperature over the HPHT technique [56, 57].

BDD is deposited onto a growth substrate containing diamond nanoparticles under reactive gas conditions. The suitable gases required for BDD growth are carbon-containing gas like methane, in the presence of hydrogen to form sp^3 carbon and boron-based gas like diborane (B_2H_6) or trimethyl boron $B(CH_3)_3$ to dope boron into the carbon crystal lattice. Adequate supply of hydrogen gas is required to suppress the formation of sp^2 bond and enhance the sp^3 bonded carbon. On the other hand, increased hydrogen concentration leads to slower growth rates. This requires the use of microwave assisted CVD to enable hotter temperatures which is capable of producing high purity material at faster growth rates [51].

Typical growth conditions are plasma temperature of 2500 K, substrate temperature of 1200 K, pressure of 25 mbar, methane concentration of 0.3-1% in hydrogen and microwave power of 1000 – 1300 W. Growth rate of BDD under these conditions is in the range of 0.1 to 2 µm. The properties of BDD greatly depend on the growth conditions, doping concentration, presence of impurities, morphological and crystallographic orientation [51, 56].

Growth substrate: The desirable properties of the growth substrate are low resistivity, high mechanical strength and chemical inertness. Typical growth substrates include silicon (Si) or metals like niobium (Nb), tungsten (W), titanium (Ti), etc. Recently, the growth of BDD on flexible substrates like polyimide was reported [56]. The selection of growth substrate mainly depends on the cost. Si/BDD anode is mostly reported in literature due to its low cost; however, large scale applications involving Si/BDD are not favourable due to brittleness and low conductivity of silicon. The main property determining the compatibility of BDD thin films on the substrate is the coefficient of thermal expansion (CTE). Since the synthesis occurs at elevated temperature, the difference in CTE between the substrate and the BDD thin film can lead to delamination of the BDD thin film. The substrate stability are in the following order: Ta > Si > Nb > W > > Ti [51].

BDD morphology: The growth conditions determine the morphology of the resulting BDD thin film. BDD electrodes are generally polycrystalline due to the ease of production over larger length scales as shown in Figure 2.16 (a) & (b). The grain size and surface roughness vary with growth time leading to thicker BDD films that can be separated from the growth substrate to form freestanding BDD material as shown in Figure 2.16 (a) & (c). Nanocrystalline BDD (NC-BDD) is of sub-micron thickness with surface roughness in the range of nanometers as shown in Figure 2.16 (a) & (d). On the other hand, microcrystalline BDD (MC-BDD) is thicker than NC-BDD with surface roughness and grain size in the range of microns [56].

In general, NC-BDD contains more sp^2 carbon due to the trapping of impurities at grain boundaries. Hence for the application of electro-oxidation, MC-BDD has greater efficiency of degradation compared to NC-BDD [56].

BDD FEATURES AFFECTING ELECTROCHEMICAL PROPERTIES

Boron doping level (B/C ratio):
Diamond can be modified from insulator to metal-like based on the doping level of boron atoms. The doping of boron atoms can vary from 200 to 15000 ppm with a trend that increase in doping increases the electrical conductivity. On the other hand, high boron doping will result in reduced properties of diamond like

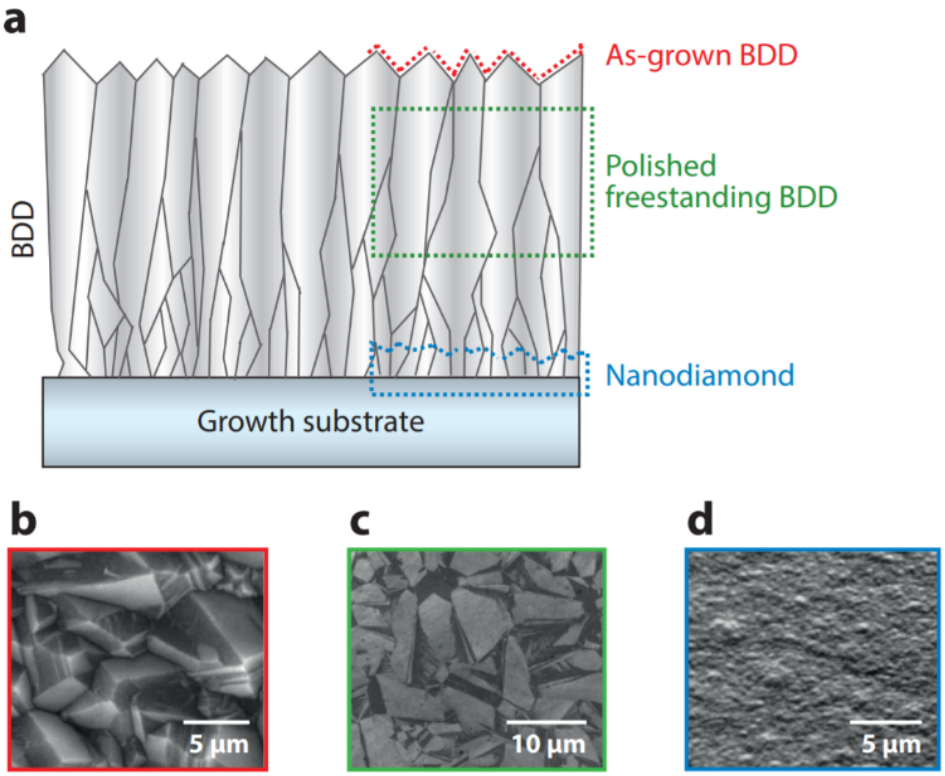

Figure 2.16: (a) Schematic of growth of BDD on a substrate. The process starts with the formation of NC-BDD from the diamond nanoparticles which over time nucleates to form microcrystalline BDD which further nucleates to form polycrystalline BDD with large grains of different orientation. (b) polycrystalline BDD with rough grains (c) polished freestanding BDD (d) nanocrystalline BDD [56]

mechanical strength, chemical inertness etc. With increase in B/C ratio, the overall width of the potential window decrease thus reducing the efficiency of degradation. Also, this can lead to the fouling of BDD electrode over time. Hence an optimum concentration of boron doping is required to find a balance between exceptional diamond properties and electrical conductivity of BDD electrodes [54–57].

sp^3/sp^2 ratio:

BDD can be considered to be a mix of non-active crystalline sp^3 (diamond) and active sp^2 (non-diamond) carbon phases. The boron doping level also controls the distribution of sp^3 and sp^2 carbon. The increase in boron concentration gives rise to non-diamond sp^2 carbon impurities. The higher the sp^2 concentration, the higher the wettability of BDD surface, making it an active anode. This can led to unwanted adsorption of chemical compounds present in water which cause fouling over time. On the other hand, a high ratio of sp^3/sp^2 can give BDD the desired non-active anode behaviour which can lead to the complete mineralization of organic contaminants. It is not possible to achieve a pure sp^3 carbon phase in combination with high boron doping which requires a trade-off between the doping level and the electrical conductivity [54, 56, 57].

The morphology of a microcrystalline BDD electrode, for example, was characterized using AFM (atomic force microscopy) as shown in Figure 2.17. The randomly oriented grains with a high degree of triangular facets due to the exposure of (111) planes represents the diamond crystallites (sp^3 arrangement). The smooth, round, non-faceted grains represents the presence of amorphous carbon (sp^2 arrangement) [58].

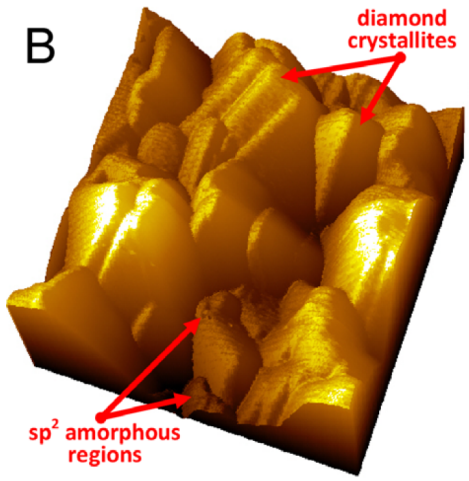

Figure 2.17: AFM image (1 x 1 μm^2) of BDD electrode showing the presence of both diamond crystallites and sp^2-rich regions [58]

2.4 BDD ANODES FOR PFAS DEGRADATION

This section explains the electrochemical advanced oxidation (EAOP) process for PFAS degradation using boron-doped diamond anodes. A comparison of various parameters affecting the efficiency of degradation is made based on the available literature. The observed degradation mechanism, its intermediate and end products are explained schematically. The contradictions on the rate-determining step and the limitations of using EAOP for PFAS degradation is highlighted.

2.4.1 LITERATURE ON PFAS DEGRADATION USING BDD ANODES

Till date, only 12 research articles have been published that demonstrated the use of boron-doped diamond as anode in EAOP for degradation of PFAS. The split up of research articles based on the PFAS type is as follows:

- **8 research articles on PFOA**
- **3 research articles on PFOS**
- **1 research article on GenX**

This section only discusses the literature on PFOA and GenX since they are used in this work. The researchers mainly focused on finding the degradation mechanism and its rate-determining step by varying the concentration of electrolytes. The efficiency is calculated based on the rate of defluorination and removal of PFAS. Also, the formation of unwanted by-products like perchlorate has been discussed.

PFOA

Electrochemical cell setup

The following researchers performed the degradation of PFOA using a commercial flow cell with commercial BDD electrodes. Advanced Diamond Technologies, USA and Condias, Germany are the two main suppliers of commercial BDD flow cells as mentioned in the literature. The researchers carried out their experiments

with a view of applying it on an industrial scale, hence less focus was made on the characterization of the BDD electrode before and after degradation.

The following table (Table 2.3) mentions the different cathode, anode, cell volume, effective electrode area and electrode gap mentioned in the articles:

Table 2.3: List of experimental parameters of the electrochemical cell setups for PFOA degradation using BDD anodes reported in literature

Literature	Anode	Cathode	Cell Volume	Electrode Area	Electrode Gap
Schaefer et al. [59]	Nb/BDD	Tungsten	250 mL	38 cm^2	4 mm
Ochiai et al. [60]	Nb/BDD	Pt-deposited Ti	100 mL	77.4 cm^2	10 mm
Urtiaga et al. [61]	Nb/BDD	Tungsten	250 mL	42 cm^2	8 mm
Zhuo et al. [62]	Si/BDD	Ti sheet	40 mL	8.5 cm^2	30 mm
Barisci et al. [63]	Si/BDD	Si/BDD	600 mL	81 cm^2	10 mm
Gomez et al. [64]	Nb/BDD Si/BDD	Tungsten SS	500 mL 1000 mL	42 cm^2 70 cm^2	8 mm 5 mm
Garcia et al. [65]	Si/BDD	Si/BDD, Pt, SS, Zirconium	1000 mL	63 cm^2	10 mm
Ensch et al. [66]	Nb/BDD	Nb/BDD	750 mL	105 cm^2	3 mm

Electrolytes

Groundwater naturally consists of certain dissolved inorganic salts as seen in Table 2.4.

Table 2.4: Characteristics of groundwater as mentioned in [59]

Salts	Concentration (mg/L)
Fluoride	<0.2
Chloride	18
Sulfate	25
Nitrate	5.5
Perchlorate	0.15

As discussed in the previous chapter, indirect oxidation through the generation of oxidants like sulfate radicals, chloride radicals, free chlorine, perchlorate etc. can increase the efficiency of degradation. To study the effects of indirect oxidation and to find the rate-determining step, the following electrolytes have been used. On the other hand, to determine if hydroxyl radicals are responsible for the rate-determining step, hydroxyl scavengers like tert-butyl alcohol are used.

(i) Sodium Sulfate (Na_2SO_4): When sodium sulfate is dissolved in water, they split into sodium (Na^+) and sulfate (SO_4^{2-}) ions. Due to indirect oxidation, sulfate ions turn into free radicals of the form $SO_4^{\bullet -}$ or $S_2O_8^{\bullet -}$. Sulfate radicals are highly reactive with the oxidation potential ranging from 2.5 – 3.1 V/SHE which is comparable or higher than hydroxyl radicals (2.80 V/SHE) [67]. The average lifetime of sulfate radicals are 30-40 µs which is much longer than hydroxyl radicals (20 ns) [68, 69]. Hence sulfate radicals can increase the efficiency of degradation.

(ii) Sodium Chloride (NaCl) or Sodium Perchlorate ($NaClO_4$): At high voltage (>2 V), the presence of chloride ions in water can lead to the formation of oxidants like chloride radicals ($Cl^{\bullet}$), free chlorine (Cl_2) and hypochlorite ions (ClO^-) [70]. The hypochlorite ion is less reactive compared to $OH^{\bullet}$ or $SO_4^{\bullet -}$ due to its oxidation potential value of 1.63 V/SHE [71]. The presence of these oxidants are again observed to increase the efficiency of degradation. But free chlorine and perchlorates are unwanted by-products that need to be removed to maintain the safe limits of drinking water [59].

(iii) Tert-Butyl Alcohol (TBA): To study the effect of hydroxyl radicals on the degradation efficiency, radical

scavengers are used. Tertiary-butyl alcohol lacking α-hydrogen is commonly used as a hydroxyl scavenger due to its higher reactivity with $OH^{\bullet}$ with a reaction rate constant (3.8-7.6 x 10^8 mol^{-1} s^{-1}) [72]. It effectively reacts with the hydroxyl radical to form an inert intermediate like a dimer [73]. This decreases the reaction of $OH^{\bullet}$ with organic compounds and can be useful in studying the effect of $OH^{\bullet}$ generation rate to determine the rate constant for PFAS degradation.

Effect of input parameters on degradation efficiency

(i) Effect of current density: Degradation efficiency normally increases with increase in current density due to the increase in voltage for efficient electron transfer and the increase in generation of $OH^{\bullet}$. This trend in increase of PFOA degradation as well as defluorination can be seen in Figure 2.18 [61] . On the other hand, further increase in current density can cause increased energy consumption and also favours the oxygen evolution reaction instead of intermediate hydroxyl formation reaction [74, 75].

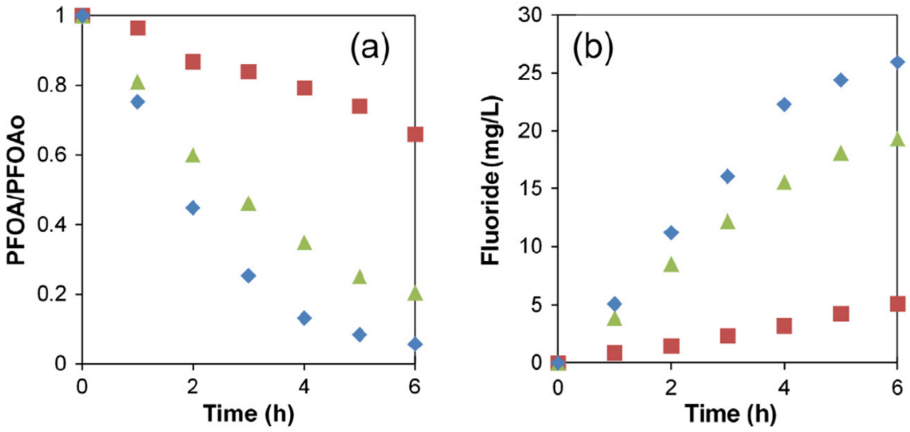

Figure 2.18: Effect of applied current density on the (a) PFOA concentration and (b) Fluoride concentration. (red) j = 5 mA/cm^2, (green) j = 10 mA/cm^2, (blue) j =20 mA/cm^2 where j represents the current density [61]

(ii) Effect of pH: Degradation efficiency is less affected with the change in pH between acidic and neutral regions. At high alkaline conditions, the performance is inhibited due to more OH^- that were adsorbed on the active sites of the electrode. Figure 2.19 explains the trend observed with change in pH. The degradation rates of PFOA were in the order pH 3 > pH 9 > pH 12 [62].

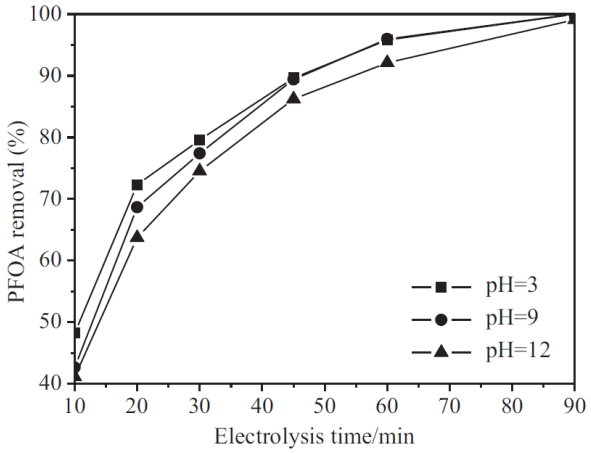

Figure 2.19: Effect of pH on the PFOA degradation [62]

(iii) Effect of initial PFOA concentration: With increase in PFOA concentration, more molecules reach the BDD surface leading to higher removal rates due to PFOA degradation. On the other hand, high concentration of PFOA has no significant influence on the degradation efficiency due to the unavailability of enough $OH^{\bullet}$ radicals. Hence, PFOA concentration has very little effect on the degradation efficiency as can be seen in Figure 2.20 [62].

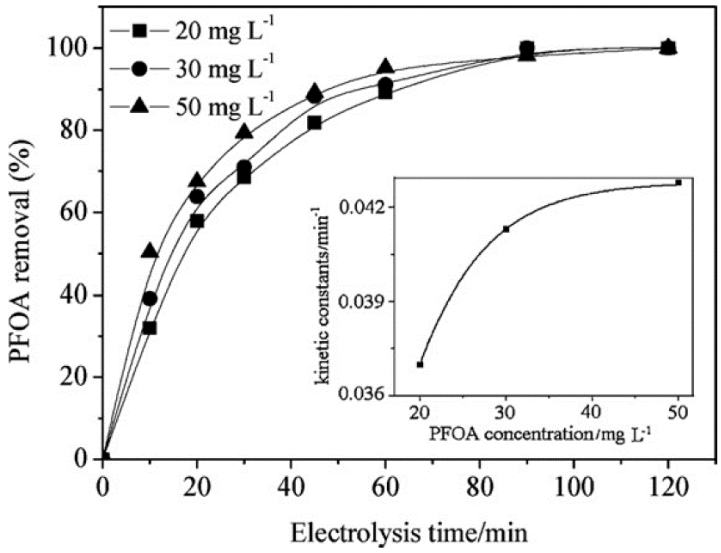

Figure 2.20: Effect of initial PFOA concentration on the degradation efficiency. The inset illustrates the pseudo-first order kinetic constant with respect to PFOA concentration [62]

(iv) Effect of electrolyte concentration: Degradation efficiency normally increases with increase in electrolyte concentration due to the increased production of oxidants formed by indirect oxidation. This gives rise to increased generation of sulfate radicals, chloride radicals, free chlorine, hypochlorite etc. that actively react with the organic compounds to degrade it. However, with further increase in electrolyte concentration, voltage between the electrodes decrease, which decreases the degradation efficiency and more energy is spent on indirect oxidation to create free radicals rather than to directly oxidize the organic compounds. This requires the use of an optimum concentration of electrolyte to obtain the maximum degradation efficiency.

(v) Effect of electrolyte temperature: With increase in temperature, the degradation efficiency increases due to the increase in indirect oxidation that leads to the production of oxidants like sulfate radicals, chloride radicals, free chlorine, hypochlorite etc.

Degradation mechanism

The first step in the mechanism is the direct electron transfer from the PFOA molecule to the BDD anode. This creates a highly unstable PFOA radical which undergoes Kolbe decarboxylation process to form C_7F_{15} radical. The C_7F_{15} radical then forms an unstable alcohol of the form $C_7F_{15}OH$ due to interaction with $OH^{\bullet}$ which later splits into F^- and short-chain compound $C_7F_{13}OF$. $C_7F_{13}OF$ again reacts with water and loses another F^- to form $C_6F_{13}COOH$. This compound again reacts in the above mentioned steps to form further shorter intermediates and later, completely mineralizes to F^- and CO_2 by repeating the CF_2 unzipping cycle steps as illustrated in Figure 2.21.

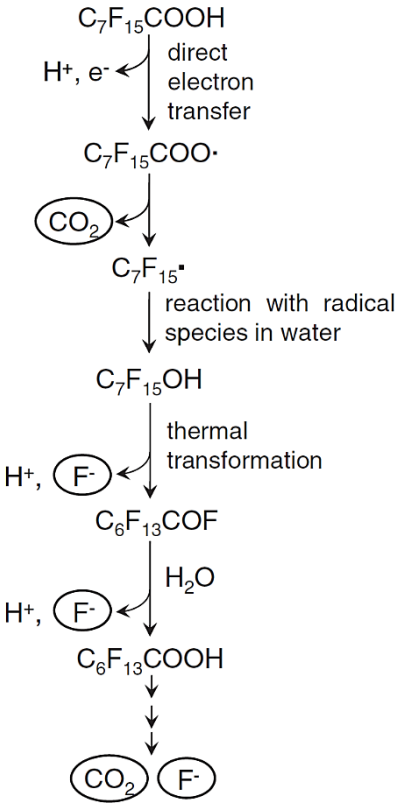

Figure 2.21: Schematic representation of electrochemical degradation mechanism of PFOA leading to the formation of F^- and CO_2 as end products [60]

Rate-determining step

In chemical kinetics, the rate of a reaction is determined by the slowest step called as rate-determining step or rate-limiting step [76]. As seen above there are a number of reactions occurring during PFOA degradation. The three possible rate-determining steps are:

(i) Direct oxidation through direct electron transfer: This can be confirmed when the rate constant does not vary with change in concentration of radical scavengers.

(ii) Oxidation through hydroxyl radical: This can be confirmed through the use of tert-butyl alcohol which should decrease the rate constant of the reaction if $OH^{\bullet}$ oxidation is the rate-determining step.

(iii) Indirect oxidation: This can be confirmed by decreasing the concentration of sodium sulfate or sodium chloride which decreases the generation of oxidants like sulfate radicals, chloride radicals, free chlorine, hypochlorite etc. Due to this decrease, the rate of the reaction also decreases which confirms indirect oxidation to be the rate-determining step.

Schaefer et al. [59], Barisci et al. [63], Gomez et al. [64], Garcia et al. [65] and Ensch et al. [66] have mentioned direct oxidation through electron transfer as the rate-determining step. Ochiai et al. [60] and Zhuo et al. [62] have pointed to direct oxidation through electron transfer as the rate-determining step at low current density and with increase in current density, oxidation through hydroxyl radicals favour the rate-determining step. Urtiaga et al. [61] has mentioned oxidation through hydroxyl radical as the rate-determining step.

Comparison of BDD morphology on PFOA degradation

As mentioned in Section 2.3.2, the morphology of the BDD anode can influence the efficiency of degradation. Gomez et al. [64] have compared the microcrystalline (MCD) and ultrananocrystalline (UNCD) boron-doped diamond on the PFOA degradation efficiency. Since nanocrystalline BDD traps impurities at grain boundaries, there are higher levels of sp^2 compared to microcrystalline BDD [56]. This fact is supported with the rate of defluorination and the removal of total organic carbon (TOC) being higher in microcrystalline BDD than in ultrananocrystalline BDD as seen in Figure 2.22 (a) and (b).

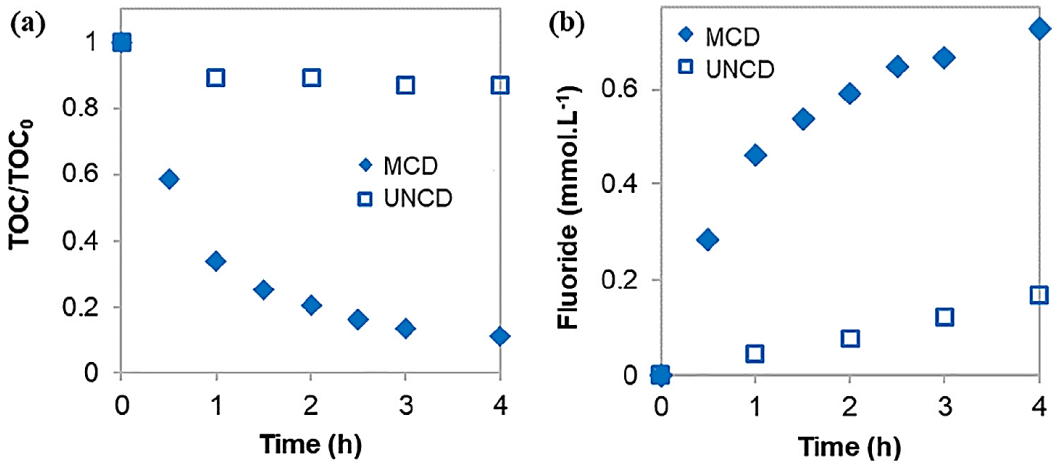

Figure 2.22: Comparison of B-doped MCD and UNCD on the (a) removal efficiency of total organic carbon (TOC) and (b) rate of defluorination during degradation of PFOA [64]

GENX (HFPO-DA)

GenX (HFPO-DA) with the inclusion of an ether bond makes it a short-chain organofluorine compound compared to PFOA. GenX was initially thought to be easily degradable due to the ether bond but the steric hindrance of GenX has resulted in difficulty of degradation using EAOP. This is due to the ineffective electron transfer from the carboxylic head group due to the presence of CF_3 at alpha position [77].

Till date, very limited research is reported on GenX (HFPO-DA) degradation. Bao et al. [77] studied the oxidation of GenX based on $SO_4^{\bullet-}$ oxidative degradation using UV/persulfate and reported that <5% of GenX was degraded whereas 26% of PFOA was degraded in 3 hours (Fig. 2.23). Adding to that, <5% GenX degradation was completely attributed to direct UV oxidation and not to sulfate radicals ($SO_4^{\bullet-}$). In their next research [78], they studied the oxidation of hexafluoropropylene oxide tetramer acid (HFPO-TeA) using UV/persulfate and reported that HFPO-TeA depolymerized to hexafluoropropylene oxide trimer acid (HFPO-TA) which then depolymerized to HFPO-DA (GenX) and not further, which supports their previous finding. This was due to the steric hindrance by the -CF_3 branch in HFPO-DA which blocks the trajectory of $SO_4^{\bullet-}$ from reaching the carboxylic group for successful electron transfer.

Pica et al. [79] studied the electrochemical oxidation of HFPO-DA using a BDD anode in combination with nanofiltration and reported that $SO_4^{\bullet-}$ was capable of enhancing HFPO-DA oxidation. They reported that their finding was in contrast to the claim by Bao et al. whose experiments were carried in alkaline solution which reduces the generation of $OH^{\bullet}$ from sulfate radicals, thereby reducing the degradation efficiency.

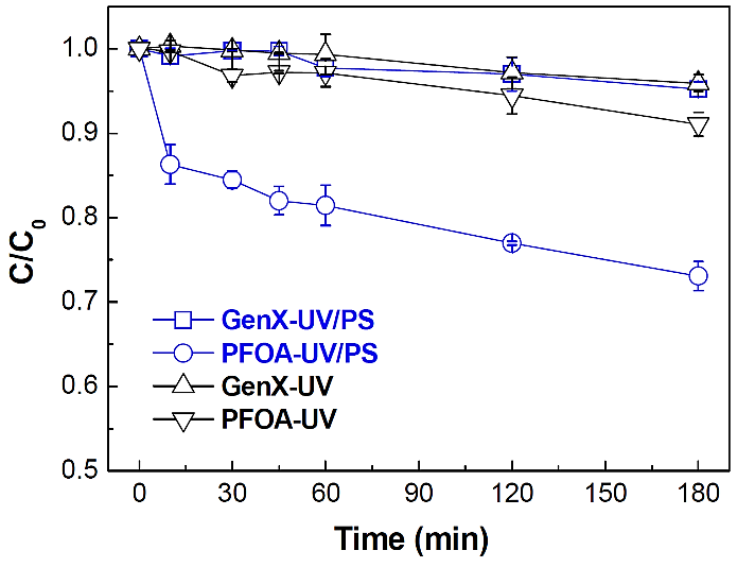

Figure 2.23: Degradation efficiency of GenX and PFOA under UV and combination of UV/Persulfate conditions [77]

Summary of Literature Review

This literature review serves a way to understand why PFAS are called "Forever Chemicals". Exposure to PFAS has potential effects on human health and the environment due to their inability to degrade naturally. The current available treatment methods are ineffective as they fail to degrade PFAS, hence requiring safe disposal of the concentrated PFAS sludge back into the environment. Advanced oxidation processes (AOPs) could effectively degrade PFAS by breaking them into smaller biodegradable compounds owing to the formation of highly reactive radicals. Electrochemical advanced oxidation process (EAOP) has an advantage over other AOPs due to its simplicity in operation and the ease with which the process can be incorporated into the existing flow system of the water treatment plants. The only main disadvantage of EAOP is the formation of by-products like perchlorate and free chlorine during degradation that require additional treatment methods to meet the safe drinking water standards.

Boron-doped diamond (BDD) anodes having a wide potential window and extreme chemical stability can effectively mineralize PFAS into fluoride and CO_2. Results presented by various research articles demonstrate that BDD anodes are effective in degrading PFAS compounds with an efficiency greater than 95%. The input parameters of EAOP have a direct effect on determining the efficiency of PFAS degradation. Although a clear schematic representation of the PFOA degradation mechanism is illustrated, it is still unclear which oxidation mechanism determines the rate-limiting step.

Due to the ban of PFOA in The Netherlands, GenX, a short-chain organofluorine compound, is currently being used in fluorochemical production plants as they are thought to be easily degradable. However, the results demonstrate that the degradation of GenX is more difficult compared to that of PFOA. This is due to the ineffective electron transfer from the carboxylic head group due to the presence of CF_3 at alpha position and thus failing to degrade it through bond cleaving. Research on GenX degradation using BDD anodes has not been explored in-depth yet. Above-sketched contradictions and current knowledge gap form the base for my research proposal on closing the gap by performing design of experiments on the electrolytes and by testing the efficiency of GenX degradation using a parallel plate setup with BDD anode and platinum (Pt) cathode.

3

KNOWLEDGE GAP AND RESEARCH OBJECTIVES

This chapter illustrates the possible oxidation mechanisms reported in current available literature. The contradictions on the rate-determining step and the present knowledge gap are mentioned. Finally, the research objectives on closing this knowledge gap are discussed by conducting experiments in three different phases.

3.1 INTERPRETATION

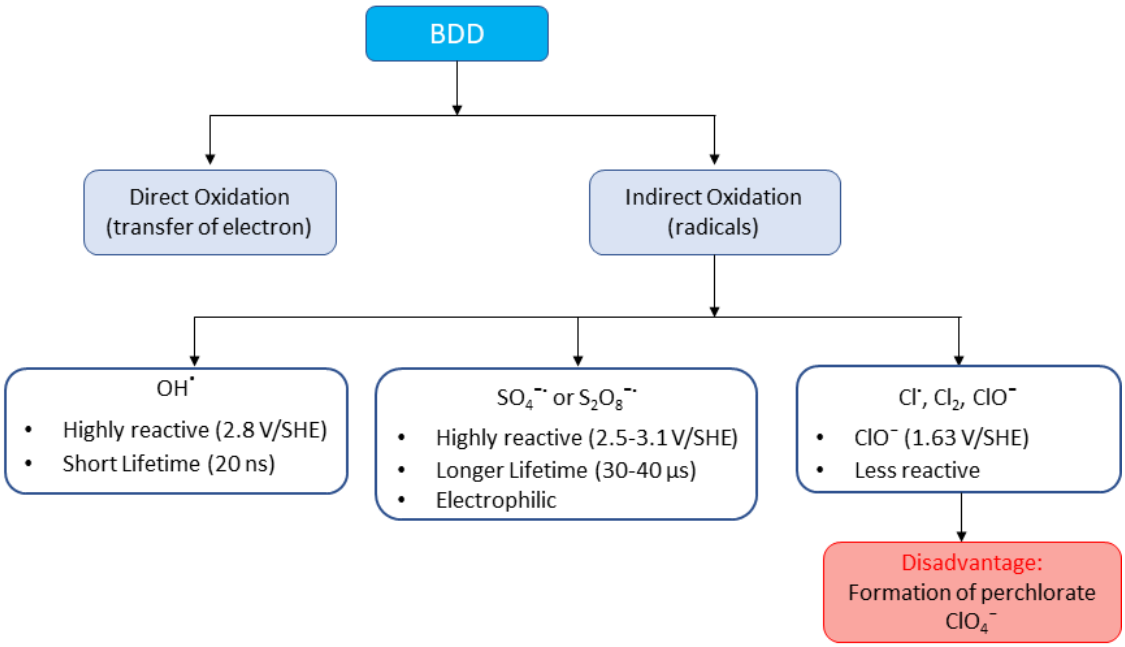

Figure 3.1: Flowchart illustrating the possible oxidation mechanisms for PFAS degradation using BDD anodes

Electrochemical oxidation using BDD anodes for most common organic pollutants is mostly influenced by the generation of hydroxyl radicals which in most cases will be the rate-limiting step. However, in the case of PFAS degradation, the rate-determining step is the oxidation reaction through direct electron transfer (DET) as supported by a total of seven research articles mentioned in section 2.4.1. However, one article [61] re-

ported the oxidation reaction through hydroxyl radicals to be the rate-limiting step. The above figure (Figure 3.1) illustrates the possible oxidation mechanisms responsible for PFAS degradation using BDD anodes.

In the case of HFPO-DA (GenX), two articles [77, 78] reported that sulfate radicals are ineffective in GenX degradation using UV/persulfate. On the other hand, one article [79] on EAOP using BDD anode in combination with nanofiltration reported that sulfate radicals are involved in the first step of GenX degradation. These results create a bit of ambiguity on the factors that influence the rate-limiting step.

3.2 KNOWLEDGE GAP

The 12 available research articles on PFAS degradation using BDD anodes are more inclined towards replicating an industrial approach. Hence, the experiments were performed using commercial flow cells and commercial BDD anodes. Results from these articles are mainly focused on the degradation and defluorination efficiency. These factors create the following knowledge gap:

- The degradation mechanism of GenX is not yet explored in detail.
- There is no research on GenX degradation solely using BDD anodes in EAOP.
- Contradictions exist on the role of sulfate radicals in GenX degradation.
- Electrochemical and surface characterization of the BDD anodes before and after PFAS degradation have not been performed.
- Surface morphology of BDD anode with respect to PFAS degradation efficiency still needs to be explored in-depth.
- The relationship between BDD surface morphology and the bubble formation on the BDD anode surface during PFAS degradation is not yet explored.
- Contradictions exist on the rate-determining step in PFAS degradation.

3.3 RESEARCH OBJECTIVES

In order to close the existing knowledge gap on PFAS degradation using BDD anodes, the following research objectives are formulated:

Phase 1

- To perform an extensive characterization of the BDD anode before degradation.
- To study the role of sulfate radicals on GenX degradation.
- To study the effects of electrolyte concentration, current density, chloride radicals and radical scavenger on GenX degradation.
- To compare the degradation and defluorination efficiency between GenX and PFOA.
- To propose a possible degradation mechanism of GenX in electrochemical oxidation.
- To find out the rate-determining step in GenX degradation.

- To characterize the BDD anode after GenX degradation and elucidate the differences.

Phase 2

- To characterize the surface morphology of BDD anode and relate it to GenX degradation and defluorination efficiency using three different commercial electrodes.

Phase 3

- To study the bubble formation on BDD anode during degradation using visual and electrochemical observations.
- To relate the bubble formation with the surface morphology of BDD anode.

With the above mentioned objectives, an in-depth knowledge on BDD morphology and the factors that directly affect the degradation efficiency of GenX in EAOP can be obtained.

4

MATERIALS AND METHODS

This chapter lists the materials required for degradation experiments. The various surface and electrochemical techniques to characterize the BDD anodes and analytical methods to determine the degradation and defluorination efficiency are described. The methodology for performing degradation experiments using a in-house fabricated electrochemical cell is briefly explained.

4.1 MATERIALS

4.1.1 CHEMICAL REQUIREMENTS

PFAS, electrolytes and radical scavenger required for performing degradation are mentioned in Table 4.1.

Table 4.1: Chemical requirements

PFAS	1. Hexafluoropropylene oxide dimer acid (GenX) 2. Perfluorooctanoic acid (PFOA)
Electrolytes	1. Sodium sulfate 2. Sodium perchlorate 3. Sodium chloride
Radical scavenger	tert-butyl alcohol

4.1.2 BDD ANODES

Thin-film boron-doped diamond (6 µm thick, boron concentration 2500 ppm) electrodes were purchased from NeoCoat, Switzerland. BDD was coated on a pre-treated niobium substrate (50 x 25 mm^2, 2 mm thick), uniformly on both sides including the edges, using a hot-filament chemical vapor deposition (HFCVD) reactor. Neocoat (Nb/BDD) electrodes are used to complete the Phase 1 objectives. For comparison between different electrodes in Phase 2 and Phase 3, two other electrodes were purchased. MCD Nb/BDD electrodes (12 µm thick) prepared using HFCVD were purchased from DiaCCon GmbH, Germany. A polished freestanding BDD electrode (1 mm thick, boron concentration 3 x 10^{20} atoms cm^{-3}) was purchased from Mintres B.V., The Netherlands.

4.2 SURFACE CHARACTERIZATION OF BDD ANODES

Various microscopy and spectroscopy techniques are employed to characterize the surface of BDD anodes. Before and after each electrode characterization, the BDD anodes are cleaned separately in acetone, ethanol and D.I. water using an ultrasonic bath for 15 minutes each.

4.2.1 SCANNING ELECTRON MICROSCOPY

Scanning electron microscopy (SEM) measurements are performed with a JEOL JSM-6010LA scanning electron microscope, at 10 keV and using a secondary electron detector. SEM analysis is performed over a range of magnifications (1000x to 20000x) to observe the surface morphology and to check for any surface defects related to BDD coating before and after degradation. Since all BDD anodes are conductive, they are placed on to the sample holder without the use of adhesive carbon tape to avoid contamination of the BDD anodes.

4.2.2 RAMAN SPECTROSCOPY

Raman spectroscopy measurements are performed with a Horiba LabRAM HR setup, equipped with an argon ion laser operating at 514 nm and a spectral resolution of ~0.3 cm^{-1}. Measurements are taken at multiple locations of the BDD anode to check for the variation in sp^3/sp^2 ratio. Measurements are performed before and after electrochemical degradation to observe any changes in sp^3/sp^2 ratio due to anodic oxidation. The acquisition time is optimised to increase the signal-to-noise (S/N) ratio. Raman spectra are recorded over a range of 200 cm^{-1} to 2000 cm^{-1}.

4.2.3 ATOMIC FORCE MICROSCOPY

Atomic force microscopy (AFM) measurements are performed to study the surface topography of the BDD anodes. AFM measurements are done using a Bruker Dimension Edge™ in tapping mode with antimony n-doped silicon tip. AFM scans are performed with a pixel resolution of 256 x 256 and a scan rate of 0.6 Hz. Post-processing of the AFM data is done using Gwyddion v2.57 software. The use of adhesive conductive tapes are also avoided here.

4.2.4 CONTACT ANGLE MEASUREMENT

Contact angle measurement is a quantitative analysis to study the wettability of the BDD anode surface by a liquid. Contact angle is defined as the angle made by the liquid at the three phase boundary where solid, liquid and gas intersect. The measurements are performed using a Theta Lite optical tensiometer. A Hamilton microliter syringe is use to dispense the D.I. water with a droplet size of 3 µL. An optical camera is used to track the changes in contact angle after the droplet makes contact with the surface of BDD anode and the software OneAttension actively calculates the contact angle through Young-Laplace fit. Since contact angle measurement is highly sensitive due to human handling, several measurements are taken along a line and the average value is calculated. Contact measurements are also performed before and after degradation to observe the changes due to anodic oxidation.

Surface free energy (SFE) of the BDD anode is also analyzed using the same equipment. It uses two polar solvents (D.I. water and Ethylene Glycol) and one dispersive solvent (Di-iodomethane). The droplet size of

each solvent is 2 µL. The contact angle made by each solvent is directly analyzed by OneAttension software and it calculates the SFE using Fowkes hypothesis ($\gamma_{total} = \gamma^d + \gamma^p$) where γ^d and γ^p are the dispersion and polar component of the surface free energy calculated by the software using the measured contact angle of three solvents.

4.3 ELECTROCHEMICAL CHARACTERIZATION OF BDD ANODES

Electrochemical characterization measurements are performed using a multichannel Metrohm Autolab potentiostat with eight an 8 x M101 channel and a 1 x FRA2M impedance analysis module. Measurements are done in a three-electrode configuration, BDD as the working anode with an active surface area of 1 cm^2, platinum mesh (2 cm x 2 cm) as the cathode, and Ag/AgCl as the reference electrode. The data are analysed using Metrohm Nova software. The electrochemical cell setup for electrode characterization is shown in Figure 4.1.

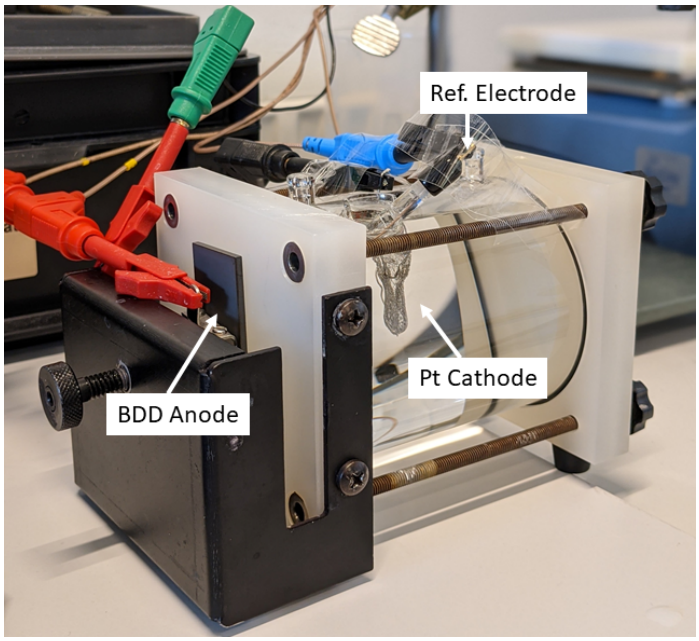

Figure 4.1: Electrochemical cell setup for electrode characterization

4.3.1 LINEAR SWEEP VOLTAMMETRY

Linear Sweep Voltammetry (LSV) is a potentiodynamic technique in which the current at the working electrode is measured while the applied potential is swept linearly in time with a specific scan rate. Any peak in the current signal corresponds to the direct oxidation of a certain species at the BDD anode. To check for the direct oxidation of chloride and radical scavenger at the BDD anode, LSV measurements are performed. The direct oxidation can be checked either by changing the concentration of the known species or by changing the scan rate which directly affects the anodic peak current. The voltammograms are iR compensated with the electrolyte resistance R_s obtained from electrochemical impedance spectroscopy (EIS).

4.3.2 CYCLIC VOLTAMMETRY

Cyclic voltammetry (CV) is similar to LSV except that the potential is swept back to reach the initial set value. CV is a technique in which the oxidation (E_{pa}) and reduction potential (E_{pc}) of a species can be found from

the anodic (i_{pa}) and cathodic peak (i_{pc}) in the current signal, respectively as shown in Figure 4.2. To determine the potential window and the background current of the BDD anode, cyclic voltammetry is performed in 0.1 M KNO_3 electrolyte and the voltammograms are iR compensated.

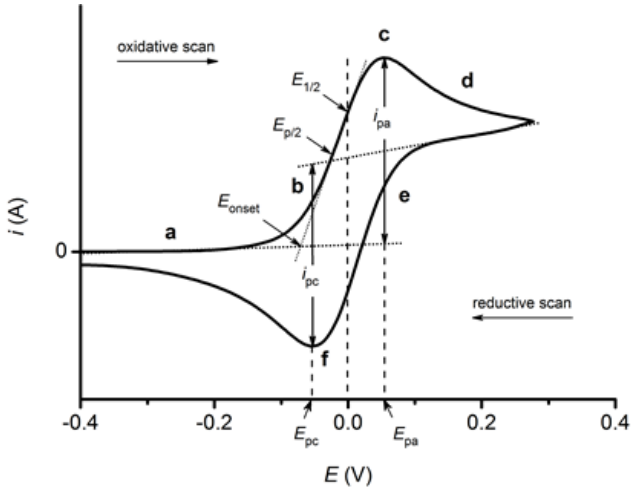

Figure 4.2: Cyclic voltammogram illustrating the oxidation and reduction peak [80]

4.3.3 FERROCYANIDE REDOX REACTION

To study the heterogeneous electron transfer (HET) processes which are responsible for the oxygen evolution (4 electrons transfer, inner-sphere reaction) at the BDD anode, ferrocyanide redox couple ($Fe(CN)_6^{3-/4-}$) is used. Ferrocyanide redox couple undergoes oxidation and reduction through inner-sphere reaction as they are able to penetrate the inner Helmholtz plane and are very sensitive to the electrode surface. As a result, CV using ferrocyanide redox couple is performed to determine the electrochemical surface characteristics of the BDD anode. Cyclic voltammetry is performed in 0.1 M KNO_3 electrolyte containing 1 mM ferrocyanide. The potential range is set between -0.4 V and 0.8 V and voltammograms (iR compensated) are measured at different scan rates varying from 0.025 V/s to 0.8 V/s.

4.4 ELECTROCHEMICAL DEGRADATION

Electrochemical degradation experiments (Phase 1) are performed in a single compartment electrochemical cell made of polypropylene with a 3D printed cap to hold the electrodes. Neocoat Nb/BDD electrode with an effective surface area of 22.6 cm^2 is used as the working anode and a platinum mesh is used as the cathode placed parallel to either side of the anode with an electrode spacing of 10 mm. All experiments are conducted in batch mode at room temperature (approximately 22°C) with an electrolyte volume of 400 mL containing 15 mg/L of HFPO-DA (GenX). Electrolytes used in the experiments are sodium sulfate and sodium perchlorate at varying molar concentrations. The electrolyte concentrations are chosen to simulate the ionic conductivity of groundwater. To study the effect of chloride and reactive chlorine species in the degradation, sodium chloride is added in different molar concentrations to a background electrolyte of 0.02 M Na_2SO_4. To study the effect of hydroxyl radicals in the degradation, tert-butyl alcohol is used as radical scavenger in selected experiments. The degradation experiments are carried out at different applied current supplied by a Keithley 2400 Sourcemeter with a maximum output of 1 A and 200 V and the resulting cell voltage is continuously monitored. The electrolyte solution is stirred using a magnetic stirrer at 300 rpm to increase mass transfer. The initial and final pH (after degradation) of the electrolyte are observed using VWR Dosatest pH test strips.

Each experiment is conducted for 4 hours with samples collected every 30 minutes. At the selected intervals, the power source is turned off with the electrolyte being continuously stirred and a sample of 2 ml is collected and stored in a LightSafe polypropylene micro centrifuge tube. The electrochemical degradation setup for Phase 1 experiments is shown in Figure 4.3

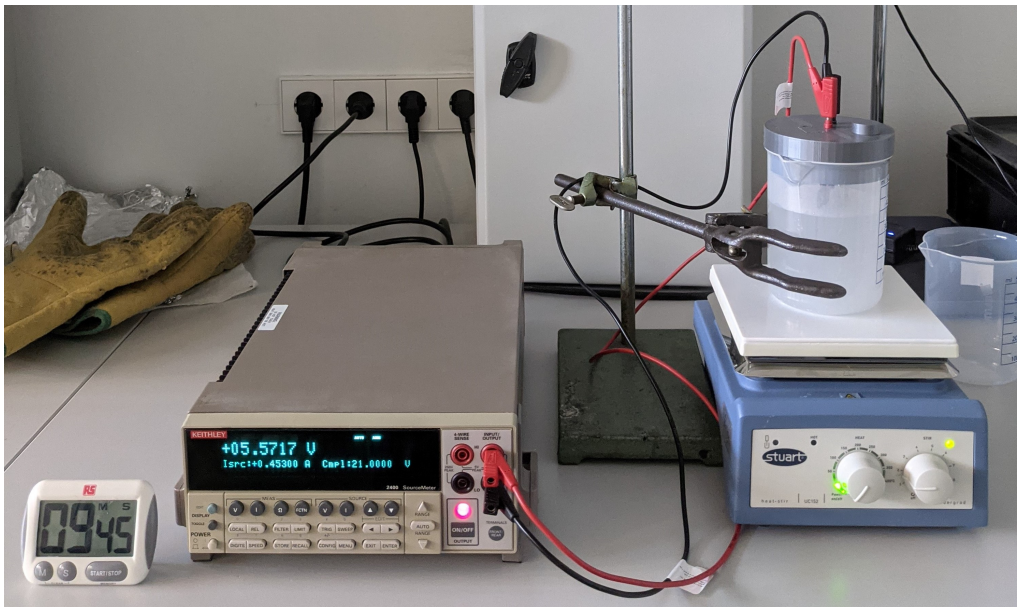

Figure 4.3: Electrochemical degradation setup for Phase 1 experiments

For electrochemical degradation experiments in Phase 2 to compare between different BDD anodes, the setup shown in Figure 4.4 is used. Since the three electrodes are of different sizes, this setup is used to expose only one side of the BDD anode with an effective surface area of 1 cm^2.

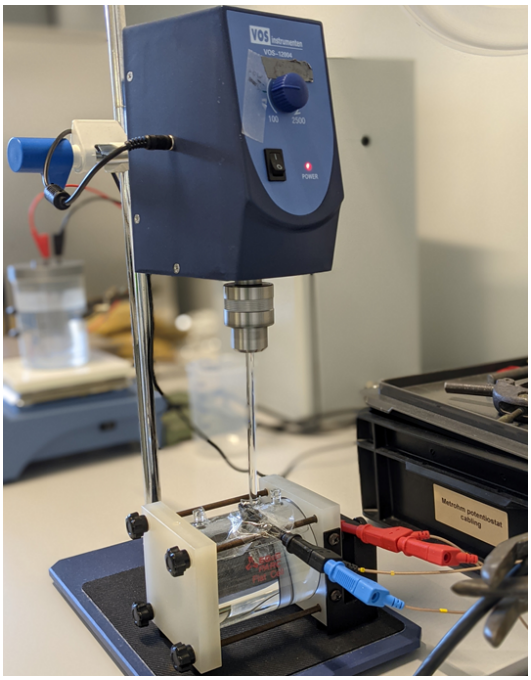

Figure 4.4: Electrochemical degradation setup for Phase 2 experiments

Since two experiments of 4 hours each are performed in a day, Figure 4.5 shows how the samples are collected.

The pipette tips after sample collection are placed in a orderly manner to avoid confusion and the samples collected in black centrifuge tubes are seen in the right side of the figure. The pH is measured before, mid and end of each degradation.

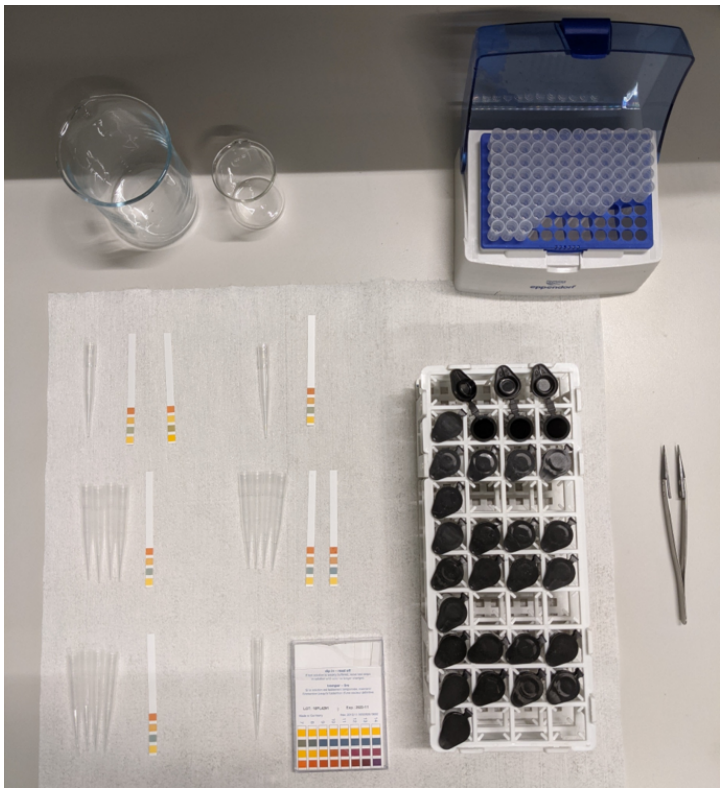

Figure 4.5: Sample collection methodology showing the used pipette tips, used pH strips and black centrifuge tubes for sample collection

4.5 ANALYTICAL METHODS

4.5.1 DPD METHOD

N, N-diethyl-p-phenylenediamine (DPD) reagent is used for free chlorine detection. Free chlorine oxidizes DPD reagent and gives a pink color that can be quantitatively measured at 551 nm using a UV-Vis spectrophotometer. Since the DPD method is highly time sensitive and reacts with ambient light, the quantification results did not follow a desired pattern. Hence, only qualitative detection of free chlorine is made.

4.5.2 HIGH PERFORMANCE LIQUID CHROMATOGRAPHY

To estimate the efficiency of degradation, the concentration of HFPO-DA or PFOA at different time intervals is measured using high performance liquid chromatography (HPLC). The HPLC system (Knauer Smartline) consists of a degasser, a pump, an automatic sample injector with an injection volume of 10 µL, a column oven (40°C) and a UV-Vis detector as shown in Figure 4.6. The HPLC system is equipped with a Phenomenex Kinetex® C18 column (100 mm x 4.6 mm, 2.6 µm). A mixture of 20 mM potassium dihydrogen phosphate (35%) and methanol (65%) is used as mobile phase in isocratic mode. The flow rate is set at 0.6 mL/min for HFPO-DA and 0.8 mL/min for PFOA. The detection was monitored at λ = 200 nm. The UV excitation wavelength of HFPO-DA and PFOA is checked with a Shimadzu UV-2600 (Fig. 4.7).

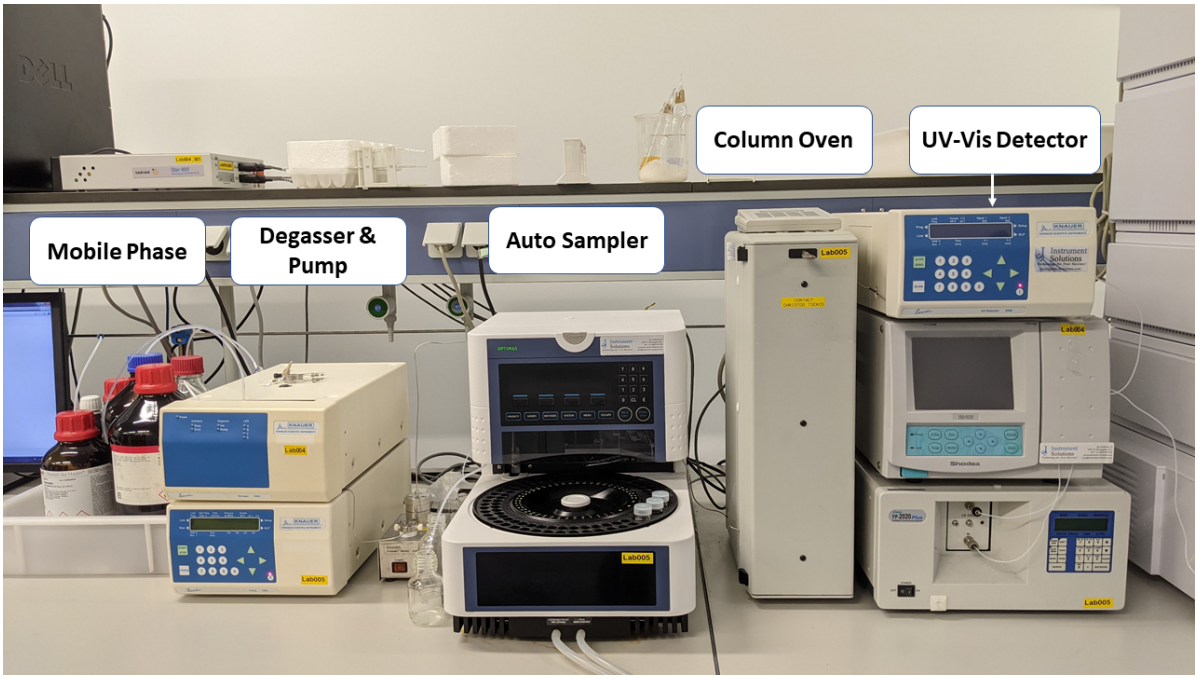

Figure 4.6: High performance liquid chromatography (HPLC) setup

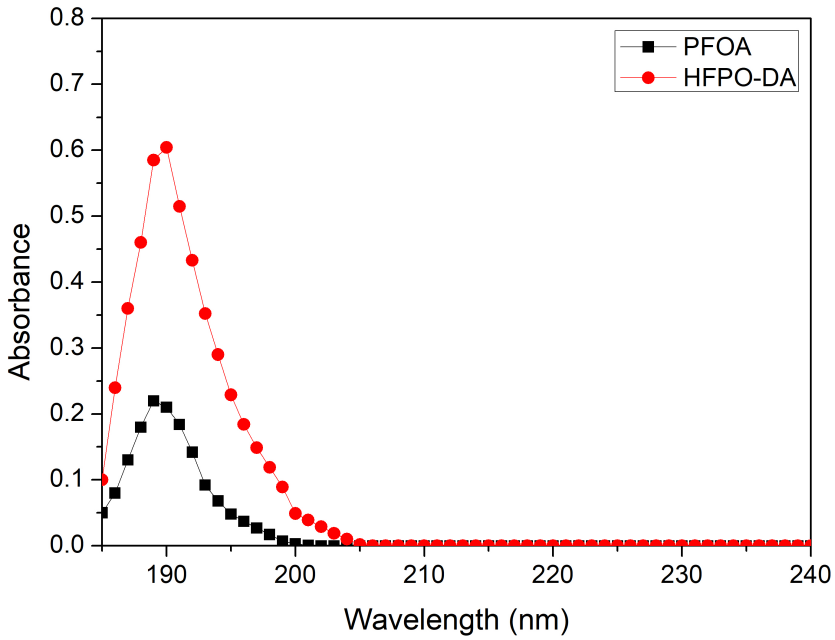

Figure 4.7: UV excitation wavelength of HFPO-DA and PFOA. The wavelength in HPLC detection was set at 200 nm after calibration to avoid noise from deep UV.

4.5.3 ION CHROMATOGRAPHY

To confirm the complete degradation/mineralization of HFPO-DA and PFOA, the concentration of fluoride (F^-) is measured using an ion-chromatograph system (DX-120, DIONEX) (Fig. 4.8) consisting of a separation column (IonPak AS12A, 200 mm x 4 mm) and a suppressed conductivity detector. The mobile phase consists of an aqueous solution of 1 mM Na_2CO_3 and 1 mM $NaHCO_3$ and the flow rate is set at 1.3 mL/min. Other anions such as chloride and sulfate are also measured. The retention times of F^-, Cl^- and SO_4^{2-} are 2.9 min,

3.5 min and 13 min, respectively (Fig. 4.9). Additionally, the peak at 6.5 min corresponds to chlorate (ClO_3^-) which is a by-product formed due to the direct oxidation of chloride (Cl^-). The area of a peak relate to the concentration of an ion species and the concentration value (ppm) is directly resulted by calibrating the system with known concentrations of respective ion species.

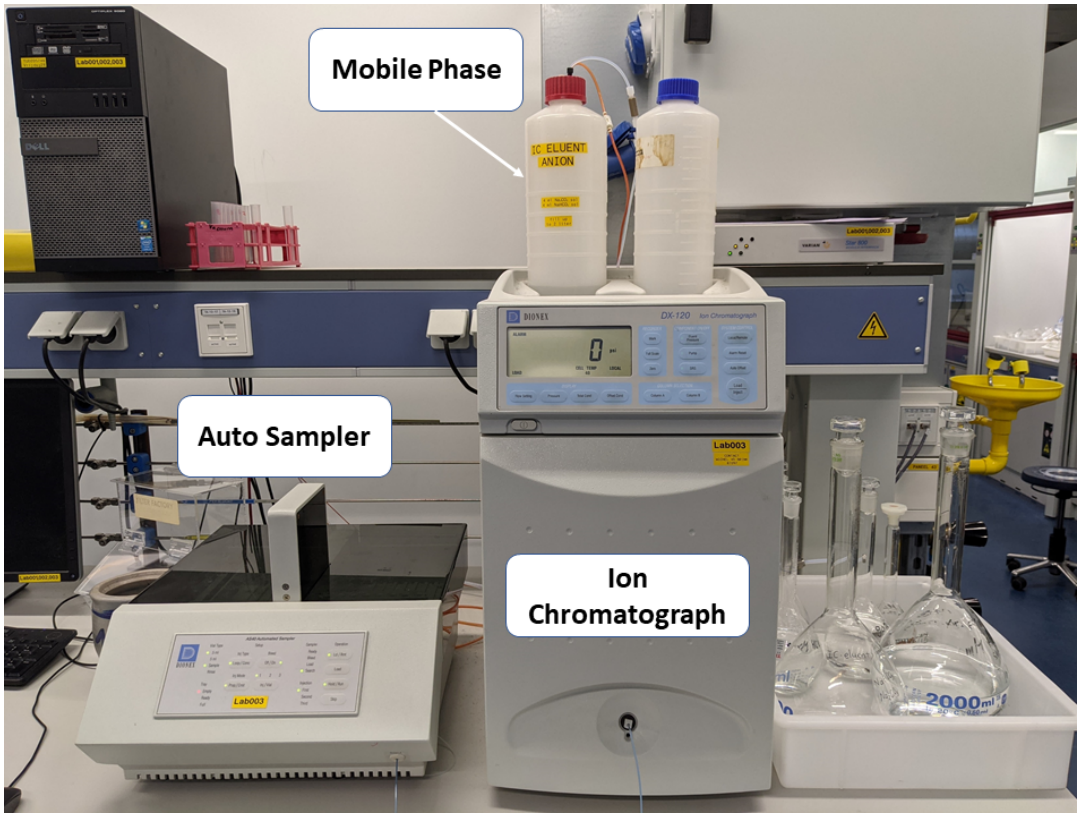

Figure 4.8: Ion Chromatography system with an auto sampler

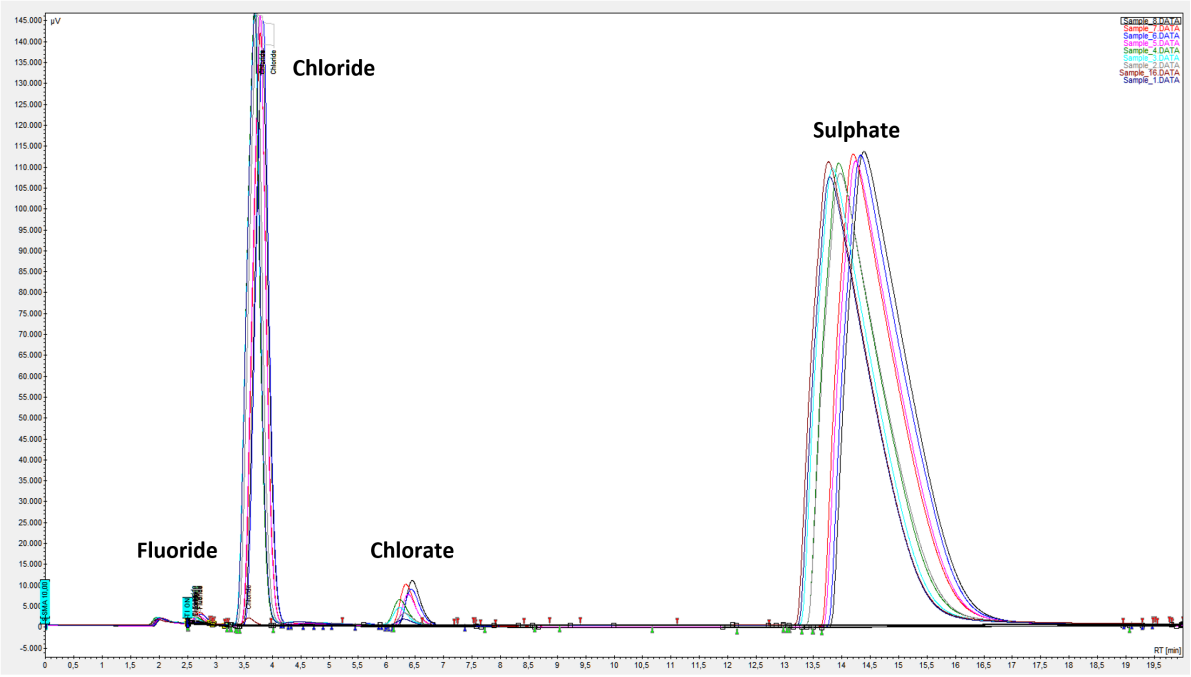

Figure 4.9: Chromatogram showing the peaks corresponding to F^-, Cl^-, ClO_3^- and SO_4^{2-} at different retention times

4.5.4 LIQUID CHROMATOGRAPHY-MASS SPECTROMETRY

The intermediates of HFPO-DA degradation were qualitatively analyzed using an ultra-performance liquid chromatography (UPLC) coupled with high-resolution mass spectrometry (LC-MS) as shown in Figure 4.10. Samples from individual time points were diluted 1:100 with H_2O and 2.5 µL of each sample was analyzed. Reverse phase chromatography was performed using a UPLC BEH (1.0 x 100 mm, 1.7µm, Waters, Acquity) separation column coupled online to a QE plus Orbitrap mass spectrometer (Thermo Scientific, Germany) operated in polarity switching, thereby alternating ES+ and ES- modes. Buffer A consisted of 0.1% formic acid in LC-MS grade water and buffer B consisted of 0.1% formic acid in LC-MS grade acetonitrile. A flow rate of 50 µL/min was maintained using an Acquity Ultra Performance LC pump system (Waters, Milford, United States). After sample injection, 10% B was kept constant over 2.5 minutes, followed by a linear gradient to a solvent composition of 90% B over 10 minutes, which was kept constant for further 2.5 minutes until back-equilibration to solvent start conditions. The full scan was acquired over the mass range of 75–500 m/z at a resolution of 70k and an AGC target of 1e6. External calibration was performed using the Pierce LTQ Velos ESI Positive Ion Calibration Solution before performing the sample analysis. Sample runs were analyzed using QualBrowser part of the Thermo Scientific Xcalibur software tool.

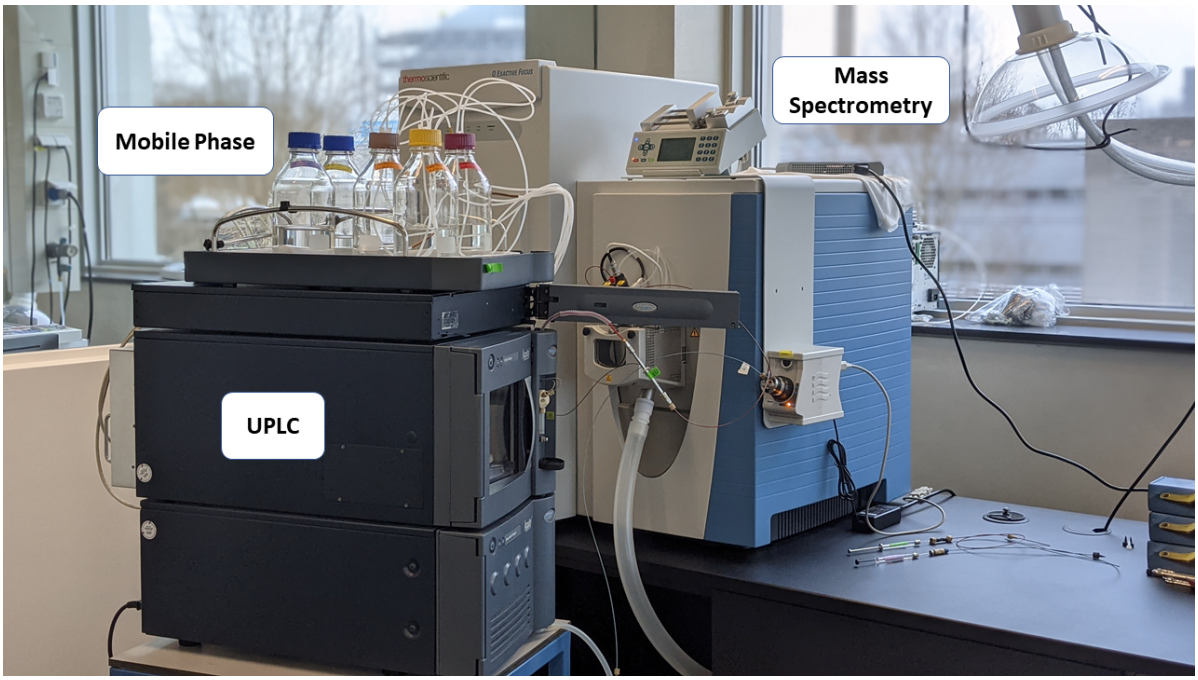

Figure 4.10: Liquid chromatography-mass spectrometry (LC-MS) setup

5

Results and Discussion

This chapter presents the results and discussion of experiments carried out in order to fulfill the research objectives. As mentioned earlier, this chapter is divided into 5 parts. Part 1 describes the BDD anode characterization before electrochemical degradation. Part 2 deals with the electrochemical degradation of GenX using BDD anodes and it forms the core of this research. Part 3 describes the changes in BDD anode after degradation observed through surface and electrochemical characterization. Parts 1, 2 and 3 relate to the research objectives mentioned in Phase 1. Part 4 discusses the comparison of different BDD anodes on the GenX degradation and defluorination efficiency (Phase 2). Part 5 presents a study on the bubble formation on BDD anodes during anodic oxidation (Phase 3).

5.1 Part 1: BDD Anode Characterization before Degradation

This section presents the surface and electrochemical characterization results of the Neocoat Nb/BDD anode with which GenX degradation experiments are conducted.

5.1.1 SEM Analysis

The SEM images in Fig. 5.1 illustrate the surface morphology of the Neocoat Nb/BDD electrode taken at different magnifications. The irregular topography observed is due to the roughness generated during pretreatment of the niobium surface prior to deposition. The BDD surface represents a cauliflower-like morphology [81] likely caused by renucleation [82] occurring during the growth of the polycrystalline diamond coating. The average size of the BDD surface facets is between 0.5-1 µm (Fig. 5.1 (B)). Irrespective of the Nb roughness, the diamond grains are uniformly distributed and no surface defects are observed.

5.1.2 AFM Analysis

The forward scan AFM data are processed using the Gwyddion software. Fig. 5.2 (A) presents the AFM topographic image of the BDD coating. A root-mean square surface roughness of about 860 nm and a maximum peak height of 5.44 µm is observed. The ratio of surface area to projected area is calculated to be 1.106. Fig. 5.2 (B) shows the surface facets of the BDD coating in AFM analysis.

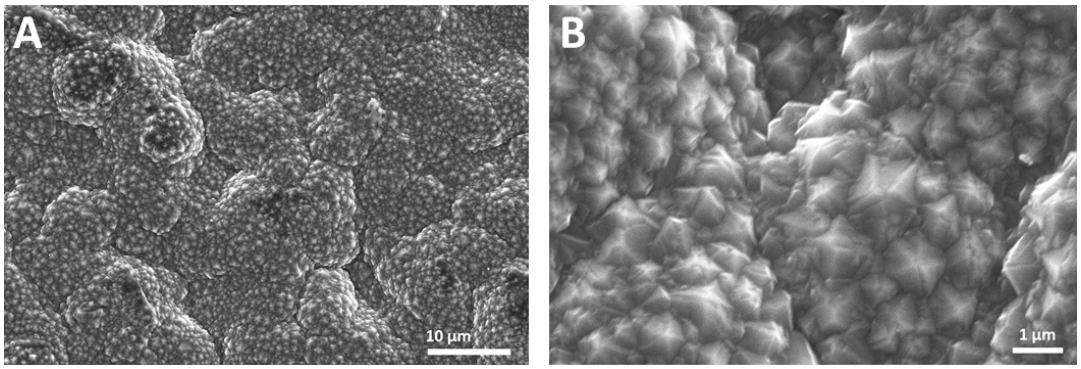

Figure 5.1: SEM micrographs of pristine Neocoat Nb/BDD anode surface at (A) x2000 and (B) x12000 magnification

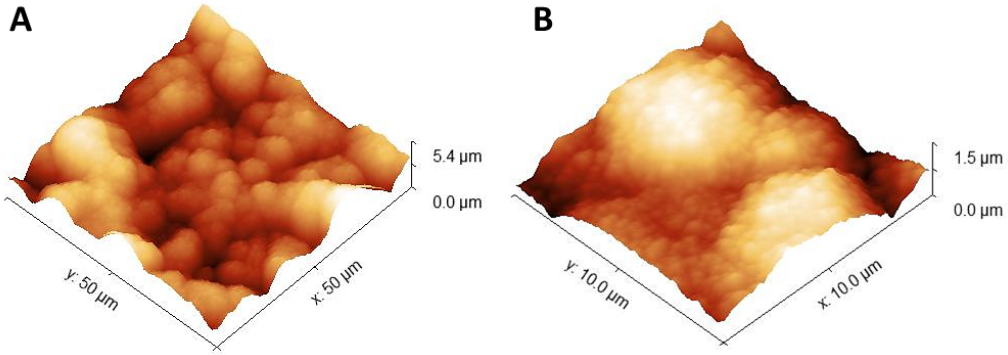

Figure 5.2: AFM topographic images of pristine Neocoat Nb/BDD anode surface: (A) 50 x 50 μm^2 map and (B) 10 x 10 μm^2 map

5.1.3 RAMAN SPECTROSCOPY ANALYSIS

Figure 5.3 shows the Raman spectrum obtained from the Neocoat Nb/BDD surface. At least, five different signals can be distinguished. The origin of the two broad bands located at ca. 491 cm^{-1} and 1239 cm^{-1} remains poorly understood [83] but they are frequently attributed to boron inclusion in the diamond lattice (B-C vibrational modes) and the Fano resonance from lattice impurities due to boron doping [84], respectively. The sharp peak at 1330 cm^{-1} corresponds to the diamond one-phonon line. The height and width of this peak determines the quality of the diamond film. The shoulder peak observed around 1355 cm^{-1} and the peak at 1587 cm^{-1} are the so-called D- and G-bands [85], which originate from sp^2 carbon present in both disordered/defective and crystalline forms of graphite trapped in the grain boundaries. Small average diamond grain size leads to a relatively low sp^3/sp^2 ratio which plays an important role in determining the electrode performance [86] in EAOP.

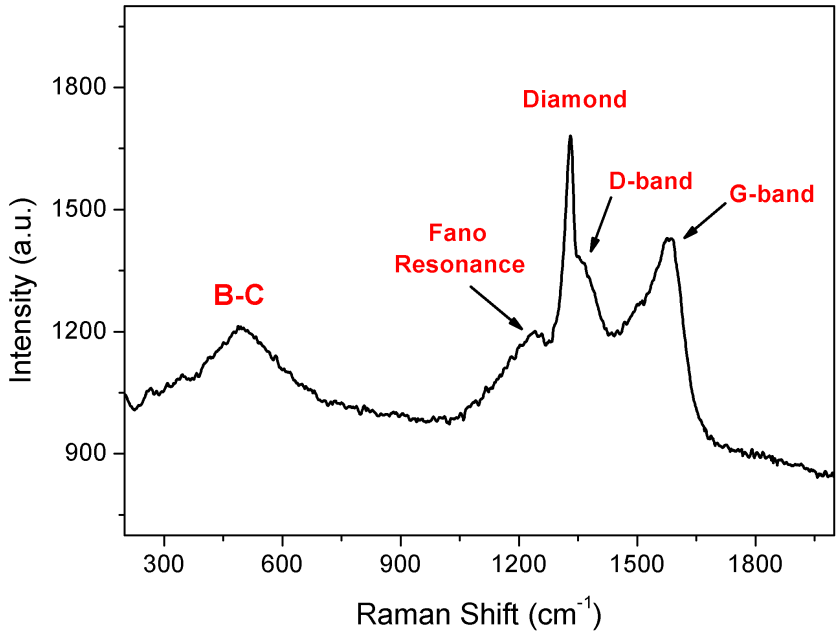

Figure 5.3: Raman spectrum obtained from pristine Neocoat Nb/BDD anode surface

5.1.4 CONTACT ANGLE MEASUREMENTS

A difference in color gradient is visible on the edges of the BDD electrode as shown in Figure 5.4. Since contact angle measurements are highly sensitive, a series of measurements are taken along a line as shown in Fig. 5.5 and the average is calculated as shown in Table 5.1. It is observed that the contact angle at the centre of the Nb/BDD anode is lower than at the edges which is noticed on both sides.

Contact angle measurements are performed to understand the surface termination of the BDD coating. A H-terminated (hydrogen-terminated) surface is hydrophobic and a contact angle between 85° to 95° could mean that the BDD surface is H-terminated. A H-terminated surface is stable and over time it slowly oxidizes, hence turns hydrophilic. A contact angle between 0.6° to 75° could mean that the BDD surface is O-terminated (oxygen-terminated) [86].

This could possibly mean that the edges are more hydrogenated than the centre. From this, a possible inference can be drawn which can explain how the BDD is coated in the HFCVD reactor. Since the BDD is coated on both sides, after coating on one side, the sample is turned upside down. During the second side coating, there are chances that the hydrogen gas reaches the edges of the electrode and hydrogenates the edges more than the centre. Hence, the contact angles measured on the edges of one side is higher than that of the other side.

X-ray photoelectron spectroscopy (XPS) can give a precise information on the surface functionalization. Due to the limitation of sample size, XPS measurements cannot be performed to confirm this observation. An XPS spectrum (Appendix B) is obtained from a reference sample (1 x 2 cm^2) provided by Neocoat, but the morphology was later found to be different from the main Nb/BDD samples. Hence, this XPS data cannot be directly related to the main Nb/BDD anodes.

Figure 5.4: Difference in color gradient of the Neocoat Nb/BDD electrode along the edges (note the lighter grey contrast as compared to the centre)

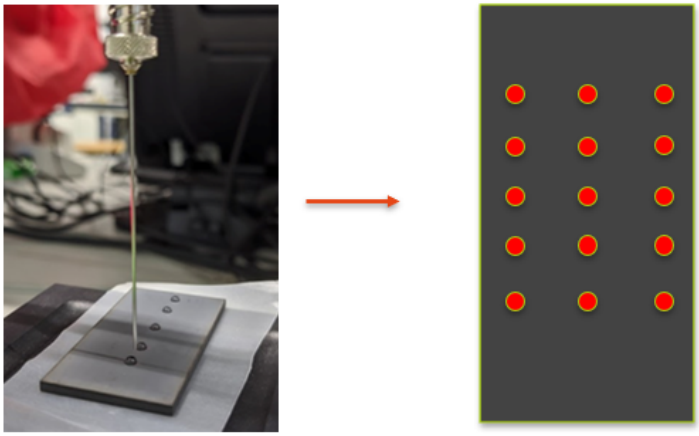

Figure 5.5: Methodology for contact angle measurements on pristine Neocoat Nb/BDD anode surface

Table 5.1: Contact angle measurements taken at the edges and centre of Neocoat Nb/BDD anode on both sides

Water Contact Angles (in degrees)					
Side 1 Left	**Side 1 Centre**	**Side 1 Right**	**Side 2 Left**	**Side 2 Centre**	**Side 2 Right**
92.7	80.8	97.6	81.0	62.8	76.2
84.2	74.3	99.0	71.8	66.4	76.8
89.3	79.0	99.8	72.0	60.6	77.7
94.8	74.2	97.2	78.3	61.8	76.2
92.0	77.3	100.2	70.6	64.7	76.2
92.2	**77.1**	**98.8**	**73.2**	**67.3**	**76.6**

To confirm the observations related to surface functionalization, an alternative method is to perform the surface free energy (SFE) calculations. Figure 5.6 shows the contact angles measured on the right edge and centre of the Nb/BDD anode using three different solvents. The calculated contact angles are shown in Table 5.2.

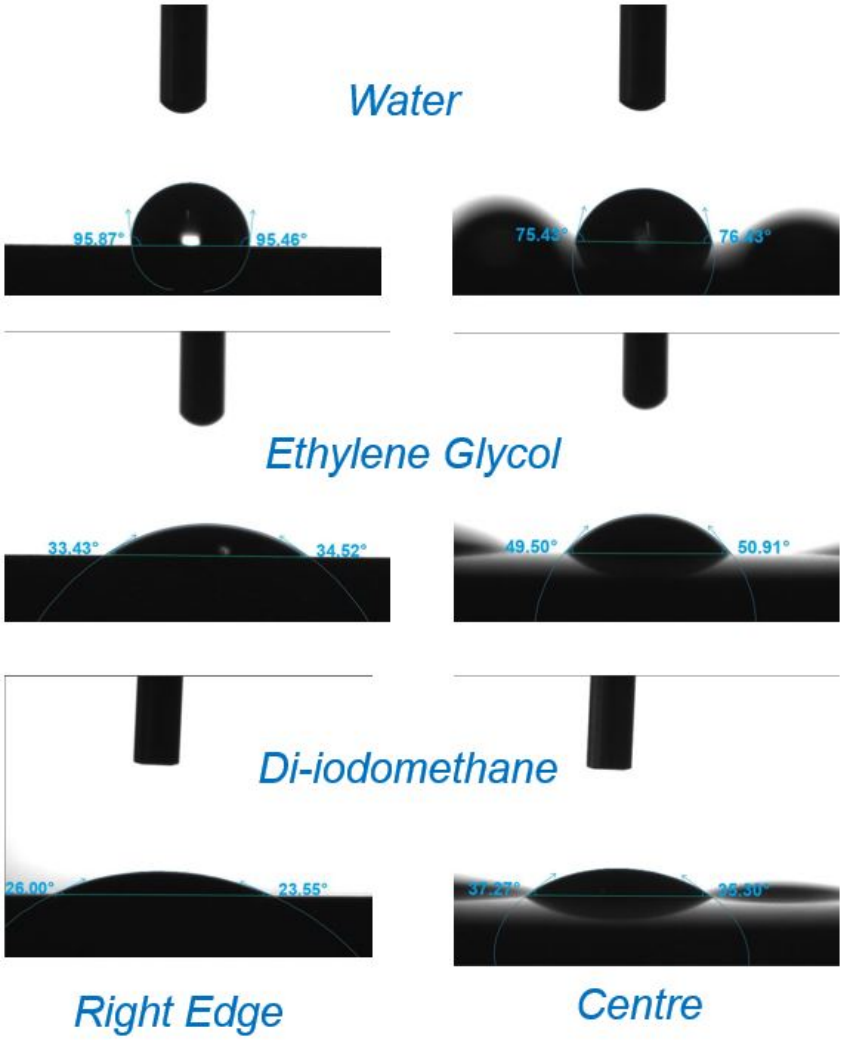

Figure 5.6: Contact angle measured on the right edge (left column) and centre (right column) of the Neocoat Nb/BDD using three different solvents

Table 5.2: Contact angles (in degrees) obtained from measurements on right edge and centre of the Neocoat Nb/BDD anode

Solvent	Right Edge	Centre
Water	95.6	75.9
Ethylene Glycol	33.9	50.2
Di-iodomethane	24.7	36.3

The contact angles are directly inputted into the SFE calculation tab of the OneAttension software. The total, dispersion and polar components of the SFE calculated using Fowkes equation ($\gamma_{total} = \gamma^d + \gamma^p$) are listed in Table 5.3.

Table 5.3: SFE components calculated using Fowkes equation

SFE Component	Right Edge	Centre
Fowkes γ_{total} (in mN/m)	49.45	43
Fowkes γ^d (in mN/m)	49.3	39.2
Fowkes γ^p (in mN/m)	0.15	3.8

From Tables 5.2 and 5.3, it can be observed that with decrease in the contact angle (wetting angle) measured using D.I. water, the polar component of the SFE (γ^p) calculated using Fowkes equation increases. The same observation is reported in a previous study [87] in which the contact angles and SFE on a diamond film were measured and the corresponding changes during hydrogenation and oxidation were reported as shown in Figure 5.7. This additionally supports to the inference that the edges of the Neocoat Nb/BDD anode are more hydrogenated than the centre.

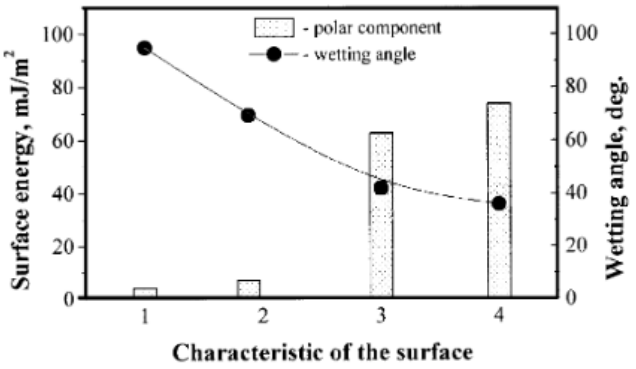

Figure 5.7: Supporting information for SFE measurement [87]. 1 and 2 correspond to the growth and nucleation surfaces of the polycrystalline diamond film hydrogenated with hydrogen plasma, respectively. 3 and 4 correspond to the growth and nucleation surfaces of the polycrystalline diamond film oxidized by heating in air (oxygen) at 500°C, respectively.

5.1.5 POTENTIAL WINDOW

Figure 5.8 shows the potential window (2.7 V) of the Neocoat Nb/BDD anode determined by cyclic voltammetry in 0.1 M KNO_3 at a scan rate of 0.1 V/s. The tangent drawn at the oxygen evolution reaction (OER) and oxygen reduction reaction (ORR) are used to determine the potential window. The background current (~3 $\mu A/cm^2$) is measured at 0.1 V during the forward scan. The peak at 1.2 V corresponds to the sp^2 oxidation.

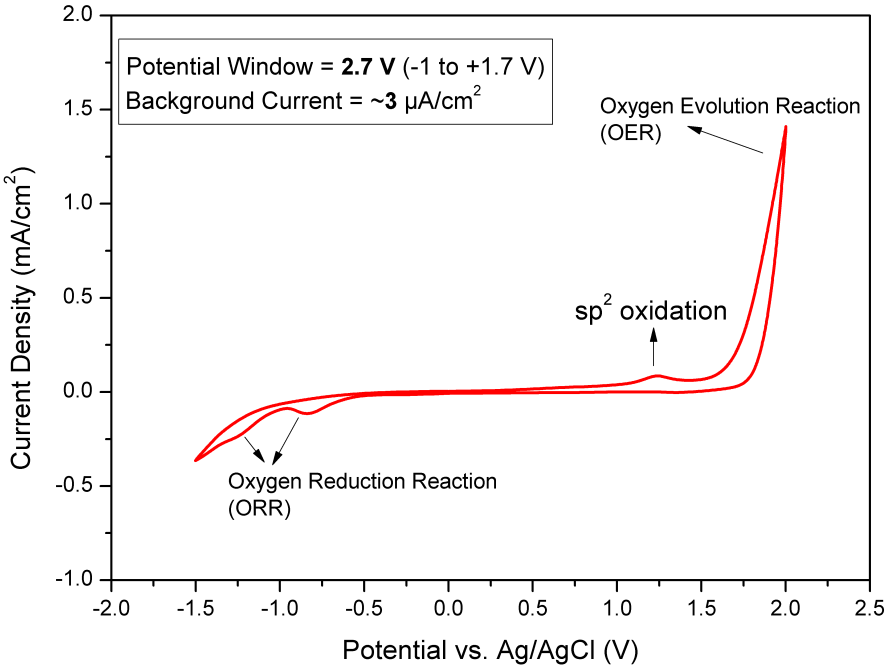

Figure 5.8: Cyclic voltammogram of Neocoat Nb/BDD anode measured in 0.1 M KNO_3 at 0.1 V/s. The curve corresponds to the 10th cycle.

5.2 PART 2: ELECTROCHEMICAL DEGRADATION OF HFPO-DA (GENX) USING BDD ANODES

In this section, the degradation and defluorination efficiency of HFPO-DA (GenX) using boron-doped diamond anodes in EAOP are investigated. This part aims to elucidate the first step in the degradation mechanism of HFPO-DA (GenX) and to clarify the contradictions previously reported on the role of $SO_4^{-\bullet}$. Experiments are performed separately with sodium sulfate and sodium perchlorate to assess the effect of $SO_4^{-\bullet}$. Additionally, the effects of electrolyte concentration, current density, and chloride radicals on the degradation and defluorination efficiency are investigated for the first time to provide in-depth understanding of the degradation. A comparison is made between the degradation efficiency of HFPO-DA and PFOA using BDD-based EAOP to highlight the effect of steric hindrance in the HFPO-DA molecule. To further provide experimental insight into the degradation pathway, the intermediate products are determined using mass spectrometry and the possible reaction mechanism is proposed and compared with that of PFOA. Initially, to get used to the degradation experiments and analytical tools, electrochemical degradation of PFOA is carried out (Appendix C).

5.2.1 ROLE OF SULFATE RADICALS

To probe the role of sulfate radicals, HFPO-DA degradation is performed separately in Na_2SO_4 and $NaClO_4$ electrolyte since $NaClO_4$ is considered inert during anodic oxidation. The degradation is conducted in $NaClO_4$ electrolyte with the same ionic conductivity (2.34 mS/cm @ 22°C) as 0.01 M Na_2SO_4. Figure 5.9(A) shows the effect of electrolyte type on the degradation of HFPO-DA. It is observed that the degradation rate is almost similar in both electrolytes reaching a degradation of 91% (Na_2SO_4) and 93% ($NaClO_4$) after 4 hours. The reaction follows pseudo-first order kinetics (Fig. 5.9(A) inset) and the apparent rate constants (k_{app}) in Na_2SO_4 and $NaClO_4$ electrolytes are 0.0107 min^{-1} and 0.0112 min^{-1}.

Experiments are also conducted at a higher ionic conductivity (9.77 mS/cm @ 22°C) in both the electrolytes and a similar trend is observed (Fig. 5.10). Again, the degradation rate is virtually identical for both electrolytes but the overall degradation (82% after 4 hours) is lower than at lower ionic conductivity. This can be ascribed to the decrease in voltage with increase in ionic conductivity which directly reduces the electron transfer rate. From the data in Figs. 5.9(A) and 5.10, we can draw a conclusion that sulfate radicals are ineffective in HFPO-DA degradation which supports previous findings using UV/persulfate [77, 78]. This is in contrast with previous findings using EAOP [79] in which sodium chloride and methanol are used to study the effect of sulfate radicals. It has to be noted that the direct oxidation of chloride and methanol (a radical scavenger) at the anode can occur as competing reactions to the direct oxidation of HFPO-DA and hence hinder its degradation.

Figure 5.9(B) shows the effect of electrolyte on the percentage of fluoride recovered during the degradation of HFPO-DA. After 4 hours, a defluorination of 83% and 86% is achieved in Na_2SO_4 and $NaClO_4$ electrolytes, respectively. Since sulfate radicals in the bulk solution can hinder the oxidation of intermediate products formed [79], the defluorination efficiency is comparatively higher in $NaClO_4$ electrolyte.

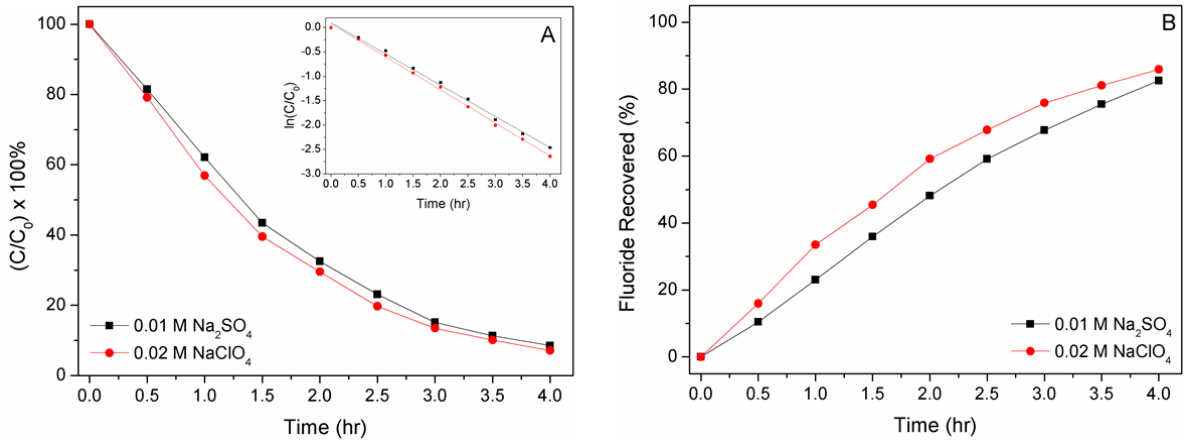

Figure 5.9: Effect of electrolyte on (A) HFPO-DA degradation (inset showing the pseudo-first order kinetic analysis) and (B) defluorination. Current density = 20 mA/cm^2, pH = 7, [HFPO-DA]$_0$ = 15 mg/L, electrolyte: 0.01 M Na_2SO_4 and 0.02 M $NaClO_4$, ionic conductivity = 2.34 mS/cm @ 22°C.

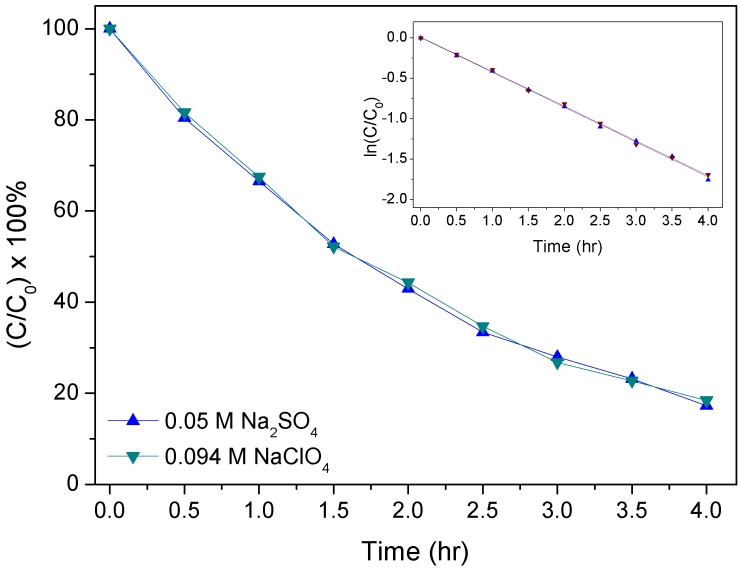

Figure 5.10: Effect of electrolyte on HFPO-DA degradation (inset showing the pseudo-first order kinetic analysis). Current density = 20 mA/cm^2, pH = 7, [HFPO-DA]$_0$ = 15 mg/L, electrolyte: Na_2SO_4 and $NaClO_4$, ionic conductivity = 9.77 mS/cm @ 22°C.

5.2.2 EFFECT OF ELECTROLYTE CONCENTRATION

Experiments in different electrolyte concentrations ranging from 0.005 M to 0.05 M Na_2SO_4 are conducted as shown in Fig. 5.11. The concentrations are chosen to simulate the conductivity range of groundwater [88]. After 4 hours, the degradation of HFPO-DA reaches 96%, 91%, and 79% in corresponding electrolyte concentrations of 0.005 M, 0.01 M, and 0.05 M (Fig. 5.11(A)). Fig. 5.11(B) shows the pseudo-first order kinetics followed. The corresponding kinetic constant (k_{app}) reduces from 0.013 min^{-1} to 0.007 min^{-1} with increasing electrolyte concentration from 0.005 M to 0.05 M. After degradation, it was worth noting that the final pH increases from 7 to 10 with increase in electrolyte concentration which could hinder the degradation. This is due to the competitive reactions between DET of $SO_4^{-\bullet}$ and OH^- at the anode to maintain the balance of electron flow (eqs. 5.1-5.3) and the hydrogen evolution reaction at the cathode that leads to formation of OH^- (eq. 5.4).

$$SO_4^{2-} \rightarrow SO_4^{\bullet -} + e^- \tag{5.1}$$

$$SO_4^{\bullet -} + SO_4^{\bullet -} \rightarrow S_2O_8^{2-} \tag{5.2}$$

$$OH^- \rightarrow OH^{\bullet} + e^- \tag{5.3}$$

$$2H_2O + e^- \rightarrow 2OH^- + H_2 \tag{5.4}$$

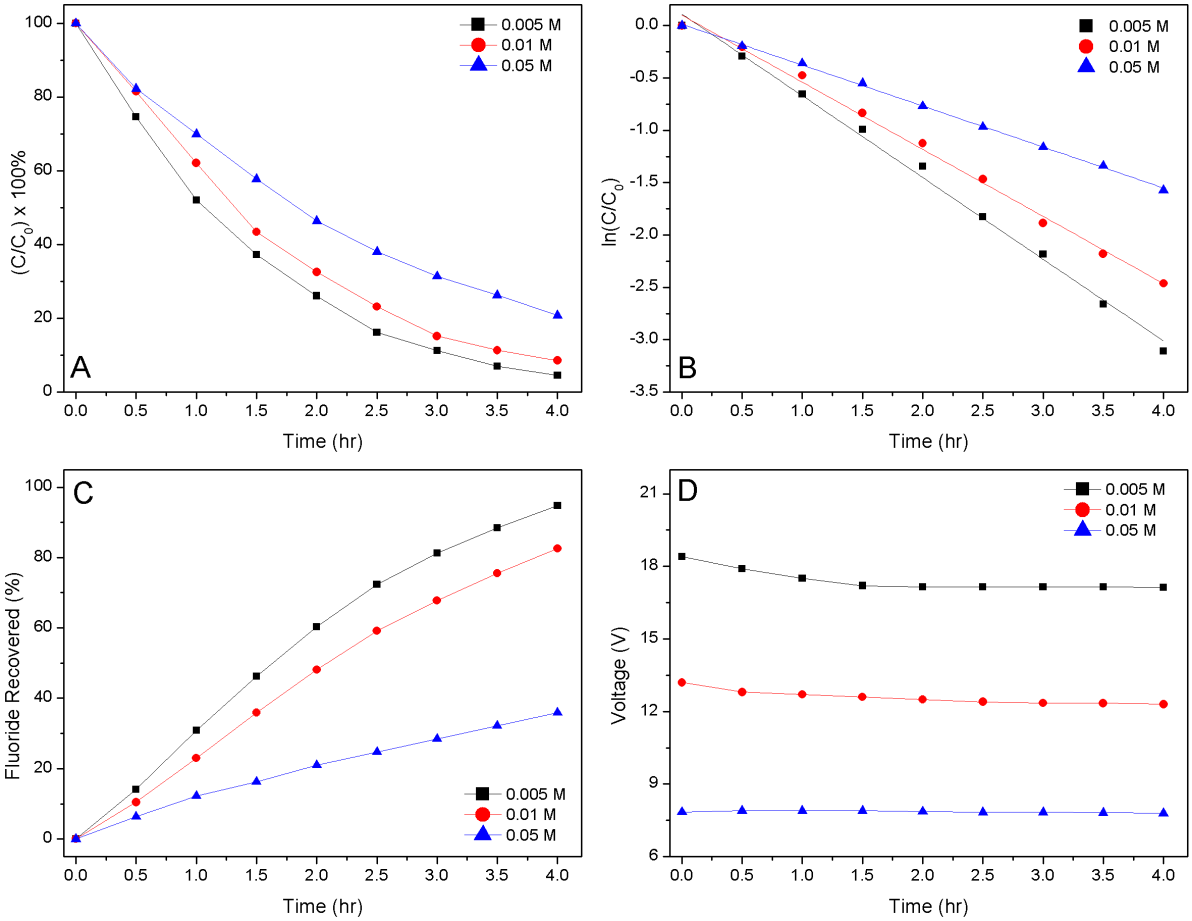

Figure 5.11: Effect of electrolyte concentration on (A) HFPO-DA degradation with (B) corresponding pseudo-first order kinetic analysis, (C) defluorination, and (D) cell voltage. Current density = 20 mA/cm^2, pH = 7, [HFPO-DA]$_0$ = 15 mg/L, electrolyte: Na_2SO_4

Figure 5.11(C) shows the effect of electrolyte concentration on the percentage of fluoride recovered during the degradation. After 4 hours, a defluorination of 95%, 83%, and 36% is achieved in 0.005 M, 0.01 M, and 0.05 M Na_2SO_4 electrolytes, respectively. This supports the above-described fact that sulfate radicals hinder the degradation of intermediates to a great extent through competing reactions. In addition, with increase in electrolyte concentration, the resulting cell voltage reduces which directly reduces the effective electron transfer. The resulting cell voltage at different electrolyte concentrations is shown in Fig. 5.11(D). In 0.005 M and 0.01 M experiments, the voltage decreases by 0.9 V and 0.5 V after 1 hour of degradation due to the additional conductivity of recovered fluoride ions. When the electrolyte concentration is increased from 0.05 M to 0.1 M Na_2SO_4, the resulting cell voltage reduces from 7.8 V to 7.4 V (not shown) which is very small compared to the other voltage differences between electrolyte concentrations in Fig. 5.11(D). The degradation in 0.1 M Na_2SO_4 follows zero order kinetics due to the high electrolyte conductivity which favors electromigration mass transfer (Fig. 5.12). HFPO-DA (pKa = 2.84) [89] dissociates into $C_6F_{11}O_3^-$ and H^+ in water and at high electrolyte conductivity, the reaction follows zero order kinetics.

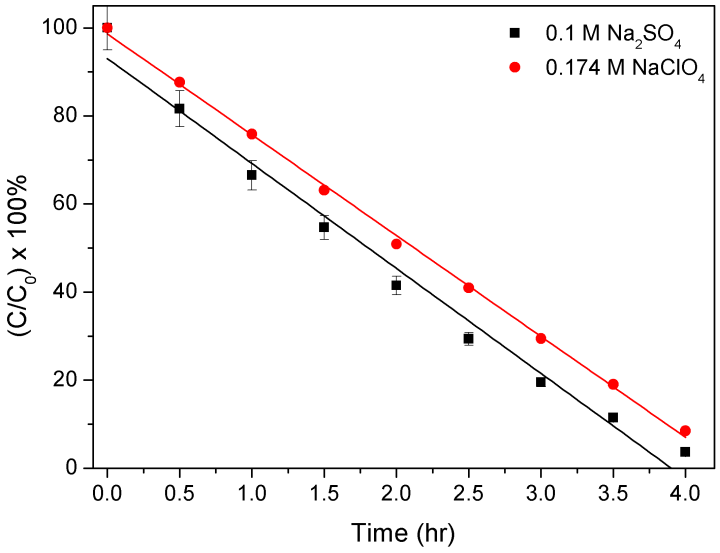

Figure 5.12: Effect of electrolyte concentration on HFPO-DA degradation. Current density = 20 mA/cm^2, pH = 7, [HFPO-DA]$_0$ = 15 mg/L, electrolyte: 0.1 M Na_2SO_4 and 0.174 M $NaClO_4$, ionic conductivity = 17.68 mS/cm @ 22°C.

5.2.3 EFFECT OF CURRENT DENSITY

To study the effect of current density on HFPO-DA degradation, different current densities ranging from 5 mA/cm^2 to 30 mA/cm^2 are applied. Fig. 5.13(A) shows the effect of current density on HFPO-DA degradation. After 4 hours, the degradation reaches 77%, 85%, 91%, and 97% with corresponding current densities of 5, 10, 20, and 30 mA/cm^2. The corresponding kinetic constant follows the order of 0.0059 min^{-1} < 0.0077 min^{-1} < 0.0105 min^{-1} < 0.015 min^{-1} with increasing current density from 5 to 30 mA/cm^2. Fig. 5.13(B) shows the effect of current density on the percentage of fluoride recovered during the degradation. After 4 hours, a defluorination of 63%, 72%, 86%, and 95% is achieved at current densities of 5, 10, 20, and 30 mA/cm^2, respectively. Increasing applied current density leads to increasing electron transfer rate and generation of reactive oxidants (e.g. OH$^\bullet$), thus faster HFPO-DA degradation and defluorination is achieved.

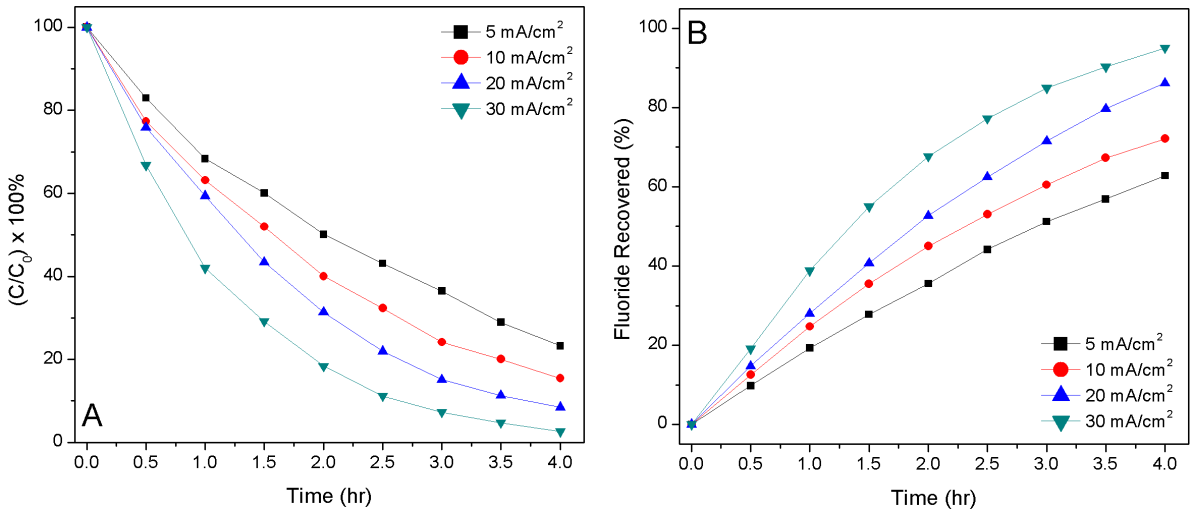

Figure 5.13: Effect of applied current density on (A) HFPO-DA degradation and (B) defluorination. pH = 7, [HFPO-DA]$_0$ = 15 mg/L, electrolyte: 0.01 M Na_2SO_4, ionic conductivity = 2.34 mS/cm @ 22°C.

5.2.4 EFFECT OF CHLORIDE AND REACTIVE CHLORINE SPECIES

To study the effect of chloride and reactive chlorine species on HFPO-DA degradation, experiments are conducted in different concentrations of NaCl ranging from 0 mM to 15 mM. To minimize the effect of voltage reduction due to addition of NaCl, 0.02 M Na_2SO_4 is added as a background electrolyte. Linear sweep voltammetry (LSV) profiles confirm the direct oxidation of Cl^- at the BDD anode (Fig. 5.14). Fig. 5.15(A) shows the effect of chloride on HFPO-DA degradation. After 4 hours, the degradation reaches 74%, 69%, 62%, and 58% in corresponding NaCl concentrations of 0, 2.5, 10, and 15 mM. This shows that Cl^- inhibits HFPO-DA degradation to a considerable extent by occupying active sites on the electrode. Formation of free chlorine is confirmed by use of DPD reagent which is oxidized by free chlorine to give a pink color (Fig. 5.16).

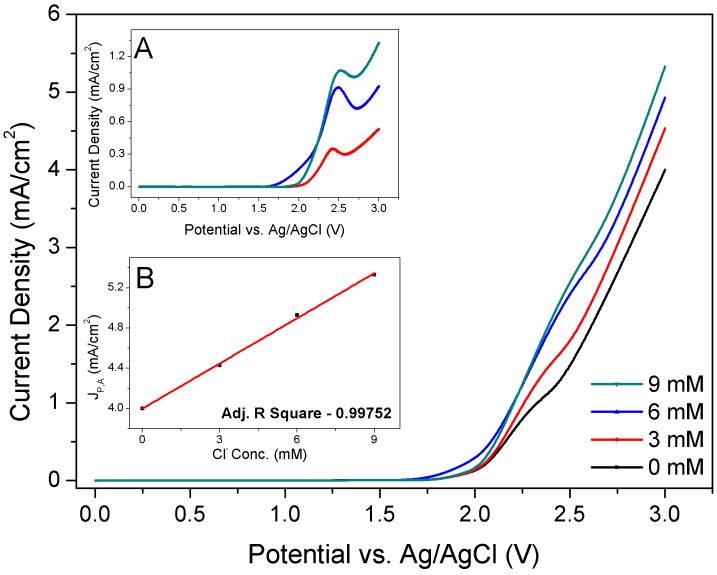

Figure 5.14: Linear sweep voltammetry (LSV) profiles of the BDD anode in a background electrolyte containing 0.02 M Na_2SO_4 and different concentrations of chloride ions (Cl^-). Scan rate – 100 mV/s. Inset A shows the LSV profiles of the three concentrations of Cl^- subtracted from 0 mM Cl^-. It can be observed that the oxidation of Cl^- occurs at 2.5 V vs. Ag/AgCl. Inset B shows a linear relationship between anodic peak current density and Cl^- concentration.

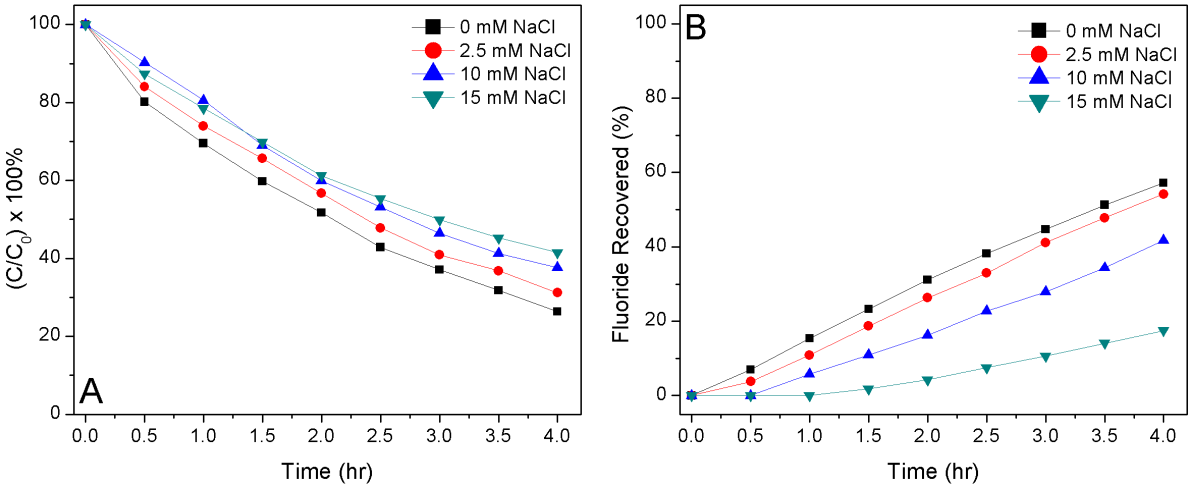

Figure 5.15: Effect of chloride on (A) HFPO-DA degradation and (B) defluorination. Current density = 10 mA/cm^2, pH = 7, $[HFPO\text{-}DA]_0$ = 15 mg/L, background electrolyte: 0.02 M Na_2SO_4

Figure 5.15(B) shows the effect of chloride on the percentage of fluoride recovered during the degradation. After 4 hours, a defluorination of 57%, 54%, 42%, and 17% is achieved in 0 mM, 2.5 mM, 10 mM and 15 mM NaCl electrolytes, respectively. Since oxidation of chloride (E°= 2.5 V) occurs at a lower potential than $OH^\bullet$ generation (E°= 2.8V), $OH^\bullet$ formation is hindered due to competing reactions at the anode and also due to consumption of $OH^\bullet$ by chloride species to form by-products [90]. However, previous work demonstrated that DET of Cl^- and its reaction with $OH^\bullet$ can lead to the formation of reactive chlorine species ($Cl^\bullet$, Cl_2, ClO^-) (eqs. 5.5-5.7) that accelerated the degradation of PFOS [91]. Electrooxidation of Cl^- using BDD anode can also lead to the formation of unwanted by-products by the formation of chlorate and perchlorate (eq. 5.8).

$$Cl^- \rightarrow (Cl_{ads}^\bullet) + e^- \tag{5.5}$$

$$Cl^\bullet + Cl^\bullet \rightarrow Cl_2 \tag{5.6}$$

$$Cl^\bullet + OH^\bullet \rightarrow ClO^- + H^+ \tag{5.7}$$

$$Cl^- \rightarrow ClO^- \rightarrow ClO_2^- \rightarrow ClO_3^- \rightarrow ClO_4^- \tag{5.8}$$

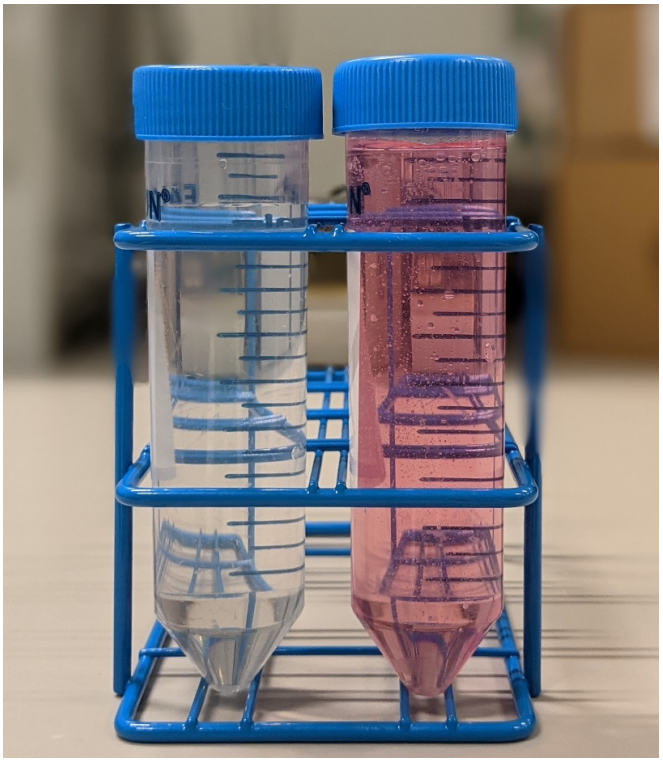

Figure 5.16: DPD method to show the presence of free chlorine. Left conical tube contains DI water with DPD reagent. Right conical tube contains sample collected at the end of degradation in 15 mM NaCl + 0.02 M Na_2SO_4 and DPD reagent. DPD reacts with free chlorine and gives a pink color as seen in the right conical tube.

5.2.5 EFFECT OF RADICAL SCAVENGERS

To show that $OH^\bullet$ plays an important role in the cleaving of C-F bonds, radical scavengers are used in selected experiment. Tert-butyl alcohol (TBA) lacking α-hydrogen is commonly used as $OH^\bullet$ scavenger due to its higher reactivity with $OH^\bullet$ with a reaction rate constant of 3.8-7.6 x 10^8 M^{-1} s^{-1} [92]. A molar concentration of 0.1 M TBA is added to 0.01 M Na_2SO_4 electrolyte containing 15 mg/L HFPO-DA. After 2 hours of degradation, it is observed that no fluoride is recovered and after 4 hours, only 5% of fluoride is recovered. Thus, 0.1

M TBA is sufficient enough to scavenge most of the generated $OH^{\bullet}$. This demonstrates that the reaction of $OH^{\bullet}$ with HFPO-DA to form an unstable alcohol is necessary for complete mineralization of HFPO-DA. Fig. 5.17 shows the effect of TBA addition on the HFPO-DA degradation. It has to be noted that $OH^{\bullet}$ reacts with compounds only through hydrogen abstraction and addition to unsaturated bonds and not through electron transfer mechanism [93]. Since the first step in HFPO-DA degradation is the direct electron transfer (DET), the decrease in degradation efficiency is due to the direct oxidation of TBA competing with DET of HFPO-DA by occupying the active sites on the BDD anode. LSV profiles further confirm the oxidation of TBA at the BDD anode (Fig. 5.18).

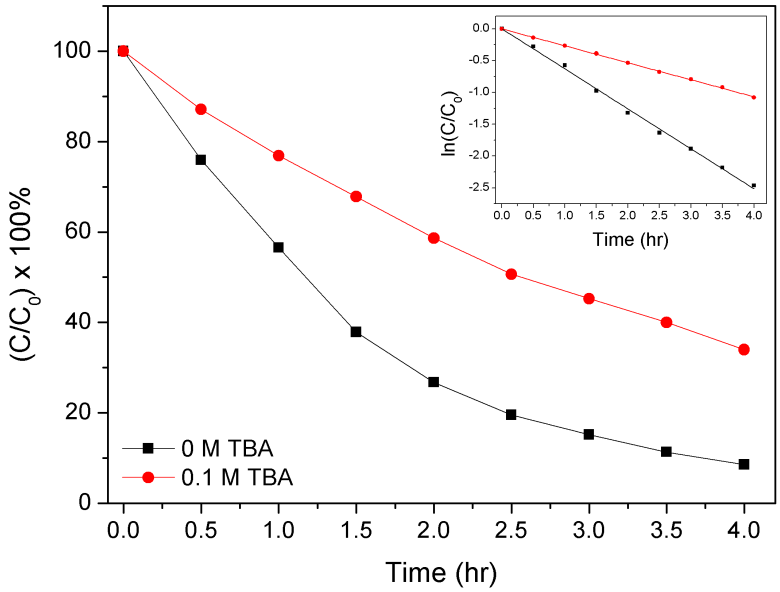

Figure 5.17: Effect of radical scavengers (TBA) on HFPO-DA degradation (inset showing the pseudo-first order kinetic analysis). Current density = 20 mA/cm^2, pH = 6, $[\text{HFPO-DA}]_0$ = 15 mg/L, electrolyte: 0.01 M Na_2SO_4. TBA-tert-butyl alcohol.

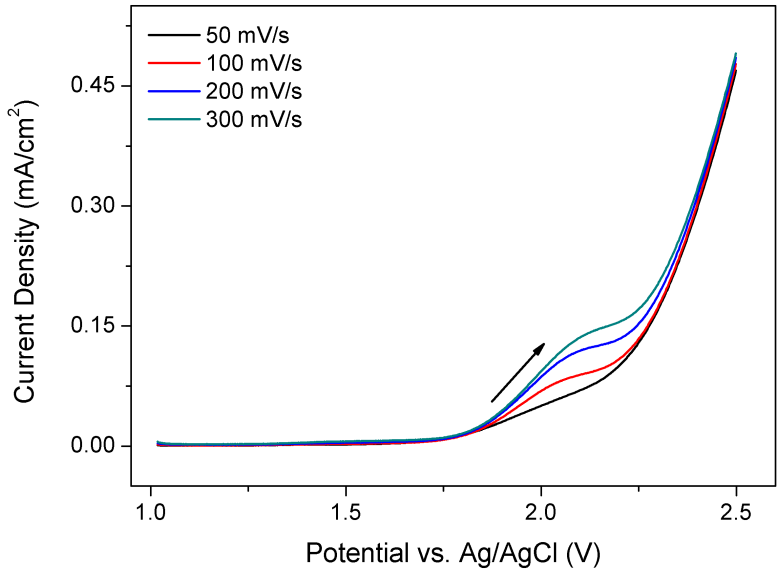

Figure 5.18: Linear sweep voltammetry (LSV) profiles of the BDD anode in 0.1 M tert-butyl alcohol (TBA) at different scan rates. An increasing trend between current density at 2.1 V and scan rate is observed which demonstrates the anode's response due to oxidation of TBA at 2.1 V. Background electrolyte: 0.01 M Na_2SO_4

5.2.6 COMPARISON BETWEEN PFOA AND HFPO-DA DEGRADATION

Fig. 5.19(A) shows the comparison between PFOA and HFPO-DA degradation. After one hour, 57% of PFOA is degraded whereas only 38% of HFPO-DA is degraded. This indicates that the presence of -CF_3 branch at the α-position hinders effective electron transfer from the carboxylic head group. Also, sulfate radicals are observed ineffective due to the same reason, thus introducing complexity in the first step of HFPO-DA degradation. Fig. 5.19(B) shows the fluoride recovered from PFOA and HFPO-DA after 4 hours. It can be observed that in the first hour, more fluoride is generated from PFOA than from HFPO-DA degradation. This is due to the higher efficiency of PFOA degradation as shown in Fig. 5.19(A). After 2 hours, however, the fluoride generated from PFOA degradation is lower than from HFPO-DA. The percentage of fluoride recovered from HFPO-DA after 4 hours is 20% higher than from PFOA. These observations bring us to a conclusion that the direct electron transfer from HFPO-DA to the anode is the rate-determining step in HFPO-DA degradation and that HFPO-DA shows a faster mineralization than PFOA under identical conditions.

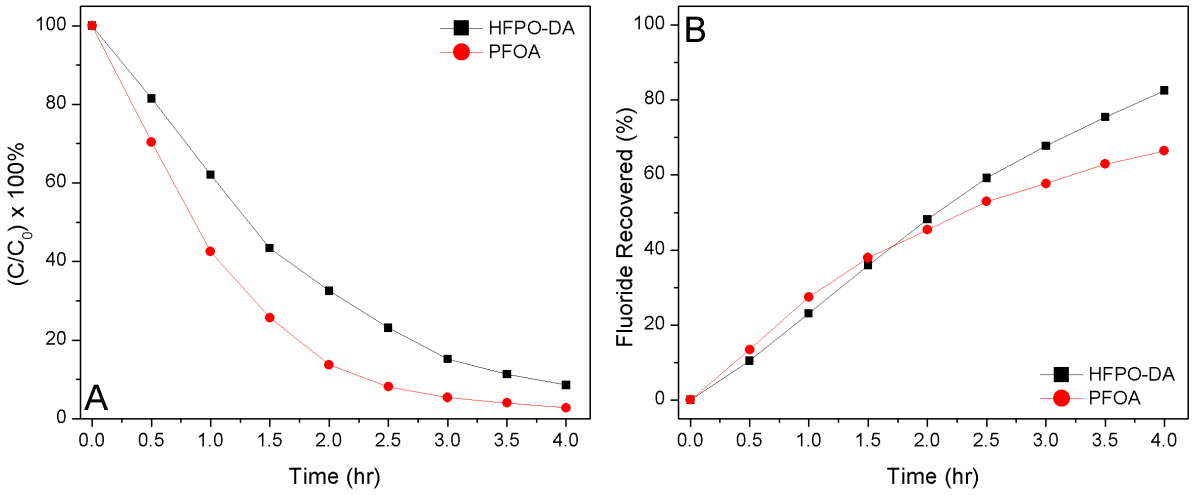

Figure 5.19: Comparison between HFPO-DA and PFOA on (A) degradation and (B) defluorination. Current density = 20 mA/cm^2, pH = 7, $[HFPO\text{-}DA]_0 = [PFOA]_0$ = 45.4 µM, electrolyte: 0.01 M Na_2SO_4.

5.2.7 DEGRADATION MECHANISM OF HFPO-DA

The mechanism of electrochemical degradation of HFPO-DA using BDD anodes is derived using LC-MS analysis. A full scan MS spectrum of a sample collected after 2.5 hours of degradation and the spectrum of an intermediate product, namely pentafluoropropionic acid (PFA, $CF_3CF_2COO^-$) and its corresponding HPLC chromatograph is shown in Appendix D. Density functional theory (DFT) calculations indicate that the carboxylic group is the preferred site for direct electron transfer and the oxidative degradation does not lead to the splitting of ether bond in HFPO-DA [79]. Bao et al. proposed that the oxidative degradation of HFPO-TeA (TeA-tetramer acid) and HFPO-TA (TA-trimer acid) lead to the split of ether bond at the non-ionic end whereas the same is not observed in HFPO-DA with only one ether bond [78].

From the above, we derive the possible oxidative degradation pathway of HFPO-DA as illustrated in Figure 5.20. The first step in HFPO-DA degradation is the direct electron transfer (DET) at the anode surface **(1)** leading to the formation of an alkyl radical via Kolbe decarboxylation **(2)**. The formed radical reacts with $OH^\bullet$ **(3)** to form a thermally unstable alcohol which due to hydrogen abstraction **(4)** undergoes -CF_3 elimination to form acyl fluoride ($C_4F_8O_2$). $C_4F_8O_2$ undergoes hydrolysis **(5)** to form an acid ($C_4F_7O_3^-$) through another F^- elimination. This intermediate again undergoes reaction (1) to (3) to form an unstable alcohol **(6)** which

through HF elimination **(7)** leads to the formation of a shorter acyl fluoride (C_3F_6O). This acyl fluoride undergoes hydrolysis **(8)** to form the second intermediate pentafluoropropionic acid (PFA, $CF_3CF_2COO^-$). The formation of subsequent alkyl radical, alcohol, acyl fluoride and acid is labeled as 4A process [78]. The intermediate PFA through 4A process **(9)** leads to the formation of the third intermediate trifluoroacetic acid (TFA, CF_3COO^-) through -CF_2 unzipping. In the final step, TFA through unzipping **(10)** leads to the formation of F^- and CO_2. Accordingly, HFPO-DA completely mineralizes to F^- and CO_2 through the formation of three intermediates, namely $C_4F_7O_3^-$, PFA and TFA. The formation of PFA and TFA was not reported in the HFPO-DA degradation pathway proposed by Pica et al. [79] using DFT calculations. Hence, the experimental determination of these intermediates gives more insight into the closest feasible HFPO-DA degradation pathway.

In the case of PFOA, which is a linear PFAS isomer, the number of intermediates formed are six as illustrated in Figure 5.21. Hence, the number of intermediates in HFPO-DA is comparatively less which leads to faster mineralization rate, as was observed experimentally (Fig. 5.19(B)).

Implications from Part 2:

The findings from this study demonstrate the complexity in HFPO-DA degradation due to the presence of -CF_3 branch and its resistance to sulfate and chloride radicals. However, electrochemical degradation of HFPO-DA (GenX) using BDD anodes has resulted in the complete mineralization to CO_2 and F^-. This supports electrochemical advanced oxidation processes (EAOPs) using BDD anodes as a promising approach towards sustainable and effective water treatment. EAOPs can be easily implemented in the existing fluoropolymer production plants for the complete mineralization of PFAS and hence, drastically reduce their discharge into the environment.

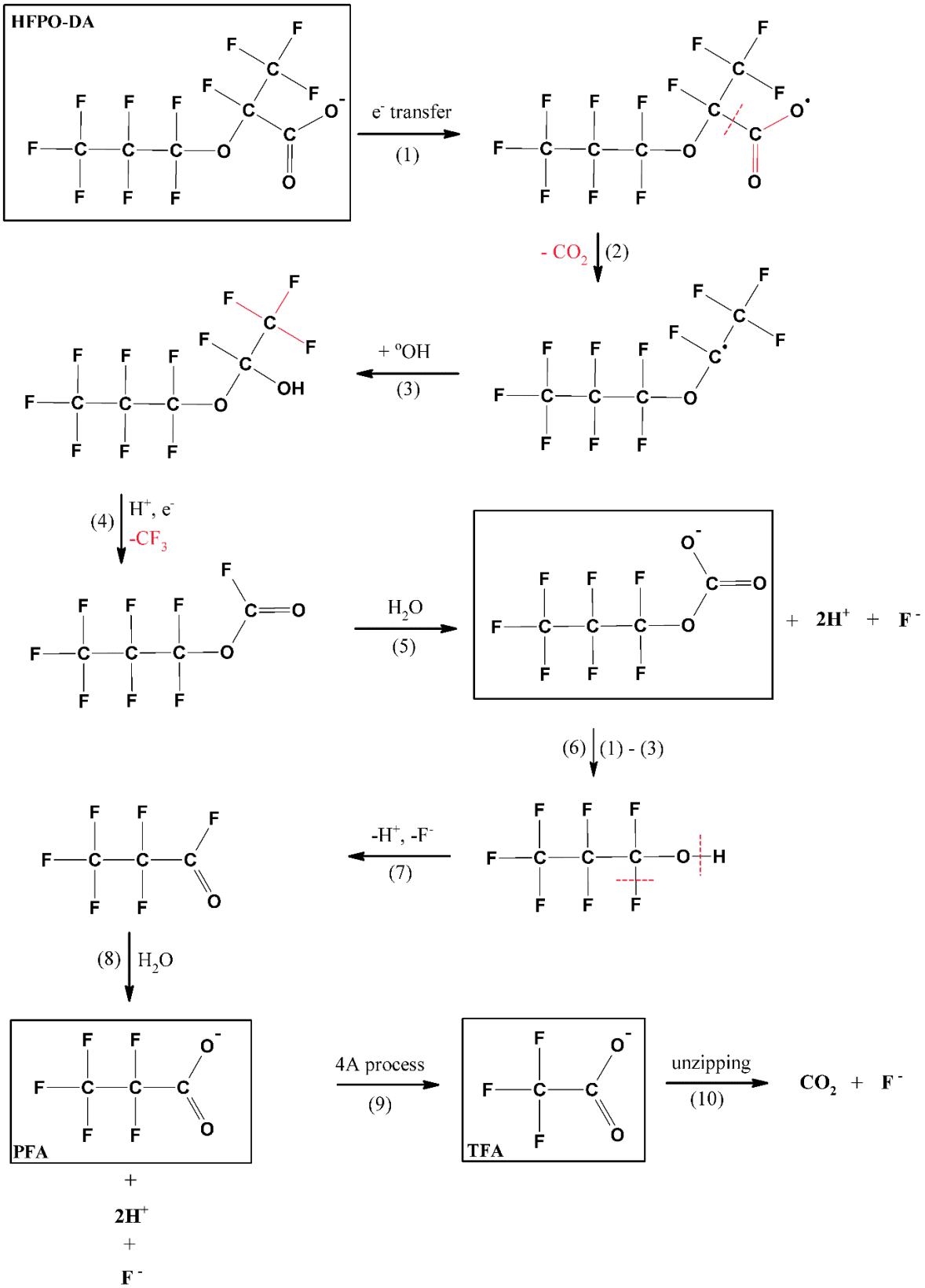

Figure 5.20: Proposed oxidative degradation pathway of HFPO-DA through determination of intermediates using LC-MS analysis. For complete mineralization, HFPO-DA degrades through successive formation of three intermediates to form CO_2 and F^-. PFA – Pentafluoropropionic acid and TFA – Trifluoroacetic acid.

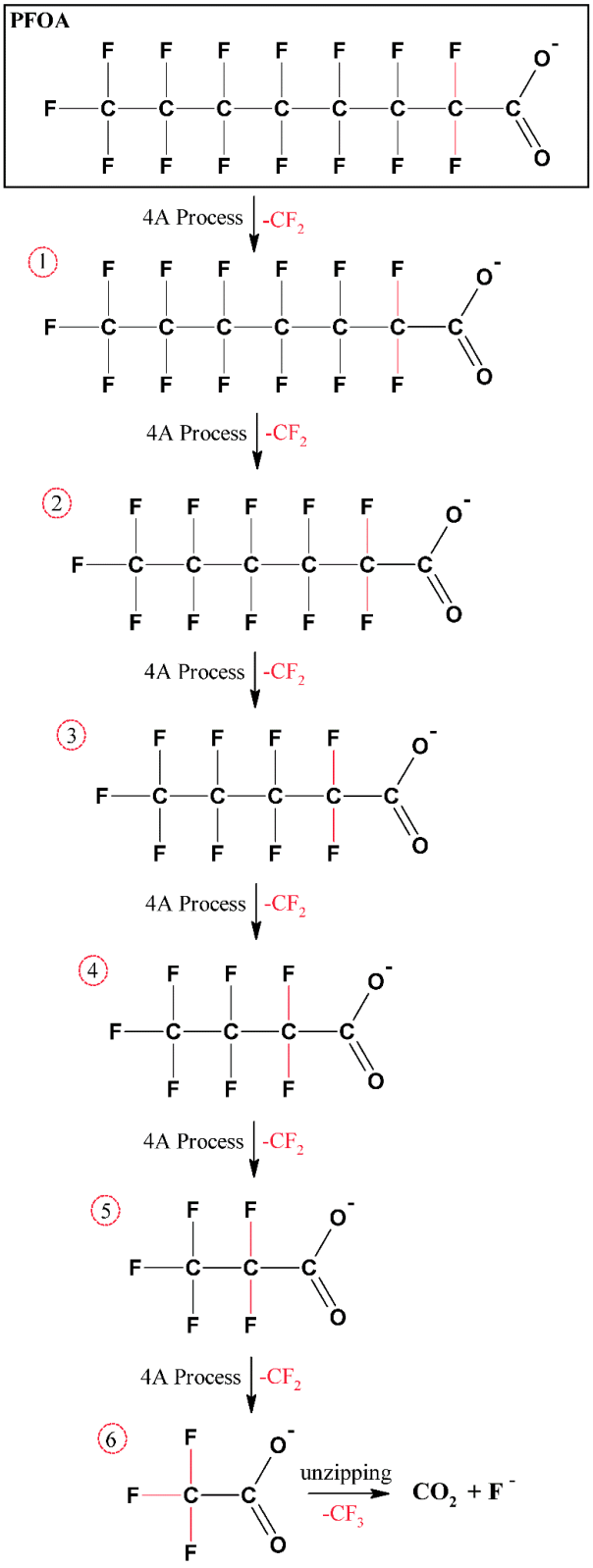

Figure 5.21: Proposed degradation pathway of PFOA in electrochemical oxidation adapted from previous works. For complete mineralization, PFOA degrades through successive formation of six intermediates (1 to 6) to form CO_2 and F^-.

5.3 PART 3: BDD ANODE CHARACTERIZATION AFTER DEGRADATION

This section presents the surface and electrochemical characterization results of the Neocoat Nb/BDD anode after conducting the GenX degradation experiments. For easy interpretation of the differences, the characterization results obtained from pristine Neocoat Nb/BDD anode are also included. The Neocoat Nb/BDD anode has been used for roughly 80 hours after which the characterization is performed.

5.3.1 SEM ANALYSIS

The SEM images in Fig.5.22 illustrate the surface morphology of the Neocoat Nb/BDD anode before and after conducting the degradation experiments. It is observed that the boundaries between clusters are more predominantly visible in Fig. 5.22(B). This is due to the interaction of oxygen, generated during degradation, with the high surface energy carbon groups present at these boundaries between clusters [94]. The longer the degradation, the clearer the boundaries between clusters. The BDD surface shows slightly finer facets after performing the degradation experiments. This might be due to the erosion of sp^2 carbon present in grain boundaries during degradation, which has reduced the contrast in the image. However, there are no surface voids or cracks visible on the BDD surface as shown in Fig. 5.23.

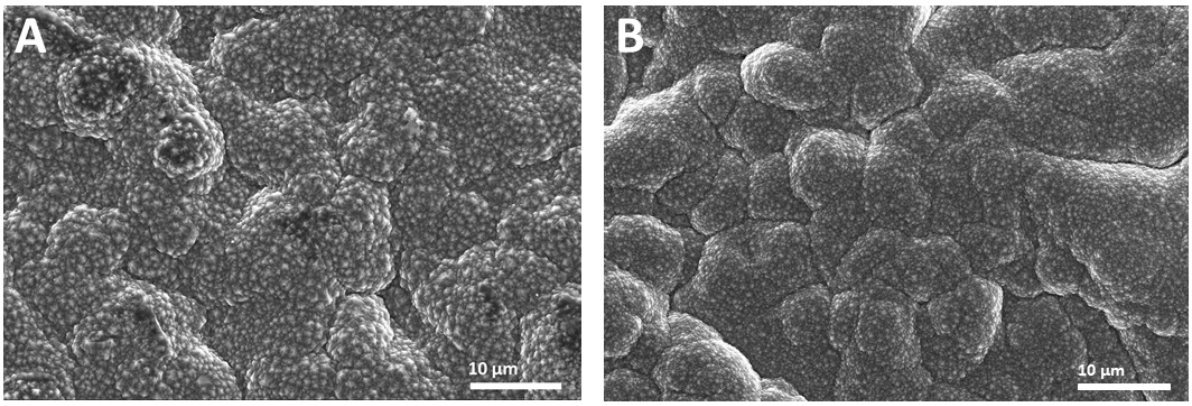

Figure 5.22: SEM micrographs of the Neocoat Nb/BDD anode: (A) before degradation experiments and (B) after degradation experiments

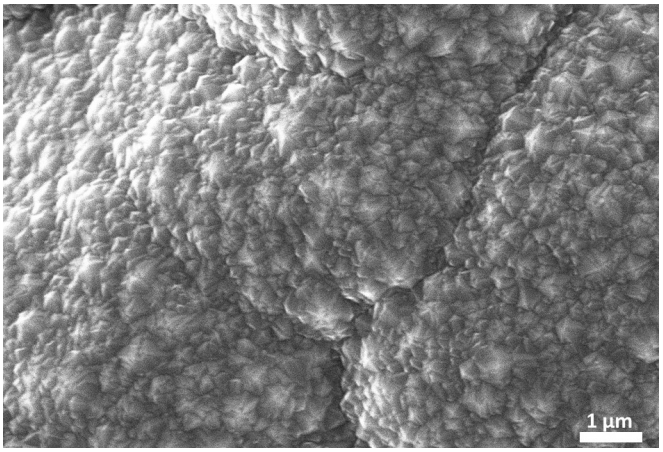

Figure 5.23: SEM micrograph (at a higher magnification) of the Neocoat Nb/BDD anode after conducting the degradation experiments

5.3.2 RAMAN SPECTROSCOPY ANALYSIS

Figure 5.24 shows the Raman spectra obtained from the Neocoat Nb/BDD anode surface before and after conducting the degradation experiments. The spectra cannot be directly compared, since the intensities (Y-axis) depend on the power density of the excitation laser beam and the scattering of the laser from the BDD facets can lead to a reduction in intensity. However, the sp^3/sp^2 ratio can help in determining the difference qualitatively. The sp^3/sp^2 ratio increased from 1.08 (before degradation) to 1.22 (after degradation). This confirms the fact that anodic oxidation leads to the stripping of sp^2 carbon from the grain boundaries and hence, effectively increases the sp^3/sp^2 ratio.

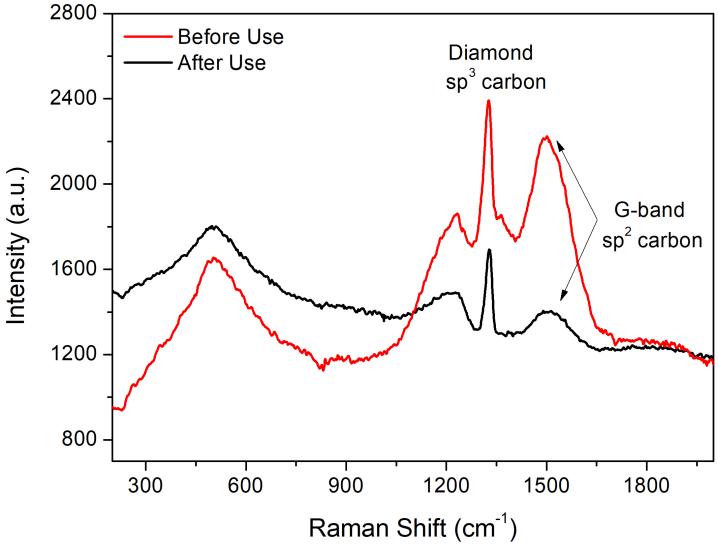

Figure 5.24: Raman spectra obtained from the Neocoat Nb/BDD anode surface before and after conducting the degradation experiments

5.3.3 CONTACT ANGLE MEASUREMENTS

Results of the contact angle measurements taken at the edges and centre of the Neocoat Nb/BDD anode before and after conducting the degradation experiments are shown in Fig. 5.25. As discussed before, anodic oxidation can increase the formation of oxygen-terminated (O-terminated) surface sites [86] and hence, the BDD surface turns more hydrophilic (i.e., lower water contact angles). The increased wettability is noticed on both sides of the Nb/BDD anode at both the centre and the edges.

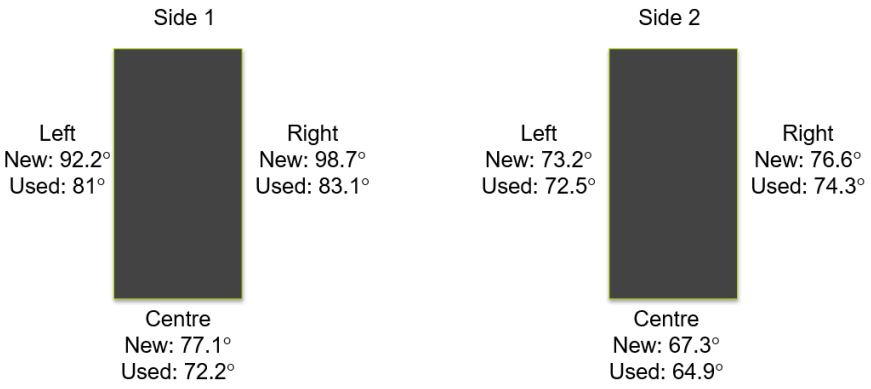

Figure 5.25: Water contact angles measured at the edges and centre of the Neocoat Nb/BDD anode before and after conducting the degradation experiments

5.3.4 POTENTIAL WINDOW

Figure 5.26 shows the potential window of the Neocoat Nb/BDD anode before and after conducting the degradation experiments. The oxygen evolution potential increased from +1.7 V to + 2.2 V. This directly increased the potential window from 2.7 V to 3.2 V. The peak at 1.2 V corresponding to sp^2 oxidation is not visible in the cyclic voltammogram of the Neocoat Nb/BDD anode after performing the degradation experiments which further confirms the stripping of sp^2 regions. Since sp^2 regions can act as active sites for electron transfer (charge transfer mediators), they could favor oxygen evolution reactions [95, 96]. The wider potential window implicates that the oxygen evolution reactions occur at higher potential. The background current is ~0.2 $\mu A/cm^2$ which is lesser compared to the pristine Neocoat Nb/BDD anode (~3 $\mu A/cm^2$).

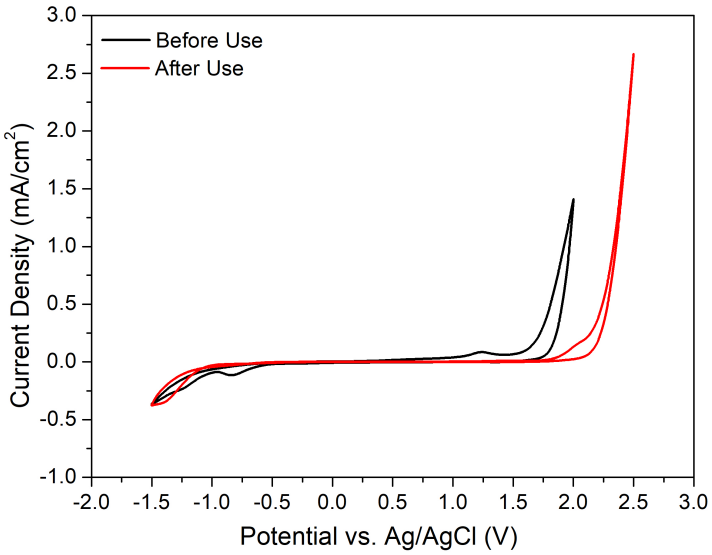

Figure 5.26: Potential window of the Neocoat Nb/BDD anode before and after conducting the degradation experiments. Cyclic voltammograms are measured in 0.1 M KNO_3 at 0.1 V/s. The curves corresponds to the 10th cycle.

5.3.5 OXIDATION OF >CH_2 GROUPS

During the determination of the potential window of the pristine Neocoat Nb/BDD anode, an additional peak near +2.2 V was observed when the positive scan range was extended from +2.0 V to +2.5 V (Fig. 5.27). Previous works [97, 98] reported that this peak is attributed to the oxidation of pristine >CH_2 groups (>CH_2 + H_2O → >C=O + $4H^+$ + $4e^-$) on the BDD surface. However, the peak has disappeared in the cyclic voltammogram of the Neocoat Nb/BDD anode after performing the degradation experiments which indicates that >CH_2 groups have been completely oxidized to >C=O. This supports the observations of increased hydrophilicity of the BDD anode surface made from contact angle measurements.

5.3.6 FERROCYANIDE REDOX REACTION

As mentioned earlier, ferrocyanide redox couple is used to study the heterogeneous electron transfer (HET) processes and it is very sensitive to the electrode surface due to inner-sphere reaction. According to the Randles-Sevcik equation [99], the peak current density is not only a function of the concentration and diffusion of active species but also on the scan rate. With increasing scan rate, the peak current density also increases since faster voltage sweep causes a larger concentration gradient near the electrode surface, resulting in a higher current. This phenomenon can be evidently observed in Fig. 5.28.

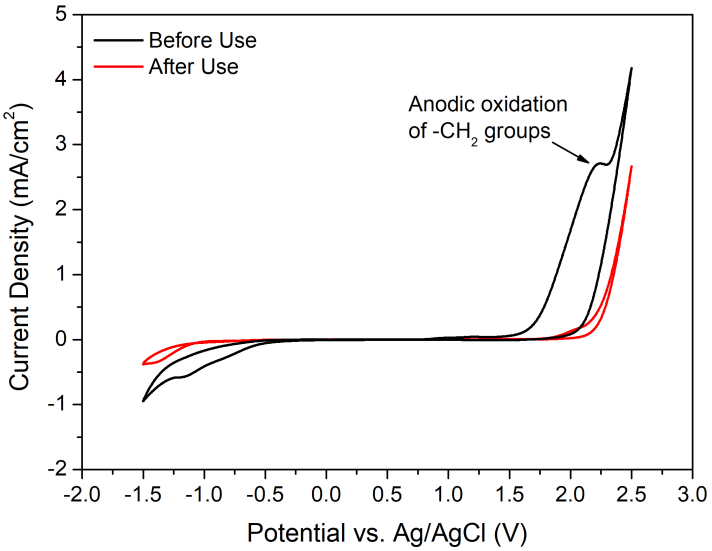

Figure 5.27: Cyclic voltammograms illustrating the disappearance of $>CH_2$ oxidation peak after anodic oxidation

The peak-to-peak separation (i.e., potential difference between oxidation and reduction peak) is used to study the heterogeneous electron transfer kinetics. The peak-to-peak separation (ΔE_p) in cyclic voltammograms of the Neocoat Nb/BDD anode before and after conducting the degradation experiments are 255 mV and 1050 mV, respectively. These values, respectively, correspond to a scan rate of 0.8 V/s as denoted by the arrow marks in Fig. 5.28. It can be inferred that anodic oxidation results in the sluggish HET kinetics. This can be attributed to the reduction in active sites for electron transfer due to the stripping of sp^2 which increases the resistance towards near reversible response for electron transfer.

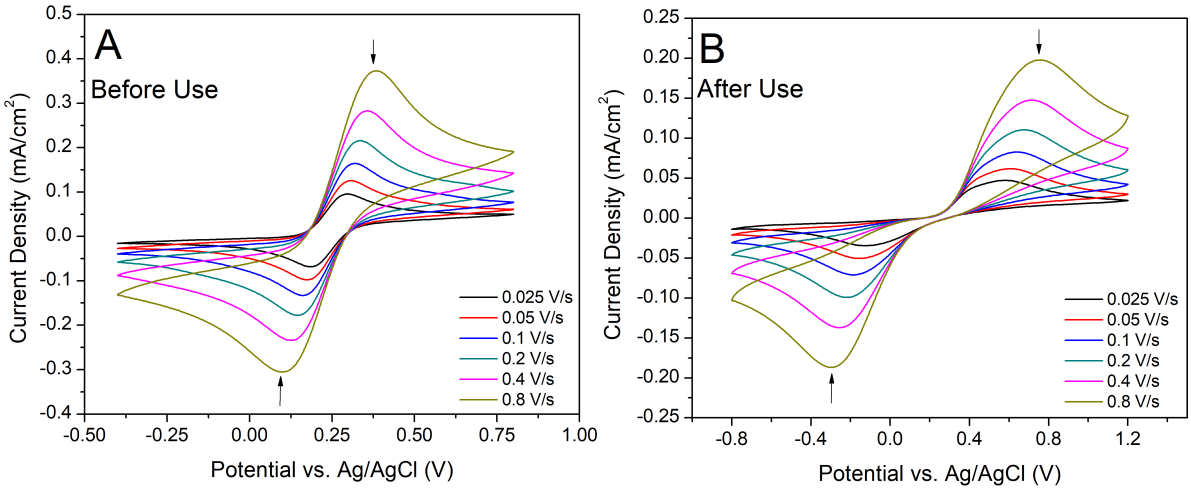

Figure 5.28: Cyclic voltammograms of the Neocoat Nb/BDD anode in 0.1 M KNO_3 containing 1 mM $Fe(CN)_6^{3-/4-}$ at different scan rates. (A) Before conducting degradation experiments and (B) After conducting degradation experiments.

Figure 5.29 shows the relationship between anodic peak current density and the square root of the scan rate. It can be observed that the peak current densities are reduced after conducting the degradation experiments. This is again due to the reduction in active sites at the anode responsible for effective electron transfer. These observations are directly related to the increased overpotential for O_2 evolution after conducting degradation experiments. Hence, anodic oxidation using the Neocoat Nb/BDD anode results in sluggish HET kinetics responsible for O_2 evolution which increases the Faradaic efficiency of $OH^{\bullet}$ production.

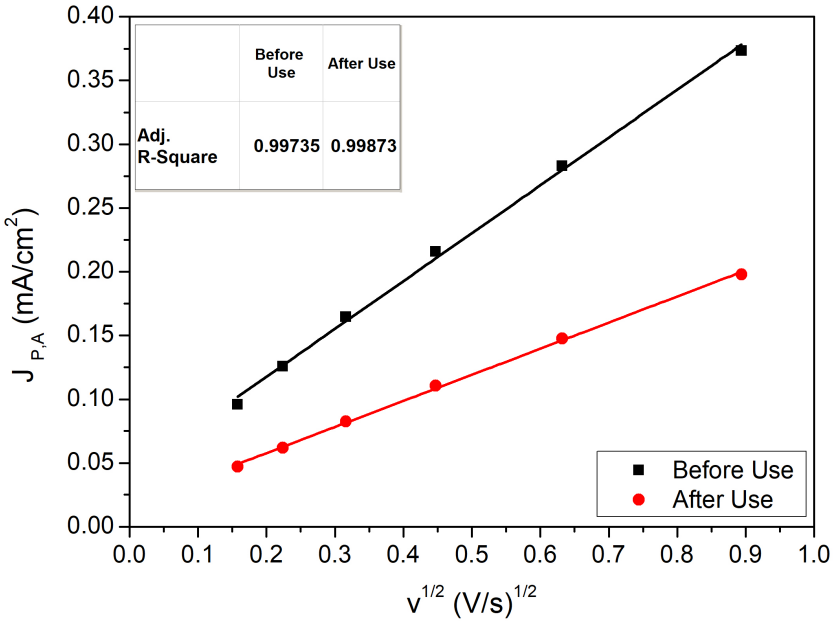

Figure 5.29: Relationship between anodic peak current density and the square root of the scan rate for the Neocoat Nb/BDD anode before and after use in degradation experiments

Summary of Part 3: From all these observations in Part 3, it can be concluded that the stripping of sp^2 carbon has a great effect on the performance of the BDD electrode. It is of great irony that with increased use of the Neocoat Nb/BDD anode for anodic oxidation, the main characteristics like wide potential window and high sp^3/sp^2 ratio are actually enhanced. However, the BDD electrode must be checked for any fouling or surface defects from time to time.

5.4 PART 4: COMPARISON OF DIFFERENT BDD ANODES ON GENX DEGRADATION

Since the properties of BDD are strongly influenced by the surface morphology and growth parameters, a few commercial electrodes, namely as-grown BDD on Nb from Neocoat (CH) and DiaCCon (DE) and polished freestanding BDD from Element Six (UK), are used to compare the GenX degradation and defluorination efficiency. Initially, characterization of these electrodes is performed and following the degradation experiments are conducted. To understand the preferred grain orientation during nucleation and growth of boron-doped diamond in the CVD process, electron backscatter diffraction (EBSD) is performed on the polished freestanding BDD (Appendix E).

5.4.1 SEM ANALYSIS

Fig. 5.30 shows the SEM images of the three BDD anodes.

Neocoat: As mentioned earlier, the BDD surface represents a cauliflower-like morphology which is likely caused by renucleation during the growth process (Fig. 5.30(A)). The average size of BDD surface facets is between 0.5-1 µm.

DiaCCon: The BDD surface represents a highly faceted growth surface with the co-existence of micro- and

nanosized crystalline facets. The average size of BDD surface facets is between 2-10 µm. Also, the slip planes generated from crystal twinning due to dislocation behaviour (stacking faults) is visible in Fig. 5.30(B). The twinning mechanism arises from the formation of a H-terminated carbon atom cluster on a local {111} surface, which also serves as a nucleus for an additional growth layer [100]. Subsequent growth proceeds by reaction at these step edges with one and two carbon atom-containing species.

ElementSix: The polished surface of freestanding BDD is shown in Fig. 5.30(C). The average grain size of the freestanding BDD is between 20-100 µm which is significantly larger compared to the other two BDD anodes.

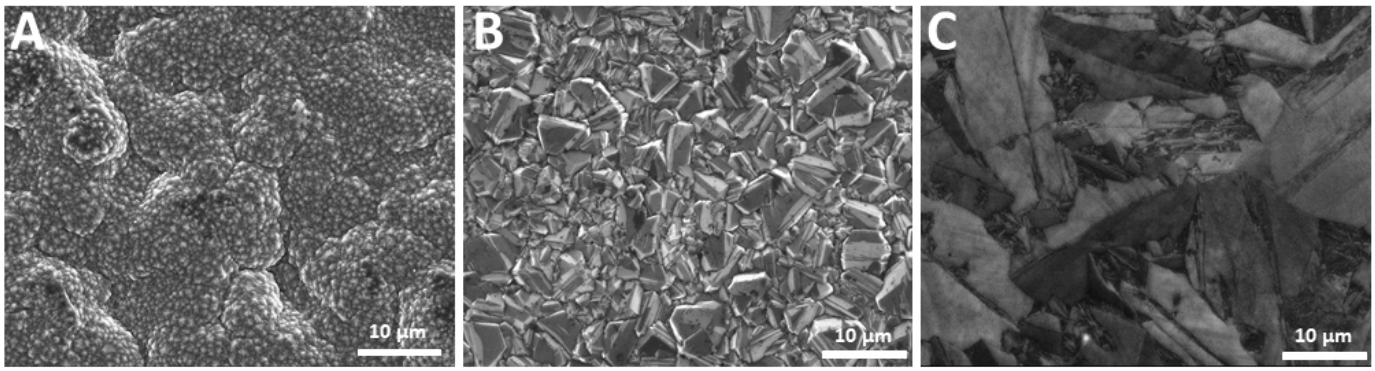

Figure 5.30: SEM micrographs of pristine surfaces of the (A) as-grown BDD on Nb from Neocoat (CH), (B) as-grown BDD on Nb from DiaCCon (DE) and (C) polished freestanding BDD from Element Six (UK)

5.4.2 AFM ANALYSIS

The data obtained from the AFM analysis (Fig. 5.31) of three BDD anodes are shown in Table. 5.4. The root-mean square (RMS) roughness and maximum peak height are of the order Neocoat > DiaCCon > polished freestanding. As mentioned earlier, the surface roughness generated during pre-treatment of the niobium surface has resulted in the relatively high RMS roughness and peak height in the Neocoat Nb/BDD anode.

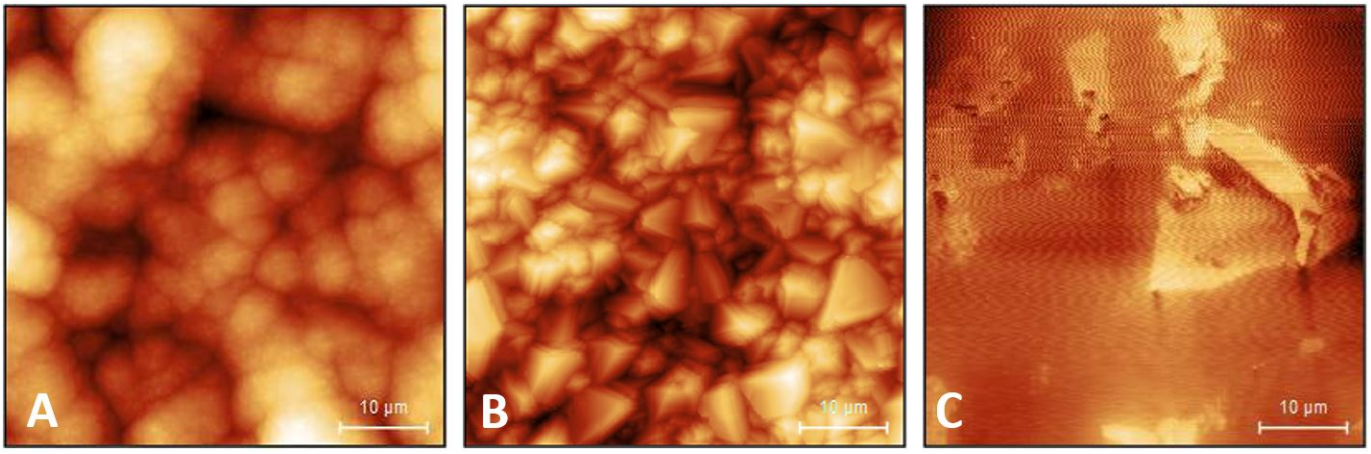

Figure 5.31: AFM topographic images of the pristine surfaces of the (A) as-grown BDD on Nb from Neocoat (CH), (B) as-grown BDD on Nb from DiaCCon (DE) and (C) polished freestanding BDD from Element Six (UK)

Table 5.4: Statistical roughness data obtained from AFM analysis of the three different BDD electrodes

Properties	Neocoat	DiaCCon	ElementSix
RMS roughness (Sq)	860 nm	594 nm	3.9 nm
Mean roughness (Sa)	619 nm	482 nm	2.9 nm
Maximum height (Sz)	5.44 µm	3.51 µm	31.9 nm
Surface area/projected area	1.106	1.141	1

5.4.3 RAMAN SPECTROSCOPY ANALYSIS

Figure 5.32 shows the Raman spectra obtained from the three BDD anodes. It is observed that DiaCCon and ElementSix polished freestanding BDD anodes have a high intensity diamond one-phonon line. Hence, a high sp^3/sp^2 ratio is observed in both DiaCCon and polished freestanding BDD anodes. In Fig. 5.32(C), label 6 (920 cm^{-1}) corresponds to the maxima of the phonon density of states (PDOS-1) due to defects [101] and label 7 (1045 cm^{-1}) corresponds to the maxima of the phonon density of states (PDOS-2) of diamond [102].

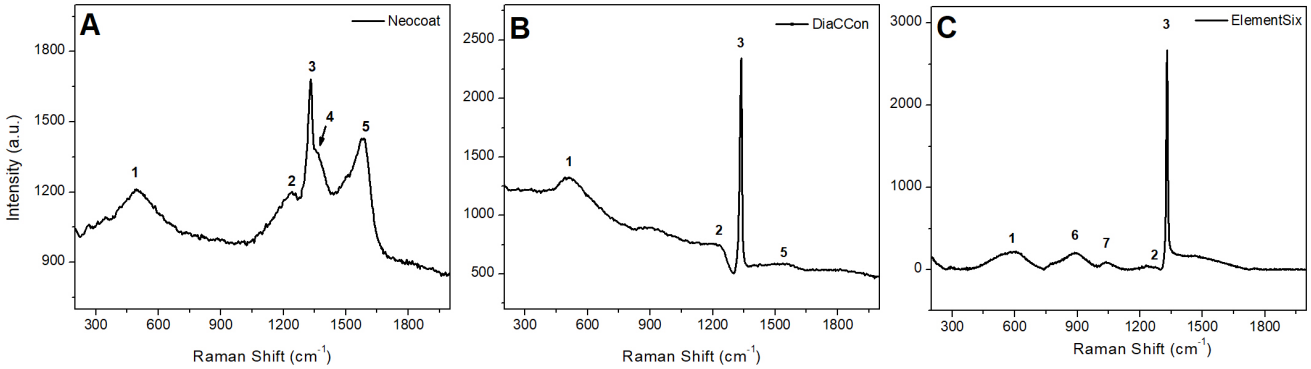

Figure 5.32: Raman spectra obtained from the pristine surfaces of (A) Neocoat, (B) DiaCCon and (C) ElementSix polished freestanding BDD anodes. The Raman signals labeled 1-7 correspond to signals from B-C vibrational modes (1), Fano resonance (2), diamond (3), the D-band (4) and G-band (5) of graphite, PDOS-1 due to defects (6), and PDOS-2 relating to diamond (7), respectively.

5.4.4 COMPARISON OF BDD ANODES ON GENX DEGRADATION

Since the BDD anodes are of different sizes, a different electrochemical cell is used (Fig. 4.4). Each experiment is conducted for 8 hours due to the smaller effective anode surface area (1 cm^2).

Figure 5.33(A) shows the HFPO-DA (GenX) degradation attained using the three BDD anodes. Though the experiments are performed for 8 hours, it resulted in less than 20% degradation due to very limited effective surface area of the BDD anodes. It is observed that the degradation efficiency is higher for the Neocoat BDD anode which can be attributed to the presence of sp^2 acting as active sites for effective electron transfer. Though the ElementSix polished freestanding and DiaCCon BDD anodes have similar sp^3/sp^2 ratio, the GenX degradation was comparatively higher on the ElementSix polished freestanding BDD anode likely due to the observed efficient desorption of bubbles from the anode surface which increases the probability of the HFPO-DA molecule hitting the BDD anode surface. This phenomenon is briefly explained in the next part (Part 5).

Since high sp^3/sp^2 ratio can result in increased overpotential for O_2 evolution and increased Faradaic efficiency for $OH^{\bullet}$ production, the defluorination efficiency is higher on the ElementSix polished freestanding BDD anode as shown in Fig.5.33(B). Again, the defluorination efficiency is likely higher on the ElementSix polished freestanding BDD anode than on the Diaccon BDD anode likely due to desorption of the bubbles from the anode surface. However, a maximum of 10% defluorination is achieved due to very limited effective

surface area of the BDD anodes.

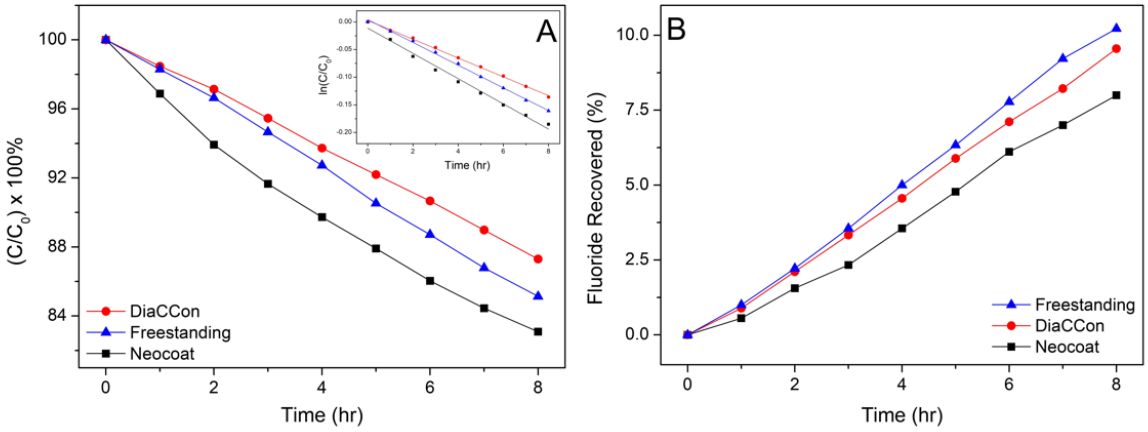

Figure 5.33: Comparison of the different BDD anodes on (a) HFPO-DA degradation (inset showing the pseudo first-order kinetic analysis) and (b) defluorination. Current density = 5 mA/cm^2, pH = 7, [HFPO-DA]$_0$ = 15 mg/L, electrolyte: 0.01 M Na_2SO_4.

Summary of Part 4: A high sp^3/sp^2 ratio of the BDD anode is preferred for degradation of most of the organic and refractory pollutants due to increased Faradaic efficiency for $OH^{\bullet}$ production. However, in the case of PFAS, both sp^2 for effective electron transfer and $OH^{\bullet}$ for cleaving C-F bonds is necessary for complete mineralization to F^- and CO_2. Hence, the sp^3/sp^2 ratio must be optimized for achieving maximum degradation and defluorination efficiency.

5.5 PART 5: STUDY ON THE BUBBLE FORMATION DURING ANODIC OXIDATION

In anodic oxidation, the bubbles generated at the anode surface can obstruct the surface underneath them from exposure to the electrolyte. This directly leads to the decrease in degradation efficiency. To study the effect of bubble formation on the morphology of BDD electrodes, the three aforementioned BDD anodes are used.

During electrochemical degradation of GenX using different BDD electrodes, it was visually observed that the protrusion in the Teflon lid acted as a site for bubble accumulation as indicated with a red circle in Fig. 5.34.

Figure 5.35 shows the schematic illustration of bubble formation on the BDD anode surface. The schematic is based on the side view of the Teflon lid. (A) illustrates the formation of tiny bubbles on the BDD anode surface. (B) Illustrates the growth of the bubbles until they reach a maximum size after which the bubbles drag vertically along the surface and accumulate at the protrusion in the Teflon lid as seen in (C). During this vertical dragging of the bubbles, any tiny bubbles present above are also dragged along. When the bubble accumulated at the protrusion reaches a maximum size (D), it breaks and exposes the obstructed BDD anode surface to the electrolyte again (E).

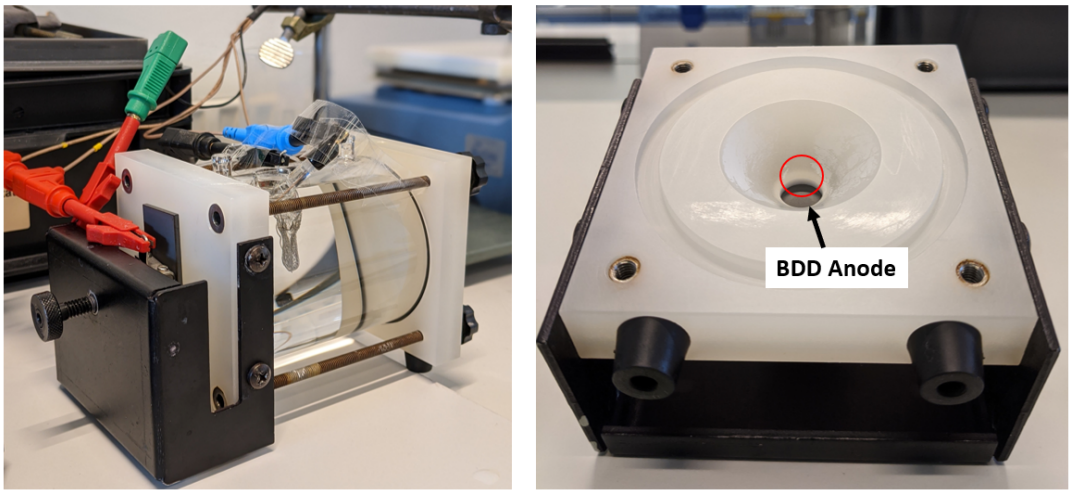

Figure 5.34: Photos of electrochemical setup used for the study of bubble formation (left) and a close-up of the protrusion in the Teflon lid (red circle in the right image) acting as a site for bubble accumulation (right)

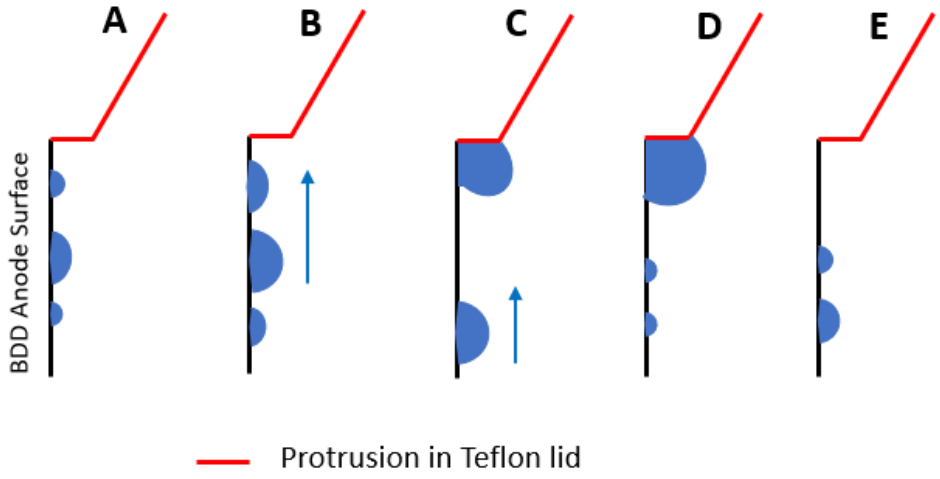

Figure 5.35: Schematic illustration of bubble formation on a BDD anode surface in case of a protrusion in the attached Teflon lid (side view of the teflon lid)

Figure 5.36 shows the current density vs time plot corresponding to the three BDD anodes. The experiments are conducted in 0.01 M Na_2SO_4 for a period of one hour. In order to maintain the same potential, a maximum current is applied through the potentiostat (0.1 A). When the bubble size at the Teflon protrusion increases, the effective anode surface area decreases. This leads to the increase in potential at the anode. Due to the maximum voltage range of the potentiostat (10 V), the applied current decreases to compensate the increase in voltage. For example, in the Neocoat plot, the current density of 18 mA/cm^2 corresponds to the maximum anode surface area and with increase in the bubble size, the current density gradually decreases. At a current density of 13 mA/cm^2, the bubble at the Teflon protrusion reaches its maximum size and immediately breaks. This leads to the sudden jump in current density from 13 mA/cm^2 to 18 mA/cm^2 (starting point of the second curve). Hence, each curve corresponds to the growth of a bubble and the number of lines in the plot directly relates to the number of bubbles formed. The number of bubbles formed on the Neocoat, DiaCCon, and ElementSix freestanding BDD anodes in the time frame of one hour are 16, 15, and 14, respectively. It is visually observed that the bubbles formed at the surface of the ElementSix polished freestanding BDD anode readily detach from the anode surface which leads to a slower bubble growth at the Teflon protrusion.

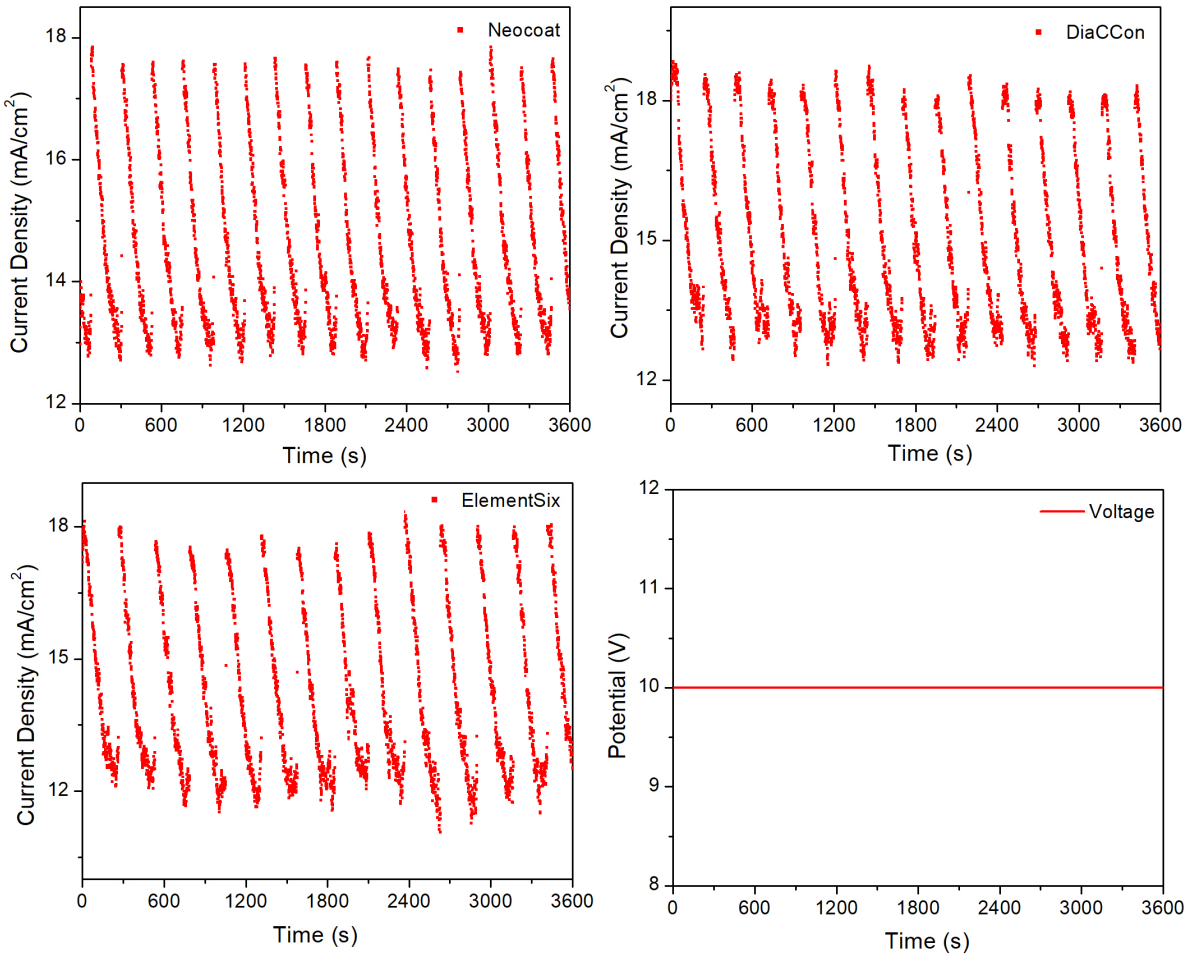

Figure 5.36: Study on the bubble formation using the three different BDD anodes

From these visual and electrochemical observations, it can be concluded that a polished surface leads to effective detachment of the bubbles from the anode surface which directly increases the effective electrode surface area at any point of time. This further explains why the ElementSix polished freestanding BDD anode has higher degradation and defluorination efficiency compared to the rougher DiaCCon BDD anode in the Part 4 study.

6

Conclusions and Recommendations for Future Work

This study examined the electrochemical degradation of HFPO-DA (GenX) using BDD anodes with an experimental insight into degradation influencing parameters. The primary conclusions drawn from this study are summarized as follows.

Phase 1: Electrochemical degradation of GenX using BDD anodes

- HFPO-DA (GenX) completely mineralizes to CO_2 and F^- via formation of three intermediates.
- Direct electron transfer is observed to be the rate-determining step in HFPO-DA degradation using BDD anodes.
- Sulfate radicals are ineffective in HFPO-DA degradation due to the steric hindrance by the -CF_3 branch which blocks the trajectory of $SO_4^{\bullet-}$.
- Increase of sulfate concentration decreases the degradation and defluorination efficiency due to decrease in cell voltage and deceleration in oxidation of intermediate products in presence of $SO_4^{\bullet-}$, respectively.
- Increase of current density increases the degradation and defluorination efficiency due to effective electron transfer and increased $OH^{\bullet}$ production.
- Increase of chloride concentration decreases the degradation and defluorination efficiency due to competing reactions at the BDD anode and quenching of $OH^{\bullet}$ by Cl^-.
- By use of radical scavengers, it is observed that $OH^{\bullet}$ is crucial for complete mineralization.
- By comparing degradation of HFPO-DA with that of PFOA, it is observed that the presence of the CF_3 branch increases the complexity of electron transfer in HFPO-DA degradation even though the mineralization rate is faster for HFPO-DA than for PFOA due to lesser number of intermediates.
- Anodic oxidation using the Nb/BDD anode leads to the stripping of sp^2 carbon from its surface which increases the overpotential for oxygen evolution and increases the Faradaic efficiency for $OH^{\bullet}$ production.

Phase 2: Comparison of different BDD anodes on GenX degradation

- GenX degradation efficiency is higher on the Neocoat Nb/BDD anode due to the presence of sp^2 carbon which acts as active sites for effective electron transfer.
- The defluorination efficiency is higher on the freestanding BDD anode due to increase in Faradaic efficiency for $OH^{\bullet}$ production due to the higher sp^3/sp^2 ratio.

Phase 3: Study on the bubble formation during anodic oxidation

- From electrochemical and visual observations, the polished freestanding BDD anode performs better due to instant detachment of bubbles from the anode surface. This increases the effective anode surface area for electron transfer and $OH^{\bullet}$ production.

Recommendations for future research

- Since the presence of the $-CF_3$ branch increases the complexity in GenX degradation, patterning of the BDD surface with nanopillars can be performed to check whether the enlarged nanoscale topography increases the probability of electron transfer.
- Using the in-house BDD reactor, the growth parameters can be varied to fabricate BDD anodes with varying sp^3/sp^2 ratio and its effect on GenX degradation and defluorination efficiency can be studied.
- Using the oxygen plasma etching tool, micropillars can be created on the BDD anodes to check whether the discontinuity in the BDD surface can suppress the bubble enlargement.
- Since industries and water treatment plants implement electrochemical oxidation treatment method in their pipe flow, degradation experiments using flow cells can lead to better understanding of industrial scale EAOPs using BDD technology for PFAS removal.

BIBLIOGRAPHY

[1] P. W. M. H. Smeets, G. J. Medema, and J. C. van Dijk, *The Dutch secret: how to provide safe drinking water without chlorine in the Netherlands,* Drinking Water Engineering and Science **2**, 1 (2009).

[2] *Water Treatment Schemes - https://ocw.tudelft.nl/course-readings/water-treatment-schemes/,* .

[3] A. I. Stefanakis, D. Zouzias, and A. Marsellos, *Groundwater Pollution: Human and Natural Sources and Risks,* Environmental Sci. and Eng **4**, 82 (2015).

[4] A. H. Vollebergh and J. D. Pbl, *Taxes and fees of regional water authorities in the Netherlands,* , 1 (2014).

[5] The Organisation for Economic Co-operation and Development (OECD), *Series on Risk Management,* Tech. Rep. (2018).

[6] Wikipedia contributors, *Timeline of events related to per- and polyfluoroalkyl substances,* (2021).

[7] 3M, *PFAS History, https://www.3m.com/3M/en_US/pfas-stewardship-us/pfas-history/,* .

[8] ITRC (Interstate Technology & Regulatory Council), *PFAS Technical and Regulatory Guidance Document and Fact Sheets,* (2020).

[9] Wikipedia contributors, *Per- and polyfluoroalkyl substances,* (2021).

[10] R. C. Buck, J. Franklin, U. Berger, J. M. Conder, I. T. Cousins, P. de Voogt, A. A. Jensen, K. Kannan, S. A. Mabury, and S. P. van Leeuwen, *Perfluoroalkyl and polyfluoroalkyl substances in the environment: Terminology, classification, and origins,* Integrated Environmental Assessment and Management **7**, 513 (2011).

[11] Y.-R. Luo, *Handbook of Bond Dissociation Energies in Organic Compounds* (CRC Press, 2002).

[12] WesTech, *Establishing an Effective PFAS Treatment Plan, https://www.westech-inc.com/blog-municipal-water/effective-pfas-treatment-drinking-water,* .

[13] I. Ross, J. Hurst, and J. Miles, *Poly- and perfluoroalkyl substances (PFAS), a new class of emerging contaminants,* Arcadis , 2 (2016).

[14] Rijkswaterstaat, *Action framework for the reuse of PFAS-containing soil and dredged material,* .

[15] Michigan PFAS Action Response Team, *PFAS Sites,* (2019).

[16] A. Nauta, A. Roelandse, and W. J. Knibbe, *Het effect van de industriële lozing van Chemours op de aanwezigheid van PFOA in (oever)grondwater,* (2016).

[17] B. G. H. Bokkers, J. F. M. Versteegh, and P. J. C. M. J. M. J. Zeilmaker, *Risicoinschatting PFOA in drinkwater in het voorzieningsgebied van twee locaties,* , 1 (2016).

[18] Ministerie van Insfrastrutuur en Milieu, *Advies richtwaarde drinkwater voor GenX technologie (FRD902),* , 7994 (2015).

[19] M. Beekman, P. Zweers, A. Muller, W. d. Vries, P. Janssen, and M. Sailmaker, *Evaluation of substances used in the GenX technology by Chemours, Dordrecht,* (2016).

[20] R. Kolpa and A. Nauta, *Het effect van de industriële lozing van Chemours op de aanwezigheid van FRD-903 in oevergrondwater,* (2016).

[21] M. J. Zeilmaker, S. Fragki, E. M. J. Verbruggen, B. G. H. Bokkers, and L. J. P. A, *Mixture exposure to PFAS: A Relative Potency Factor approach,* , 76 (2018).

[22] B. Bokkers, B. van de Ven, P. Janssen, W. Bil, F. van Broekhuizen, M. Zeilmaker, and A. Oomen, *Per- and polyfluoroalkyl substances (PFASs) in food contact materials,* (2019).

[23] A. Muller and E. Smit, *Advies Risicogrenswaarden voor PFOA, PFOS en GenX in zwemwater en vis,* (2020).

[24] M. J. Zeilmaker, C. T. A. Moermond, E. Brandon, P. Hoogerhuis, L. Razenberg, and M. P. M. Janssen, *Persistent organic pollutants in human milk in the Netherlands,* (2020).

[25] W. A. Gebbink, L. van Asseldonk, and S. P. van Leeuwen, *Presence of Emerging Per- and Polyfluoroalkyl Substances (PFASs) in River and Drinking Water near a Fluorochemical Production Plant in the Netherlands,* Environmental Science & Technology **51**, 11057 (2017).

[26] W. A. Gebbink and S. P. van Leeuwen, *Environmental contamination and human exposure to PFASs near a fluorochemical production plant: Review of historic and current PFOA and GenX contamination in the Netherlands,* Environment International **137**, 105583 (2020).

[27] European Environment Agency, *Emerging chemical risks in Europe-PFAS,* (2019).

[28] P. Grandjean, C. A. G. Timmermann, M. Kruse, F. Nielsen, P. J. Vinholt, L. Boding, C. Heilmann, and K. Mølbak, *Severity of COVID-19 at elevated exposure to perfluorinated alkylates,* PLOS ONE **15**, e0244815 (2020).

[29] J. D. McNamara, R. Franco, R. Mimna, and L. Zappa, *Comparison of Activated Carbons for Removal of Perfluorinated Compounds From Drinking Water,* Journal - American Water Works Association **110**, E2 (2018).

[30] C. J. Liu, D. Werner, and C. Bellona, *Removal of per- and polyfluoroalkyl substances (PFASs) from contaminated groundwater using granular activated carbon: a pilot-scale study with breakthrough modeling,* Environmental Science: Water Research & Technology **5**, 1844 (2019).

[31] W. Wang, A. Maimaiti, H. Shi, R. Wu, R. Wang, Z. Li, D. Qi, G. Yu, and S. Deng, *Adsorption behavior and mechanism of emerging perfluoro-2-propoxypropanoic acid (GenX) on activated carbons and resins,* Chemical Engineering Journal **364**, 132 (2019).

[32] S. Woodard, J. Berry, and B. Newman, *Ion exchange resin for PFAS removal and pilot test comparison to GAC,* Remediation Journal **27**, 19 (2017).

[33] Ect2 Montrose Environmental Group, *Treatment of PFAS-Contaminated Water,* .

[34] EPA, *Reducing PFAS in Drinking Water with Treatment Technologies | EPA Science Matters Newsletter | US EPA,* (2018).

[35] K. Jansen, *'Forever chemicals' no more? These technologies aim to destroy PFAS in water,* Chemical & Engineering News **97**, 1 (2019).

[36] O. Coronell, F. Leibfarth, D. Knappe, and H. Stapleton, *Removal of PFAS from drinking water by reverse osmosis membranes , residential filters , and a novel resin NC PFAS Testing (PFAST) Network , a research program funded by the NC Policy Collaboratory PFAST Team 3 Investigators,* (2019).

[37] M. Brienza and I. Katsoyiannis, *Sulfate Radical Technologies as Tertiary Treatment for the Removal of Emerging Contaminants from Wastewater,* Sustainability **9**, 1604 (2017).

[38] S. C. Ameta and R. Ameta, *Advanced Oxidation Processes for Wastewater Treatment 2014,* Emerging Green Chemical Technology (2018).

[39] B. C. Hodges, E. L. Cates, and J. H. Kim, *Challenges and prospects of advanced oxidation water treatment processes using catalytic nanomaterials,* Nature Nanotechnology **13**, 642 (2018).

[40] N. Nicholas, *Benefits And Disadvantages Of The Advanced Oxidation Process,* (2019).

[41] W. Koppenol, *The centennial of the Fenton reaction,* Free Radical Biology and Medicine **15**, 645 (1993).

[42] F. Sopaj, N. Oturan, J. Pinson, F. Podvorica, and M. A. Oturan, *Effect of the anode materials on the efficiency of the electro-Fenton process for the mineralization of the antibiotic sulfamethazine,* Applied Catalysis B: Environmental **199**, 331 (2016).

[43] L. Chu, S. Yan, X.-H. Xing, X. Sun, and B. Jurcik, *Progress and perspectives of sludge ozonation as a powerful pretreatment method for minimization of excess sludge production,* Water Research **43**, 1811 (2009).

[44] G. Boczkaj and A. Fernandes, *Wastewater treatment by means of advanced oxidation processes at basic pH conditions: A review,* Chemical Engineering Journal **320**, 608 (2017).

[45] B. P. Chaplin, *Critical review of electrochemical advanced oxidation processes for water treatment applications,* Environ. Sci.: Processes Impacts **16**, 1182 (2014).

[46] Wikipedia contributors, *Electro-oxidation,* (2021).

[47] Wikipedia contributors, *Electrolysis of water,* (2021).

[48] Wikipedia contributors, *Overpotential,* (2021).

[49] J. Radjenovic and D. L. Sedlak, *Challenges and Opportunities for Electrochemical Processes as Next-Generation Technologies for the Treatment of Contaminated Water,* Environmental Science & Technology **49**, 11292 (2015).

[50] Wikipedia contributors, *Reactive oxygen species,* (2021).

[51] P. V. Nidheesh, G. Divyapriya, N. Oturan, C. Trellu, and M. A. Oturan, *Environmental Applications of Boron-Doped Diamond Electrodes: 1. Applications in Water and Wastewater Treatment,* ChemElectroChem **6**, 2124 (2019).

[52] F. C. Moreira, R. A. Boaventura, E. Brillas, and V. J. Vilar, *Electrochemical advanced oxidation processes: A review on their application to synthetic and real wastewaters,* Applied Catalysis B: Environmental **202**, 217 (2017).

[53] H. Särkkä, A. Bhatnagar, and M. Sillanpää, *Recent developments of electro-oxidation in water treatment — A review,* Journal of Electroanalytical Chemistry **754**, 46 (2015).

[54] K. Muzyka, J. Sun, T. H. Fereja, Y. Lan, W. Zhang, and G. Xu, *Boron-doped diamond: Current progress and challenges in view of electroanalytical applications,* Analytical Methods **11**, 397 (2019).

[55] *Boron Dopen Diamond Electrode, https://www.egr.msu.edu/fraunhofer-ccd/feature/boron-doped-diamond-electrode,* .

[56] S. J. Cobb, Z. J. Ayres, and J. V. Macpherson, *Boron Doped Diamond: A Designer Electrode Material for the Twenty-First Century,* Annual Review of Analytical Chemistry **11**, 463 (2018).

[57] J. M. Freitas, T. d. C. Oliveira, R. A. A. Munoz, and E. M. Richter, *Boron Doped Diamond Electrodes in Flow-Based Systems,* Frontiers in Chemistry **7** (2019), 10.3389/fchem.2019.00190.

[58] T. A. Enache, A.-M. Chiorcea-Paquim, O. Fatibello-Filho, and A. M. Oliveira-Brett, *Hydroxyl radicals electrochemically generated in situ on a boron-doped diamond electrode,* Electrochemistry Communications **11**, 1342 (2009).

[59] C. E. Schaefer, C. Andaya, A. Burant, C. W. Condee, A. Urtiaga, T. J. Strathmann, and C. P. Higgins, *Electrochemical treatment of perfluorooctanoic acid and perfluorooctane sulfonate: Insights into mechanisms and application to groundwater treatment,* Chemical Engineering Journal **317**, 424 (2017).

[60] T. Ochiai, Y. Iizuka, K. Nakata, T. Murakami, D. A. Tryk, A. Fujishima, Y. Koide, and Y. Morito, *Efficient electrochemical decomposition of perfluorocarboxylic acids by the use of a boron-doped diamond electrode,* Diamond and Related Materials **20**, 64 (2011).

[61] A. Urtiaga, C. Fernández-González, S. Gómez-Lavín, and I. Ortiz, *Kinetics of the electrochemical mineralization of perfluorooctanoic acid on ultrananocrystalline boron doped conductive diamond electrodes,* Chemosphere **129**, 20 (2015).

[62] Q. Zhuo, S. Deng, B. Yang, J. Huang, B. Wang, T. Zhang, and G. Yu, *Degradation of perfluorinated compounds on a boron-doped diamond electrode,* Electrochimica Acta **77**, 17 (2012).

[63] S. Barisci and R. Suri, *Electrooxidation of short and long chain perfluorocarboxylic acids using boron doped diamond electrodes,* Chemosphere **243**, 125349 (2020).

[64] B. Gomez-Ruiz, N. Diban, and A. Urtiaga, *Comparison of microcrystalline and ultrananocrystalline boron doped diamond anodes: Influence on perfluorooctanoic acid electrolysis,* Separation and Purification Technology **208**, 169 (2019).

[65] A. L. Garcia-Costa, A. Savall, J. A. Zazo, J. A. Casas, and K. Groenen Serrano, *On the Role of the Cathode for the Electro-Oxidation of Perfluorooctanoic Acid,* Catalysts **10**, 902 (2020).

[66] M. Ensch, C. A. Rusinek, M. F. Becker, and T. Schuelke, *A combined current density technique for the electrochemical oxidation of perfluorooctanoic acid (PFOA) with boron-doped diamond,* Water and Environment Journal , 2 (2020).

[67] B.-T. Zhang, Y. Zhang, Y. Teng, and M. Fan, *Sulfate Radical and Its Application in Decontamination Technologies,* Critical Reviews in Environmental Science and Technology **45**, 1756 (2015).

[68] S. Guerra-Rodríguez, E. Rodríguez, D. Singh, and J. Rodríguez-Chueca, *Assessment of Sulfate Radical-Based Advanced Oxidation Processes for Water and Wastewater Treatment: A Review,* Water **10**, 1828 (2018).

[69] F. Ghanbari and M. Moradi, *Application of peroxymonosulfate and its activation methods for degradation of environmental organic pollutants: Review,* Chemical Engineering Journal **310**, 41 (2017).

[70] F. Liu, G. He, M. Zhao, L. Huang, and M. Qu, *Study on the wastewater disinfection at the boron-doped diamond film electrode,* Procedia Environmental Sciences **12**, 116 (2012).

[71] Wikipedia contributors, *Hypochlorite,* (2021).

[72] A. I. Cederbaum, A. Qureshi, and G. Cohen, *Production of formaldehyde and acetone by hydroxyl-radical generating systems during the metabolism of tertiary butyl alcohol,* Biochemical Pharmacology **32**, 3517 (1983).

[73] X. Li, J. Li, J. Bai, Y. Dong, L. Li, and B. Zhou, *The Inhibition Effect of Tert-Butyl Alcohol on the TiO2 Nano Assays Photoelectrocatalytic Degradation of Different Organics and Its Mechanism,* Nano-Micro Letters **8**, 221 (2016).

[74] H. Bai, P. He, J. Pan, J. Chen, Y. Chen, F. Dong, and H. Li, *Boron-doped diamond electrode: Preparation, characterization and application for electrocatalytic degradation of m-dinitrobenzene,* Journal of Colloid and Interface Science **497**, 422 (2017).

[75] C. E. Alvarez-Pugliese, P. Moreno-Wiedman, F. Machuca-Martínez, and N. Marriaga-Cabrales, *Distillery Wastewater Treated by Electrochemical Oxidation with Boron-Doped Diamond Electrodes,* Journal of Advanced Oxidation Technologies **14** (2011), 10.1515/jaots-2011-0205.

[76] Wikipedia contributors, *Rate-determining step,* (2021).

[77] Y. Bao, S. Deng, X. Jiang, Y. Qu, Y. He, L. Liu, Q. Chai, M. Mumtaz, J. Huang, G. Cagnetta, and G. Yu, *Degradation of PFOA Substitute: GenX (HFPO–DA Ammonium Salt): Oxidation with UV/Persulfate or Reduction with UV/Sulfite?* Environmental Science & Technology , acs.est.8b02172 (2018).

[78] Y. Bao, G. Cagnetta, J. Huang, and G. Yu, *Degradation of hexafluoropropylene oxide oligomer acids as PFOA alternatives in simulated nanofiltration concentrate: Effect of molecular structure,* Chemical Engineering Journal **382**, 122866 (2020).

[79] N. E. Pica, J. Funkhouser, Y. Yin, Z. Zhang, D. M. Ceres, T. Tong, and J. Blotevogel, *Electrochemical Oxidation of Hexafluoropropylene Oxide Dimer Acid (GenX): Mechanistic Insights and Efficient Treatment Train with Nanofiltration,* Environmental Science & Technology **53**, 12602 (2019).

[80] Ossila, *Cyclic Voltammetry: Basic Principles & Set Up,* .

[81] M. Castro, R. Cuerno, M. Nicoli, L. Vázquez, and J. G. Buijnsters, *Universality of cauliflower-like fronts: from nanoscale thin films to macroscopic plants,* New Journal of Physics **14**, 103039 (2012).

[82] J. G. Buijnsters and L. Vázquez, *Growth Dynamics of Nanocrystalline Diamond Thin Films Deposited by Hot Filament Chemical Vapor Deposition: Influence of Low Sticking and Renucleation Processes,* The Journal of Physical Chemistry C **115**, 9681 (2011).

[83] V. Mortet, Z. V. Živcová, A. Taylor, M. Davydová, O. Frank, P. Hubík, J. Lorincik, and M. Aleshin, *Determination of atomic boron concentration in heavily boron-doped diamond by Raman spectroscopy,* Diamond and Related Materials **93**, 54 (2019).

[84] A. F. Sartori, S. Orlando, A. Bellucci, D. M. Trucchi, S. Abrahami, T. Boehme, T. Hantschel, W. Vandervorst, and J. G. Buijnsters, *Laser-Induced Periodic Surface Structures (LIPSS) on Heavily Boron-Doped Diamond for Electrode Applications,* ACS Applied Materials & Interfaces **10**, 43236 (2018).

[85] A. Merlen, J. Buijnsters, and C. Pardanaud, *A Guide to and Review of the Use of Multiwavelength Raman Spectroscopy for Characterizing Defective Aromatic Carbon Solids: from Graphene to Amorphous Carbons,* Coatings **7**, 153 (2017).

[86] J. V. Macpherson, *A practical guide to using boron doped diamond in electrochemical research,* Physical Chemistry Chemical Physics **17**, 2935 (2015).

[87] L. Ostrovskaya, V. Perevertailo, V. Ralchenko, A. Dementjev, and O. Loginova, *Wettability and surface energy of oxidized and hydrogen plasma-treated diamond films,* Diamond and Related Materials **11**, 845 (2002).

[88] G. D. Bathrellos, H. D. Skilodimou, A. Kelepertsis, D. Alexakis, I. Chrisanthaki, and D. Archonti, *Environmental research of groundwater in the urban and suburban areas of Attica region, Greece,* Environmental Geology **56**, 11 (2008).

[89] L. Mullin, D. R. Katz, N. Riddell, R. Plumb, J. A. Burgess, L. W. Yeung, and I. E. Jogsten, *Analysis of hexafluoropropylene oxide-dimer acid (HFPO-DA) by liquid chromatography-mass spectrometry (LC-MS): Review of current approaches and environmental levels,* TrAC Trends in Analytical Chemistry **118**, 828 (2019).

[90] J. M. Barazesh, C. Prasse, and D. L. Sedlak, *Electrochemical Transformation of Trace Organic Contaminants in the Presence of Halide and Carbonate Ions,* Environmental Science & Technology **50**, 10143 (2016).

[91] L. Wang, J. Lu, L. Li, Y. Wang, and Q. Huang, *Effects of chloride on electrochemical degradation of perfluorooctanesulfonate by Magnéli phase Ti4O7 and boron doped diamond anodes,* Water Research **170**, 115254 (2020).

[92] G. V. Buxton, C. L. Greenstock, W. P. Helman, and A. B. Ross, *Critical Review of rate constants for reactions of hydrated electrons, hydrogen atoms and hydroxyl radicals (OH/O in Aqueous Solution,* Journal of Physical and Chemical Reference Data **17**, 513 (1988).

[93] A. Farhat, J. Keller, S. Tait, and J. Radjenovic, *Removal of Persistent Organic Contaminants by Electrochemically Activated Sulfate,* Environmental Science & Technology **49**, 14326 (2015).

[94] X. Kang, Z. Zhang, and L. Gou, *Improvement in electrical conductivity of boron-doped diamond films after hydrogen plasma and vacuum heat treatment,* Applied Surface Science **526**, 146738 (2020).

[95] M. H. Santana, L. A. D. Faria, and J. F. Boodts, *Electrochemical characterisation and oxygen evolution at a heavily boron doped diamond electrode,* Electrochimica Acta **50**, 2017 (2005).

[96] I. Duo, A. Fujishima, and C. Comninellis, *Electron transfer kinetics on composite diamond (sp3)–graphite (sp2) electrodes,* Electrochemistry Communications **5**, 695 (2003).

[97] F. Beck, H. Krohn, W. Kaiser, M. Fryda, C. Klages, and L. Schäfer, *Boron doped diamond/titanium composite electrodes for electrochemical gas generation from aqueous electrolytes,* Electrochimica Acta **44**, 525 (1998).

[98] F. Beck, W. Kaiser, and H. Krohn, *Boron doped diamond (BDD)-layers on titanium substrates as electrodes in applied electrochemistry,* Electrochimica Acta **45**, 4691 (2000).

[99] N. G. Tsierkezos, *Cyclic Voltammetric Studies of Ferrocene in Nonaqueous Solvents in the Temperature Range from 248.15 to 298.15 K,* Journal of Solution Chemistry **36**, 289 (2007).

[100] J. E. Butler and I. Oleynik, *A mechanism for crystal twinning in the growth of diamond by chemical vapour deposition,* Philosophical Transactions of the Royal Society A: Mathematical, Physical and Engineering Sciences **366**, 295 (2008).

[101] V. Blank, V. Denisov, A. Kirichenko, M. Kuznetsov, B. Mavrin, S. Nosukhin, and S. Terentiev, *Raman scattering by defect-induced excitations in boron-doped diamond single crystals,* Diamond and Related Materials **17**, 1840 (2008).

[102] P. Szirmai, T. Pichler, O. A. Williams, S. Mandal, C. Bäuerle, and F. Simon, *A detailed analysis of the Raman spectra in superconducting boron doped nanocrystalline diamond,* physica status solidi (b) **249**, 2656 (2012).

[103] C. Wild, N. Herres, and P. Koidl, *Texture formation in polycrystalline diamond films,* Journal of Applied Physics **68**, 973 (1990).

[104] K. Haenen, A. Lazea, J. Barjon, J. D'Haen, N. Habka, T. Teraji, S. Koizumi, and V. Mortet, *P-doped diamond grown on (110)-textured microcrystalline diamond: growth, characterization and devices,* Journal of Physics: Condensed Matter **21**, 364204 (2009).

[105] D. Liu, C. Chen, D. Perry, G. West, S. J. Cobb, J. V. Macpherson, and P. R. Unwin, *Facet-Resolved Electrochemistry of Polycrystalline Boron-Doped Diamond Electrodes: Microscopic Factors Determining the Solvent Window in Aqueous Potassium Chloride Solutions,* ChemElectroChem **5**, 3028 (2018).

A

SURVEY BY RIVM

A.1 PFAS IN DRINKING WATER

In 2017, RIVM reported that GenX in drinking water at three Dutch drinking water companies has increased, but safe. The levels of GenX measured at different Dutch drinking water companies are shown in Figure A.1 [20].

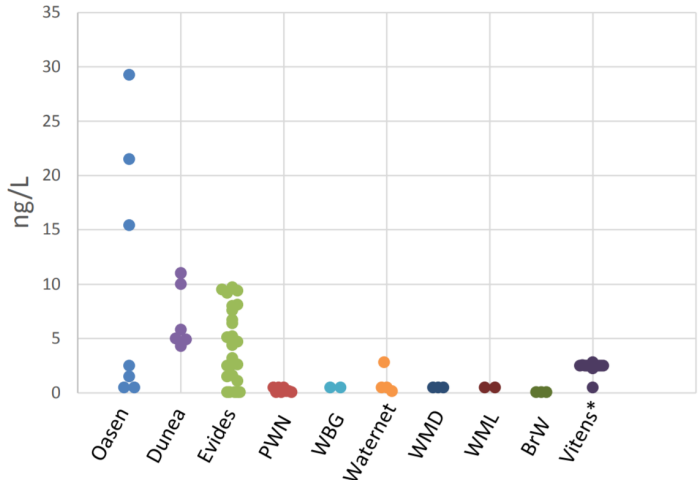

Figure A.1: GenX levels measured at different Dutch drinking water companies [20]

A.2 PFAS IN SOIL

RIVM conducted a survey on the level of PFAS found in soil. The framework for the reuse of PFAS-containing soil was expected to be released by the end of 2020 but still hasn't been published. Construction at various sites have been temporarily suspended until the framework in released. Safe limits for PFAS in soil are listed in Table A.1 [19]. It was observed that Helmond (HM1) reported high levels of PFOA in vegetables and crops grown from the PFAS contaminated soil (Figure A.2) [26].

Table A.1: Safe limits for PFAS in soil [19]

Application requirement (based on other parameters) *	Special features regarding groundwater during application	PFOS (ug / kg)	PFOA (ug / kg)	Other PFAS (per individual substance and incl. GenX) (ug / kg)
Agriculture / nature (<AW200)	Application below groundwater level (2)	0.9	0.8	0.8
	Application within groundwater protection area	0.1	0.1	0.1

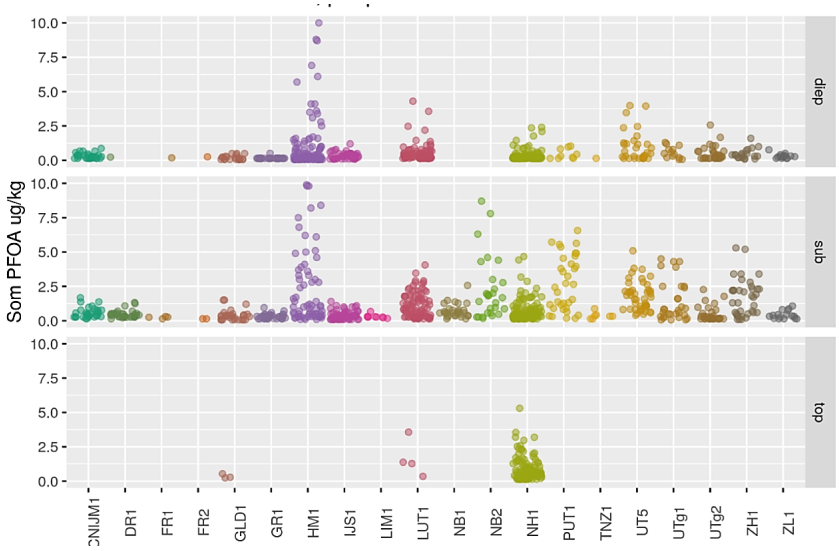

Figure A.2: PFOA levels measured in soil from various locations in The Netherlands [26] Top graph-deep soil, middle graph-sub soil and bottom graph-top soil

A.3 PFAS IN BREAST MILK

World Health Organization (WHO) continuously monitors breast milk samples from Dutch women since 1969. It is reported that PFOS concentration of 45 ng/g milk lipid is measured in breast milk samples collected in the year 2014 (Table A.2). However, the study was delayed and was recently published on March 26, 2020 [24].

Table A.2: PFOS levels measured in breast milk samples from Dutch women in the year 2014 [24]. POP- Persistent organic pollutants, HBGV- Health-based guidance value

POP	Concentration (ng/g milk lipid; for PFOS and PFHxS in ng/L)	Exposure (ng/kg body weight/day)		HBGV (ng/kg body weight/day)
		Newborns (3 kg)	Infants (10 kg)	
PFOS	45	**12**	3.6	6.25
PFHxS[a]	11	2.9	0.9	20.8

A.4 PFAS IN FOOD CONTACT MATERIALS

In 2018, RIVM conducted a survey on the level of several organic pollutants including PFOS and PFOA found in food contact materials. The observed results can be seen in Figure A.3 [22]. High levels of PFOS are found in non-stick pans and pots. High levels of PFOA are found in miscellaneous food contact paper.

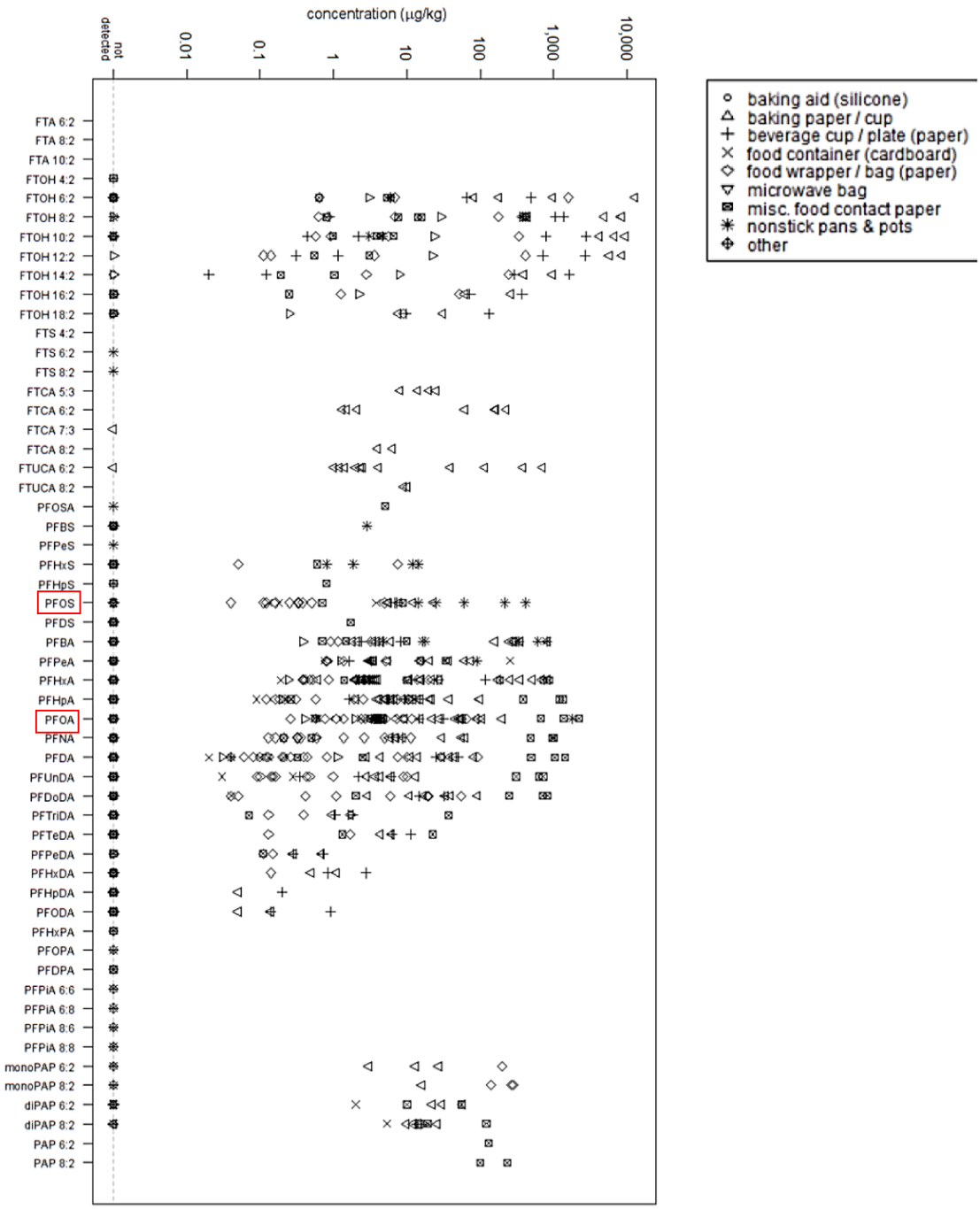

Figure A.3: PFOS and PFOA levels measured in various food contact materials [22]

A.5 SAFE EXPOSURE LIMITS OF PFAS

An overview of safe PFOA exposure limit set by various agencies like US-Environmental Protection Agency (US-EPA) and European Chemicals Agency (ECHA) are listed in Table A.3. The values are based on the toxicity studies conducted on different species like rat, mouse and monkey. European Food Safety Authority (EFSA) has listed its safe limits based on benchmark dose modelling of selected health effects found in epidemiological studies. However, due to scientific uncertainties, the conclusions derives are considered provisional [22].

Table A.3: Overview of Health-based Guidance Values (HBGVs) for PFOA [22]. (a - These values are not supported by RIVM)

Organisation (reference)	Year	Duration	HBGV		Critical effect	Species
			In serum (ng/mL)	External dose (ng/kg bw/day)		
EFSA (2008b)	2008	Chronic	-	1500	Liver	Rat, mouse
ECHA/RAC (2015)	2015	-	800	-	Repro-duction	Mouse
ATSDR (2015)	2015	Subchronic (provisional)	173	20	Liver	Monkey
US-EPA (2016a)	2016	Chronic	142	20	Develop-mental[15]	Mouse
RIVM (Zeilmaker *et al.*, 2016)	2016	Subchronic	710	100	Liver	Rat
		Chronic	89	12.5		
DWQI (2017b)	2017	Chronic	14.5	2	Liver	Mouse
EFSA (EFSA, 2018; EFSA *et al.*, 2018)	2018	Chronic (provisional)	9.4[a]	6 [a] ng/kg bw/wk	Cholesterol	Human
ATSDR (2018)	2018	Subchronic (provisional)	22	3	Develop-mental[16]	Mouse

B

XPS Analysis

XPS spectrum is a plot of the number of electrons detected at a specific binding energy. Each element produces a set of characteristic XPS peaks. These peaks correspond to the electron configuration of the electrons within the atoms, e.g., 1s, 2s, 2p, 3s, etc. The number of detected electrons in each peak is directly related to the amount of element within the XPS sampling volume. To generate atomic percentage values, each raw XPS signal is corrected by dividing the intensity by a relative sensitivity factor (RSF), and normalized over all of the elements detected.

Detection limits are often quoted as 0.1–1.0% atomic percent
Area = 100 µm, depth = 3-5 nm

Survey spectrum of a sample shows all the elements present. A survey spectrum is usually the starting point of most XPS analyses. It allows to set up subsequent high-resolution XPS spectra acquisition. The inset shows a quantification table indicating the atomic species, their atomic percentages and characteristic binding energies. High resolution spectra gives information on the chemical state and bonding of those elements.

Figure B.1 shows a morphology that is different from the morphology of Neocoat Nb/BDD anode shown in Chapter 5. This is due to the change in BDD deposition parameters. Figure B.1(B) shows the slip planes generated from crystal twinning due to dislocation behaviour (stacking faults).

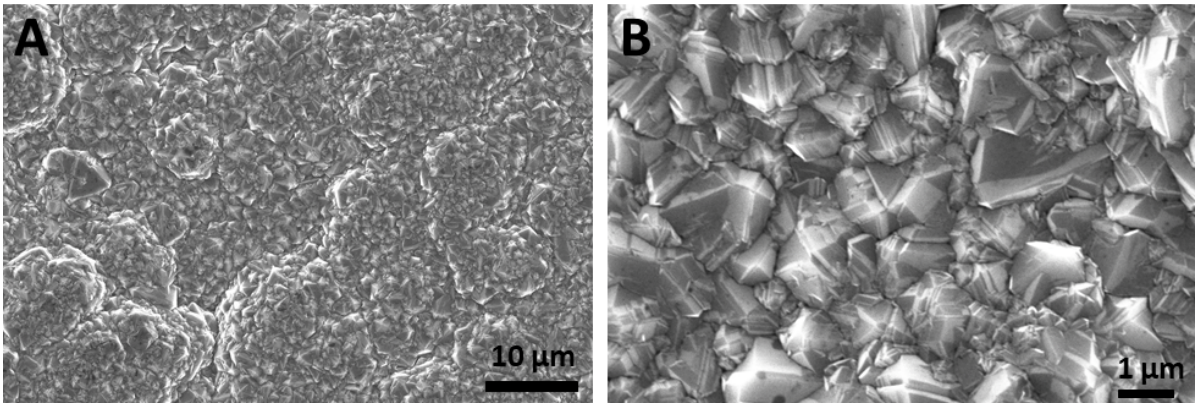

Figure B.1: SEM micrographs of the reference Neocoat Nb/BDD anode surface (A) x2000 and (B) x12000 magnification

Figure B.2 shows the survey spectrum of reference Neocoat Nb/BDD anode obtained from XPS. The spectra shows that the sample has a majority of carbon (C1s state) (93.1%)

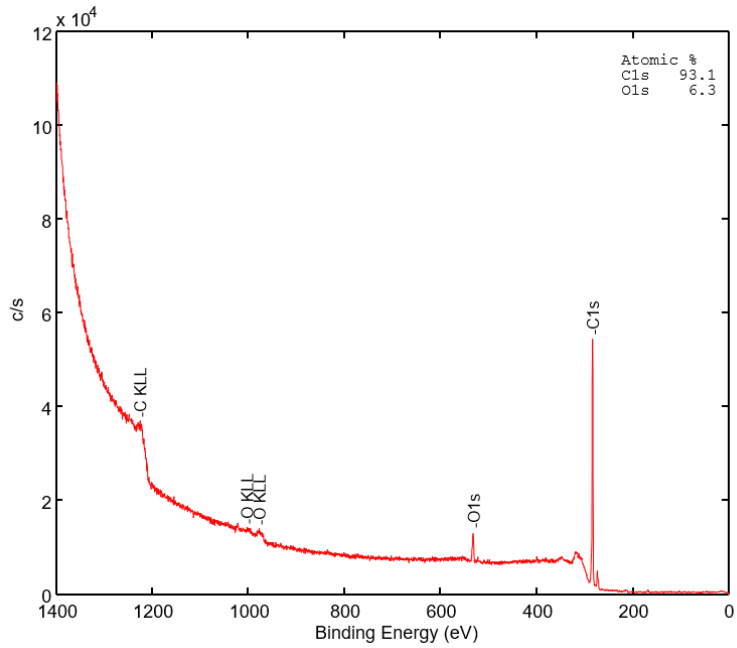

Figure B.2: Survey spectrum of the reference Neocoat Nb/BDD anode showing all the elements present

Figure B.3 shows the high-resolution XPS C1s spectra of reference Neocoat Nb/BDD anode. From the fitted spectra, the peak at 284.71 corresponds to C-C_2 (89.35%) which is attributed to the non-hydrogenated bonds (sp^3 bonds) and the peak at 286.61 corresponds to C-O (10.65%).

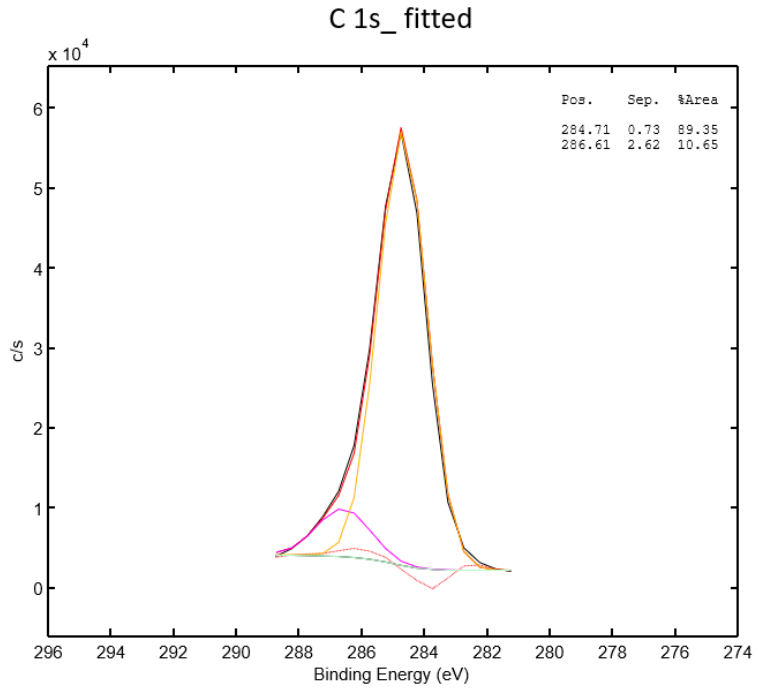

Figure B.3: XPS C1s spectra of reference Neocoat Nb/BDD anode

C

Electrochemical Degradation of PFOA using BDD Anodes

The experiments on PFOA degradation are conducted in the same cell as mentioned for Phase 1 experiments using Neocoat Nb/BDD anode. Initially, concentrations are taken as mg/L for all PFOA experiments and later, the molar concentrations are adapted for all GenX experiments to have the results published.

Electrochemical degradation conditions:

(A) 180 minutes of degradation, (B) Sample collected every 15 minutes (12 samples), (C) Current density = 5 mA/cm^2, (D) Background electrolyte = 1500 mg/L Na_2SO_4

C.1 Design of Experiments

Experiment	Na_2SO_4 (mg/L)	NaCl (mg/L)	TBA (mg/L)
1	1500		
2	1500	100	
3	1500	200	
4	1500	300	
5	1500	400	
6	1500	1500	
7	1500		10
8	1500		50
9	1500		200
10	1500		400

Figure C.1: List of experiments for PFOA degradation

C.2 Effect of Chloride on PFOA degradation

The first step in PFOA degradation is the direct electron transfer (DET) from PFOA to the BDD anode. It is observed that with increase in NaCl concentration, the PFOA degradation decreased as shown in Figure C.2. This shows that Cl^- inhibited PFOA degradation to a considerable extent by occupying active sites on

the BDD anode to form reactive chlorine species ($Cl^{\bullet}$, Cl_2, ClO^{-}) and by-products (chlorate and perchlorate) which is observed through the decrease in chloride concentration (Fig. C.3). Adding to that, with increase in NaCl concentration, the voltage decreases which directly reduces the electron transfer rate. Fig. C.4 shows the increase in chlorate concentration with time and with increase in NaCl concentration. Fig. C.5 shows the effect of chloride on the fluoride recovered. Reaction of PFOA with $OH^{\bullet}$ is responsible for the formation of thermally unstable alcohol which effectively cleaves the C-F bonds. Since oxidation of chloride (E=2.5 V) occurs at a lower potential than $OH^{\bullet}$ generation (E=2.8V), $OH^{\bullet}$ formation is hindered due to competing reactions at the anode and also due to consumption of $OH^{\bullet}$ by chloride species to form by-products. Hence the defluorination efficiency decreases with increase in chloride concentration.

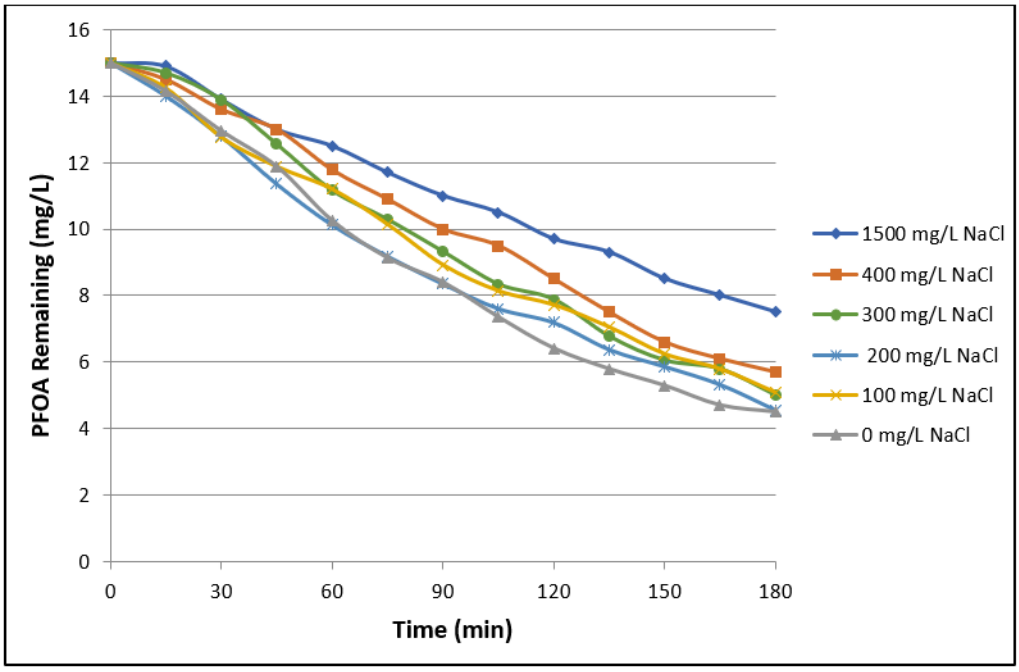

Figure C.2: Effect of chloride on PFOA degradation

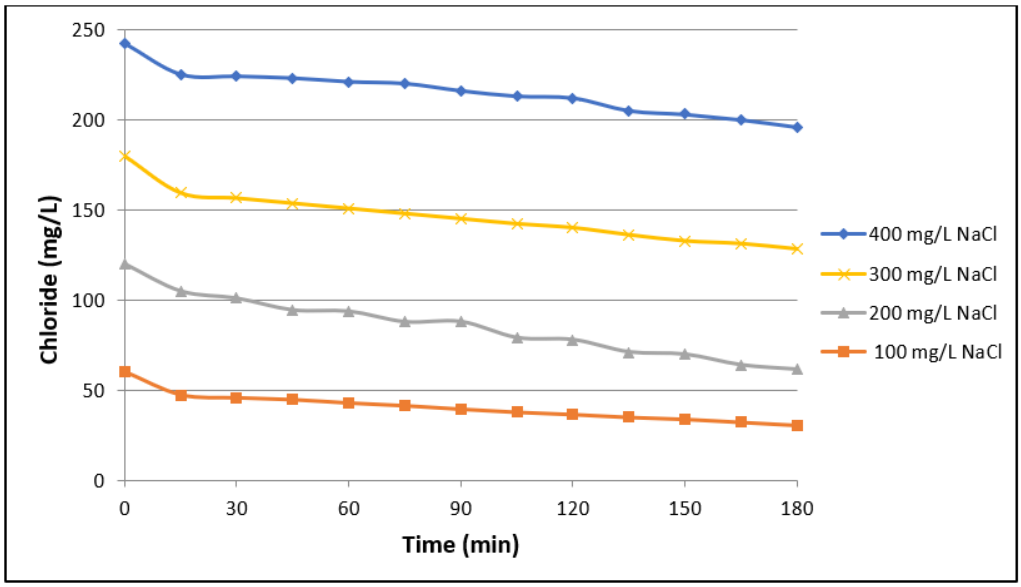

Figure C.3: Decrease in chloride concentration with time in each experiment due to the formation of reactive chlorine species and by-products

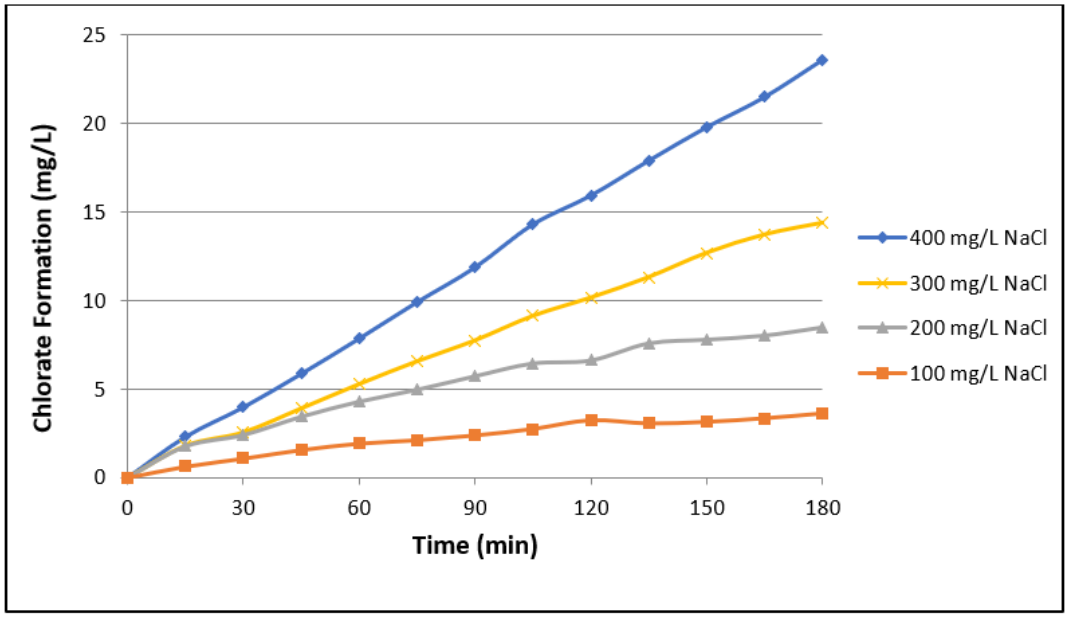

Figure C.4: Increase in chlorate concentration with time due to the oxidation of chloride ions at BDD anode

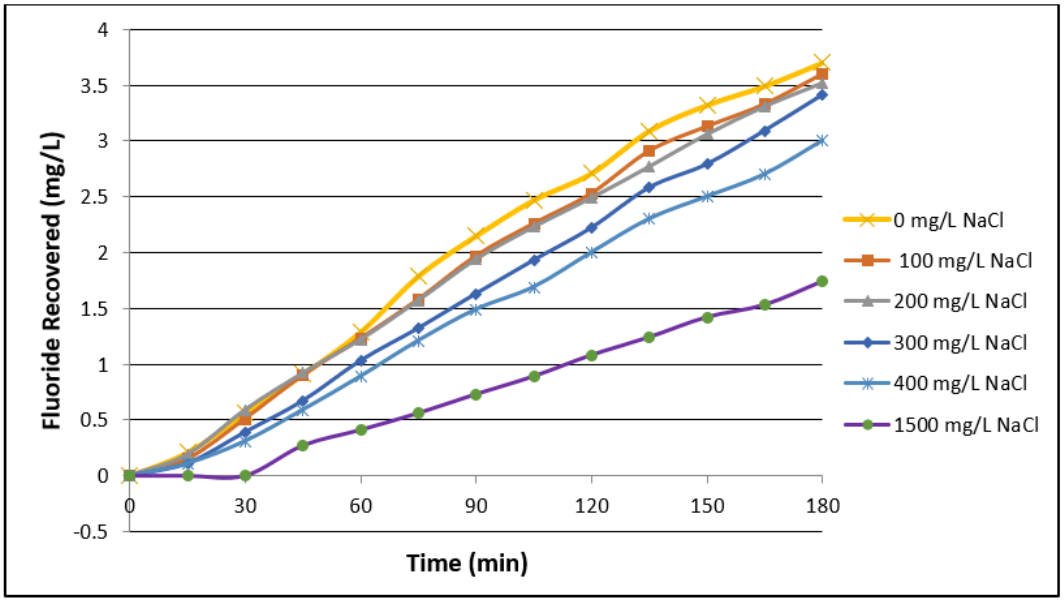

Figure C.5: Effect of chloride on fluoride (mg/L) recovery

C.3 EFFECT OF RADICAL SCAVENGER ON PFOA DEGRADATION

Tert-butyl alcohol (TBA) lacking α-hydrogen is commonly used as $OH^{\bullet}$ scavenger due to its higher reactivity with $OH^{\bullet}$. Figure C.6 shows the effect of TBA on PFOA degradation. Initially it was interpreted that $OH^{\bullet}$ take part in the first step of PFOA degradation from the observed results. But after thorough understanding of both PFOA and GenX degradation mechanism, it is understood that $OH^{\bullet}$ cannot take part in the first step of the PFOA degradation which is the direct electron transfer (DET). It has to be noted that $OH^{\bullet}$ reacts with compounds only through hydrogen abstraction and addition to unsaturated bonds and not through electron transfer mechanism. Hence, the decrease in PFOA degradation efficiency is due to the direct oxidation of TBA

competing with DET of PFOA by occupying the active sites on the BDD anode.

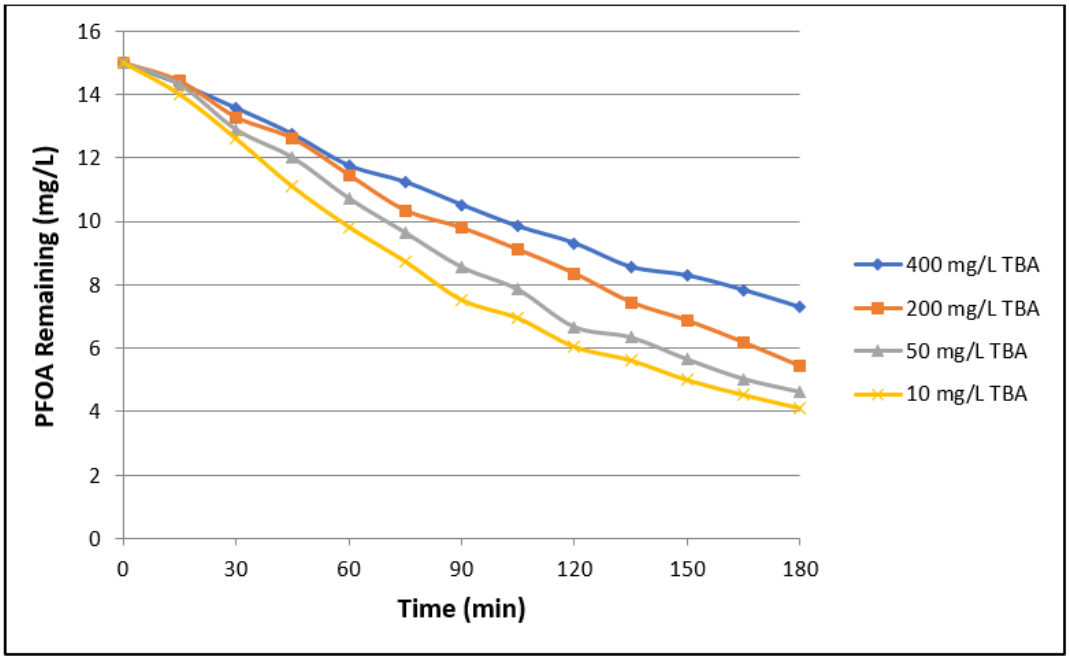

Figure C.6: Effect of radical scavengers (TBA) on PFOA degradation

D

LC-MS Analysis

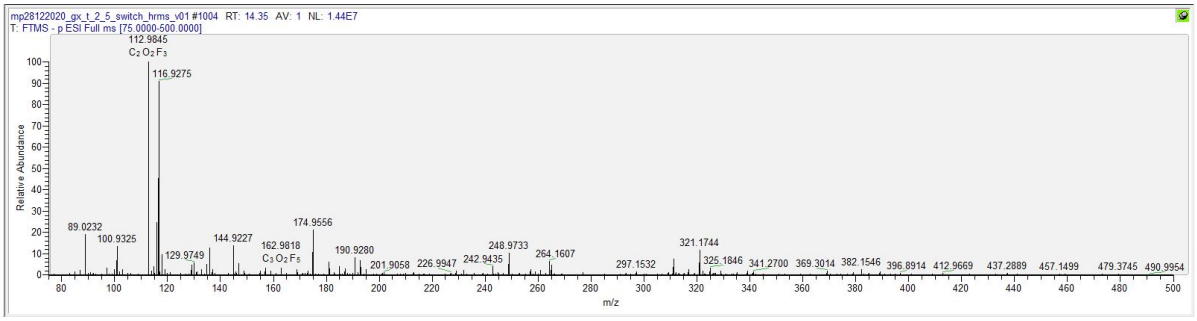

Figure D.1: Full scan spectrum acquired over a mass range 75-500 m/z. The spectrum corresponds to sample collected after 2.5 hours of degradation. Current density = 20 mA/cm^2, pH = 7, [HFPO-DA]$_0$ = 15 mg/L, electrolyte: 0.01 M Na_2SO_4, ionic conductivity = 2.34 mS/cm @ 22°C.

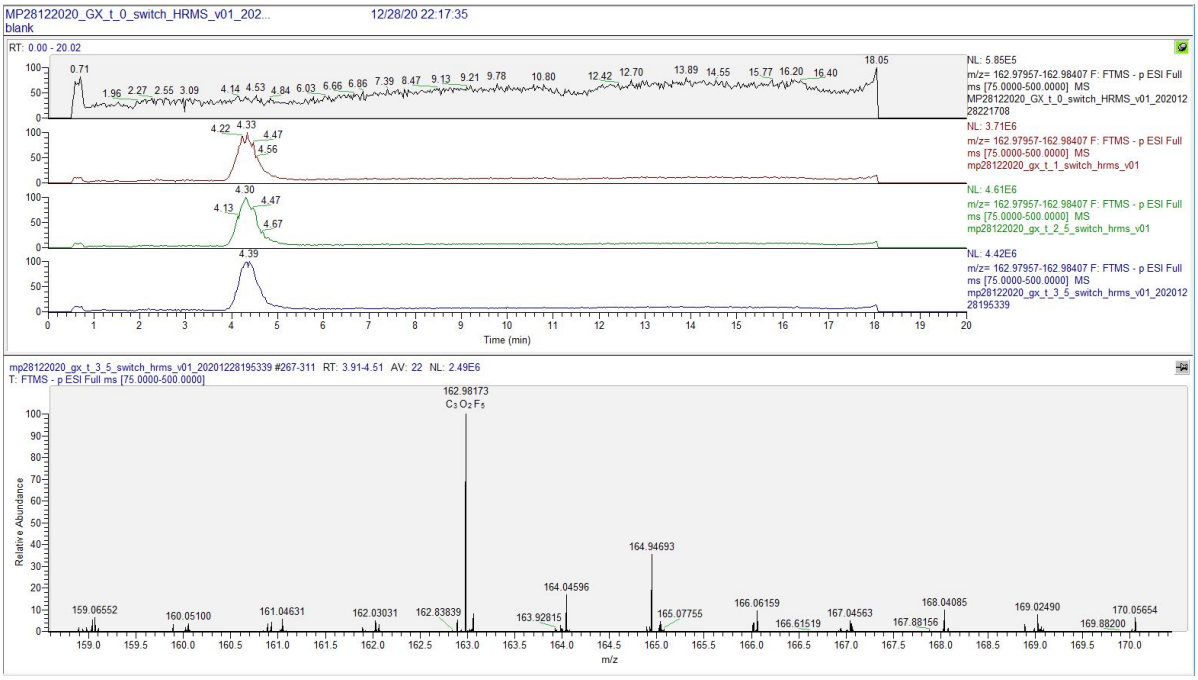

Figure D.2: MS spectrum of intermediate product PFA (pentafluoropropionic acid, $CF_3CF_2COO^-$). In the top section, the upper graph corresponds to the HPLC chromatogram of HFPO-DA sample before degradation. The other three graphs, which correspond to the HPLC chromatograms of samples taken at 1, 2.5 and 3.5 hours, show the retention of PFA at 4.3 minutes. This confirms that PFA is an intermediate formed during degradation and not due to fragmentation of the HFPO-DA molecule during LC-MS analysis.

E

EBSD

Electron backscatter diffraction (EBSD) is a microstructural-crystallographic characterization technique used to extract microstructural information such as crystal orientation, phases, grain boundary fraction and angles. The samples need to be perfectly polished in order to achieve proper backscatter diffraction. Hence, only the polished freestanding BDD is used for EBSD analysis. The measurements are conducted using a JEOL JSM 6500F FEG-SEM microscope with an EDAX/TSL detector. The band contrast image and Euler angle map of the polished freestanding BDD are shown in Figs. E.1 and E.2.

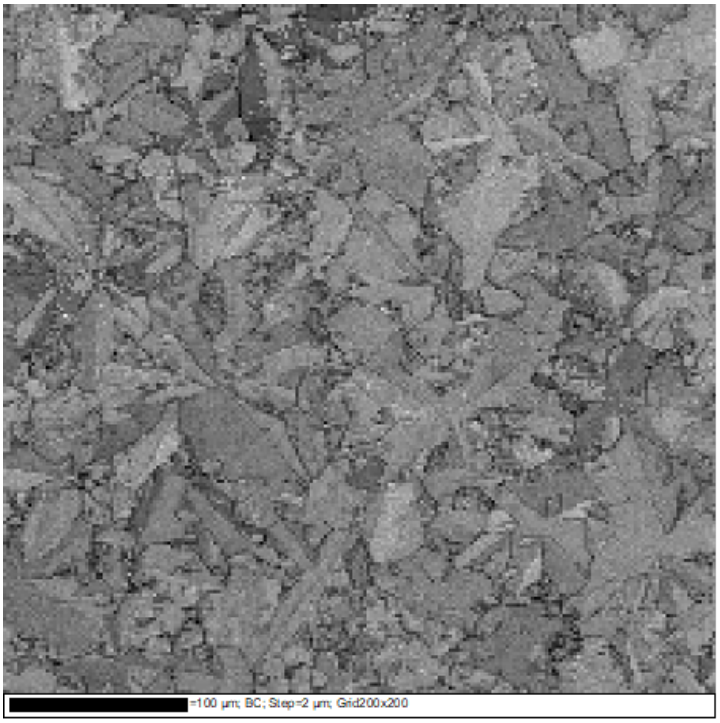

Figure E.1: Band contrast image of the freestanding BDD

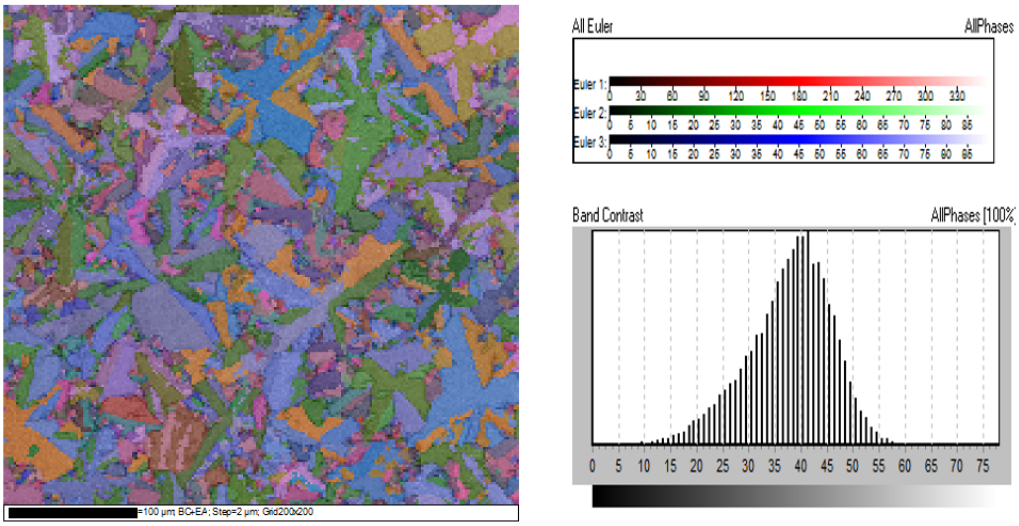

Figure E.2: Band contrast and Euler angle map of the freestanding BDD

From Figs.E.3 and E.4, it can be observed that 101 is the preferred texture. In Fig.E.3, high angle grain boundaries with an angle of 60° are predominant. This is due to the longer nucleation and growth time in order to achieve 1 mm thick BDD which results in larger grains and high angle grain boundaries. The inverse pole figure (IPF) corresponding to Z0 in Fig. E.4 corresponds to the BDD growth direction. It confirms that the <101> is the preferred orientation parallel to BDD growth.

Initially, BDD growth starts in <111> direction and with an increase in thickness the grains orient to <101>. The only explanation given to this observation in literature is based on a computer simulation [103] which reported <101> direction as the fastest growth direction. 101 as the most preferred texture is also reported in two other literature reports [104, 105]. This confirms the fact the BDD grains orient to <101> since it is the fastest growing direction.

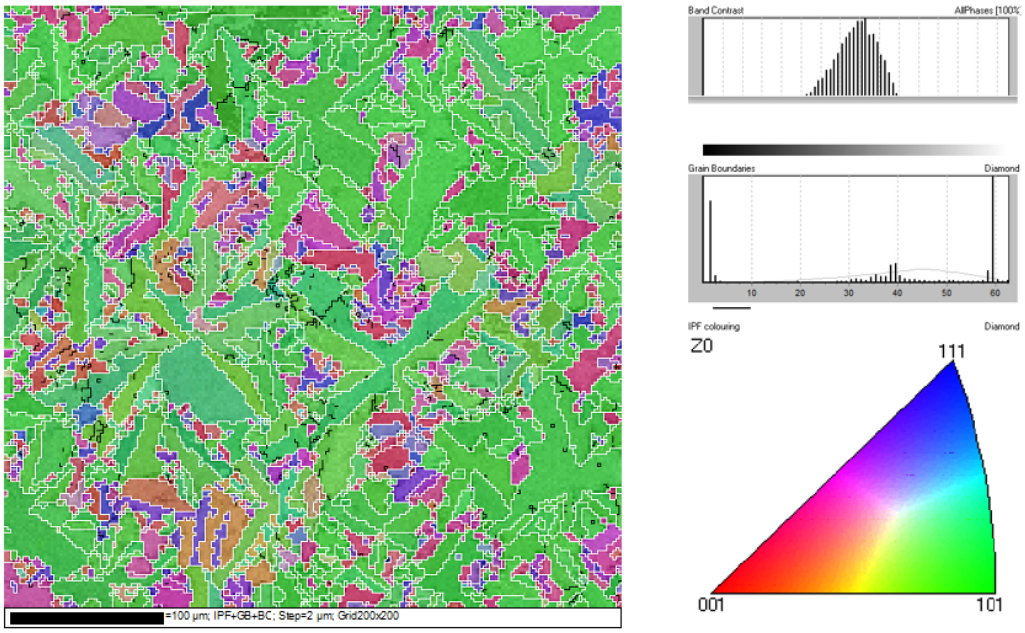

Figure E.3: EBSD inverse pole figure map showing the grain orientation and grain boundary angles

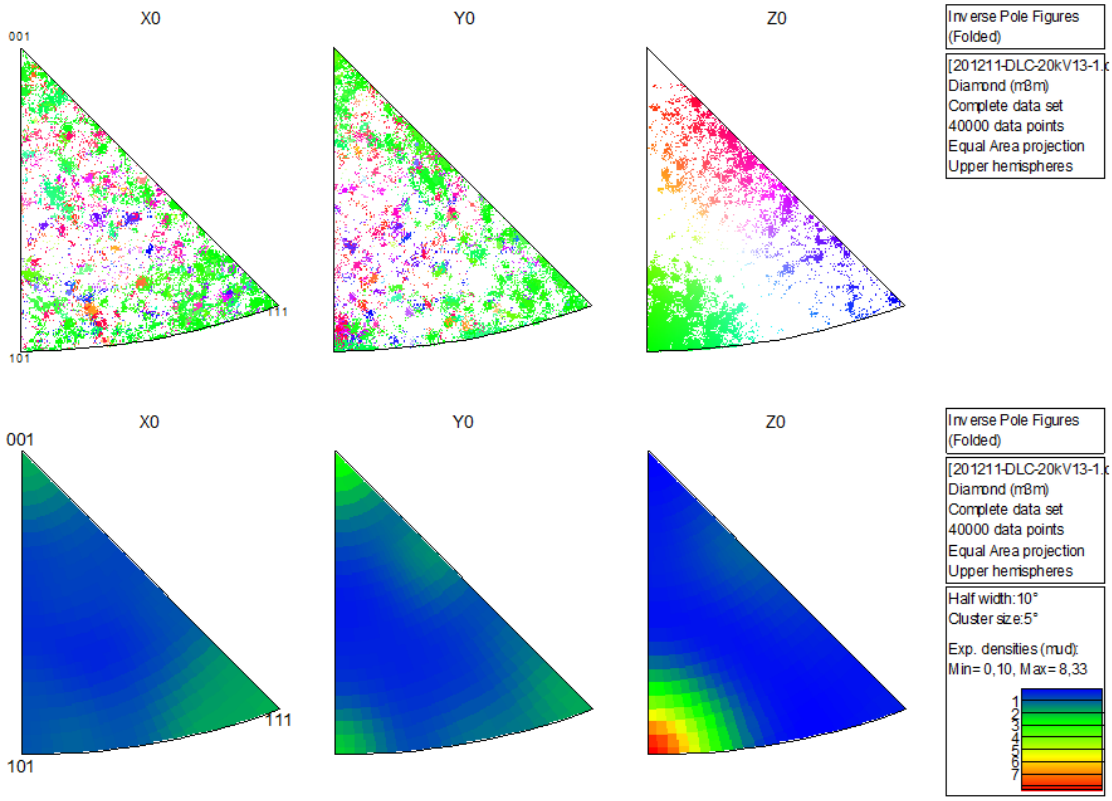

Figure E.4: EBSD inverse pole figures obtained from different crystal axes. Z0 corresponds to the BDD growth direction.